UNIVERSITY OF CALIFORNIA, SAN DIEGO

Retro-Modulators and Fast Beam Steering for Free-Space Optical Communications

A Dissertation submitted in partial satisfaction of the
Requirements for a degree Doctor of Philosophy

in

Electrical and Computer Engineering

by

Trevor Keith Chan

Committee in charge:

Professor Joseph Ford, Chair
Professor Prabhakar Bandaru
Professor Steven Buckley
Professor Yeshaiyahu Fainman
Professor Shayan Mookherjea

2009

The Dissertation of Trevor Keith Chan is approved, and it is acceptable in quality and form for publication on microfilm and electronically

_____

_____

_____

_____

_____
Chair

University of California, San Diego

2009

DEDICATION

This dissertation is dedicated to the many people that helped me along my way throughout my degree. First and foremost, I would like to thank my advisor, Professor Joseph Ford, for his advice and dedication to me starting from when there was nobody else in the Photonic Systems Integration Lab (PSI-Lab) group. I also want to recognize the current members of the PSI-Lab for giving me their input and support in my research. I also would have never made it to this point without the opportunity I was given by Dr. Ying Tsui of the University of Alberta. Dr. Tsui gave me my first steps in the photonics field and I haven't stopped ever since. Finally, I want to think my family for supporting me even though my decisions weren't always their favorite. I want to especially thank my brother who paved the way ahead of me and was able to warn me of the pitfalls in advance.

TABLE OF CONTENTS

LIST OF FIGURES AND TABLES

ACKNOWLEDGMENTS

The text of Chapter Two, in part or in full, is a reprint of the material as it appears in the following publications:

- T. K. Chan, J. E. Ford, “Retroreflecting optical modulator using an MEMS deformable micromirror array”, J. Lightwave Tech., 24 (1), January 2006.

The dissertation author was the primary researcher and author. The co-authors listed in these publications directed and supervised the research which forms the basis for these chapter.

The text of Chapter Four, in part or in full, is a reprint of the material as it appears in the following publications:

- T. K. Chan, J. Karp, R. Jiang, N. Alic, S. Radic, C. F. Marki, J. E. Ford, “1092 channel two-dimensional array demultiplexer for ultra-large data bandwidth”, J. Lightwave Tech., 24 (1), March 2007.
- T. K. Chan, E. Myslivets, J. E. Ford, “2-Dimensional beamsteering using dispersive deflectors and wavelength tuning”, Opt. Express, 16 (19), September 2008.

The dissertation author was the primary researcher and author. The co-authors listed in these publications directed and supervised the research which forms the basis for these chapter.

VITA

2002 Bachelor of Science in Engineering Physics, University of Alberta

2004 Master of Science in Electrical Engineering (Photonics), University of California, San Diego

2009 Doctor of Philosophy in Electrical Engineering (Photonics), University of California, San Diego

PUBLICATIONS

1. T. K. Chan, J. E. Ford, “Retroreflecting optical modulator using an MEMS Deformable Micromirror Array”, J. Lightwave Tech., 24 (1), January 2006.

2. T. K. Chan, J. Karp, R. Jiang, N. Alic, S. Radic, C. F. Marki, J. E. Ford, “1092 channel two-dimensional array demultiplexer for ultra-large data bandwidth”, J. Lightwave Tech., 24 (1), March 2007.

3. T. K. Chan, E. Myslivets, J. E. Ford, “2-Dimensional beamsteering using dispersive deflectors and wavelength tuning”, Opt. Express, 16 (19), September 2008.

ABSTRACT OF THE DISSERTATION

Retro Modulators and Fast Beam Steering for Free-Space Optical Communications

by

Trevor Keith Chan

Doctor of Philosophy

University of California, San Diego, 2009

Professor Joseph Ford, Chair

Free-space optical (FSO) communications is a means of secure, high bandwidth communication through the use of a modulated laser beam in free-space as the information medium. The chaotic nature of the atmosphere and the motion of the communication nodes make laser alignment a crucial concern. The employment of

retro-reflecting modulators makes the bidirectional quality of a communication link into a one sided alignment problem. While there are existing retro-reflecting modulators, their trade-offs create a lack of abilities (such as aperture size, angular range, high modulation speeds, economic viability) which do not fulfill the requirements for certain applications. Also, the beam must be directed towards the intended receiver. Form mobile or scintillated communication links, beam direction must be adaptable in real time. Once again, this area suffers from trade-offs where beamsteering speed is often limited. Research used to mitigate the trade-offs and adapt the devices into viable options for a wider range of applications is explored in this dissertation.

Two forms of retro-modulators were explored; a MEMS deformable mirror retro-modulator and a solid silicon retro-modulator that modulated the light by frustrated total internal reflection (FTIR). The MEMS version offered a high speed, scalable, wavelength/angle insensitive retro-modulator which can be massed produced at low cost, while the solid retro-modulator offered a large field of view with low cost as well. Both modulator's design, simulated performances, fabrication and experimental characterization are described in this dissertation.

An ultra-fast beamscanner was also designed using 2-dimensional dispersion. By using wavelength switching for directional control, a beamscanner was developed that could switch light faster than pre-existing beamscanners while the beams characteristics (most importantly its aperture) could be freely adjusted by the independent optics. This beamscanner was preceded by our work on a large channel

wavelength demultiplexer which combined two orthogonally oriented wavelength demultiplexers. This created a 2-dimensional array of spots in free-space. The light was directed be a collimating lens into a specific direction based on its wavelength. The performance of this beamscanner was simulated by modeling the dispersive properties of the components.

Chapter 1

Introduction

1.1 Free-space optical communications

Wireless radio links and fiber optics are two prominent communication solutions in modern technology. Wireless radio links offer freedom from static by transmission cords; the only requirements are the transceiver and the receiver. They are easy to install and have a flexible communication path; however, radio signals are broadcast over a large area allowing them to be read by unwanted receivers. On the other hand, fiber optic communication offer high bandwidth inherent of optical signals. While these two communication methods have their advantages, there are still niches such as the "last mile" [1][2] and secure battlefield communication where neither method will suffice.

Free-space optical (FSO) communications combines the advantages of radio wireless and fiber optic systems by projected a beam of light as the information carrier. This method incorporates the speed and security of an optical signal with the flexibility and freedom of a wireless signal.

In the atmosphere, the establishment of the communication link comes with several costs due to the chaotic nature of the atmosphere which the optical signal must traverse. Water particles become a deterrent for laser transmission due to its highly absorptive nature. Other atmospheric gases, particles and temperature gradients also result in refraction or diffraction of a light beam, thereby interfering with the

transmitted signal. Thus, for terrestrial communications, FSO communications has only been successfully applied to short range (~ km) communication links. This has been previously demonstrated between stationary nodes [3][4]. On the other hand, we can use active pointing and tracking to combat the effects of scintillation and maintain signal fidelity. Active alignment also allows for communication links to be maintained between mobile nodes. Current technology is limited in the speed and distance at which it can maintain such a dynamic link.

1.2 Components of a FSO link

The establishment of a typical FSO link requires several components. This starts with the source of light which is typically a laser beam. Infrared light, especially in the C-band (1530 to 1565 nm), is usually selected for optical communication because the human eye is relatively insensitive to its effects. Although commonly used, monochromatic light is not necessary for optical communications. For certain applications, a broad spectrum of light is sufficient or advantageous.

Modulation is typically in the form of binary, on/off modulation of a laser beam. This has been demonstrated where high speed lasers are modulated on and off at sufficient modulation speeds for video transmission [5]. If the light source is not directly modulated, an optical modulator would follow the light source to encode the signal. Optical modulators include, but are not limited to, electrooptic (EO) Mach Zender interferometers, acoustooptic (AO) modulators, MEMS and liquid crystals.

The modulated beam is then transmitted through beam forming optics. When long distance transmission is the goal, the ideal beam is a large aperture collimated beam which results in a small divergence and maximizes power delivery. This typically requires the expansion and wavefront flattening of the optical signal during or after modulation.

Additionally, a FSO communication node would also consist of a receiver component. This can consist of a collection lens which concentrates the light onto an optical detector. Once the signal has been digitally converted, it can then be processed for information.

1.2.1 Beamsteering

The above requirements are enough to create and detect a modulated light signal. For FSO communications, this signal needs to be directed towards the intended receiver. In most FSO communication systems, the pointing direction of the optical signal will not be stationary and active alignment to the target is necessary. In some cases, the entire laser assembly can be manually or mechanically tilted to the proper direction [6]. In most systems, however, this method is not fast enough to keep up with the dynamics of agile FSO links. This includes communication between mobile communicators (including unmanned aerial vehicles (UAVs) [7] which is ideally suited for FSO) and communication through distorting atmospheric conditions [8],[9][10],[11],[12],[13].

Several methods have been used to steer a beam over a range of angles. An obvious solution involves simply reflecting the light off a tiltable mirror, such as a

galvanometric scanner. Although these large mirrors suffer in speed and power dissipation, tiltable mirrors can be small when they are made as microelectromechanical systems (MEMS) [14],[15][16]. These mirrors operate considerably faster with multi-kHz sweeping speeds, but are limited to millimeter sized apertures. This trade-off between size and speed is a concern because a smaller aperture leads to a greater beam divergence which in turn decreases the range. Acousto-optic [17] deflectors are limited in their total angular range and electro-optic [18] crystals require kilovolt drive voltages to obtain an adequate angular range and aperture. Table 1.1 provides a summary of the versions of beamscanning systems and their typical characteristics.

Table 1.1: Summary of beamscanning solutions

	Speed	Range	Aperture	Key limitation
Galvanometric	KHz	~ 30°	~10mm	Bulk, power, reliability
MEMS mirror	KHz	~ 5°	~1mm	Aperture, power handling
Acousto-optic	KHz	~ 1°	~10mm	Angle range
Liquid Crystals	100 Hz	~ 60°	>100mm	Speed, environmental constraints
Electro-optic	MHz	~ 1°	~10mm	Drive current, angle range

The ideal beamsteering device for FSO links would have a combination of fast switching speeds, large aperture, pointing accuracy and low power. Usually, the desired performance parameters are intertwined such that when high speed (> kHz) is achievable, it is reached at the expense of one of the other parameters.

An indirect way to increase aperture size without decreasing performance is by segmenting the aperture into an array of sub-apertures. Each sub-aperture functions as its own device and therefore, maintains the advantages of a small aperture device. However, the cost of segregation is that each aperture has to be phase matched to one another.

Alternatively, phase matching itself can be used as a means of beamsteering. This has been done with arrays of liquid crystals [19] where the phase delay from each element in an array is given a phase delay such that emitting wavefronts match in the desired beam propagation direction. However, liquid crystals can only be tuned at kilohertz speeds.

For bidirectional communications, all of the requirements listed above would be required at both ends of the communication link; however, this is not necessary if we make use of a retro-reflecting modulator (also referred to as a retro-modulator). Put simply, the retro-modulator recycles optical power by reflecting it in the opposite direction while encoding a returned signal, thereby drastically simplifying the remote optical communications terminal. This arrangement is illustrated in Figure 1.1. It is ideally suited for asynchronous communications where a lower frequency return signal can be carved over the original high frequency modulated signal. This includes applications such as remote telemetry or tagging for identification [20],[21],[22]. Retro-communication is ideally suited for these purposes where stealth, security, light weight, low cost and low power consumption become invaluable. In fact, the power

consumption of retro-modulators can be so small such that it can be powered by the incoming light signal [23][24].

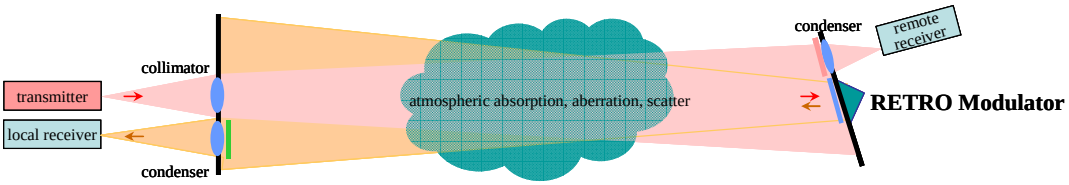

Figure 1.1: Retro-communications system using automatic retro-reflected alignment.

As its name suggests, the retro-reflecting modulator is a combination of a retro-reflector and a modulator. They can carve a signal into the retro-reflected beam by either absorbing the incident signal, or by scattering the reflected wavefront so that it does not propagate back to the source. There are two types of retro-reflector that are prevalently used: the Cat's Eye retro-reflector and the Corner Cube retro-reflector. Both of these are passive devices which makes them easier to incorporate into a system.

1.2.2 Cat's eye retro-reflector

The Cat's Eye retro-reflector, illustrated in Figure 1.2, consists simply of a lens followed by a reflective surface at its focal plane. Collimated light shone into the retro-reflector passes through the lens to create a point source at the reflective surface. The light is then reflected back through the lens and recollimated. Since the light has not been translated at the focal plane, the light is retro-reflected in the same but opposite direction from which it came.

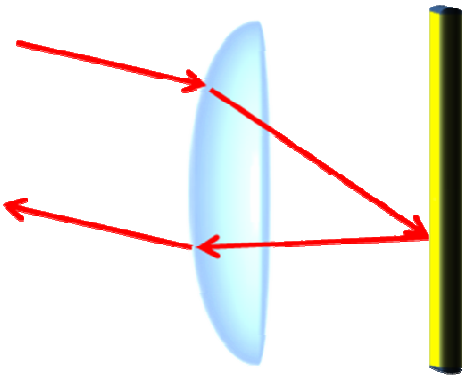

Figure 1.2: Cat's Eye retro-reflector

1.2.3 The Corner Cube retro-reflector

The Corner Cube retro-reflector, illustrated in Figure 1.3, consist of three planar reflectors connected at right angles to each other like the corner of a cube (hence the name). Each mirror changes one Cartesian direction of the light to its exact opposite. When the light is reflected off all three surfaces, it exits the corner cube in its conjugate direction. Like the Cat's Eye retro-reflector, a retro-reflected image will be inverted.

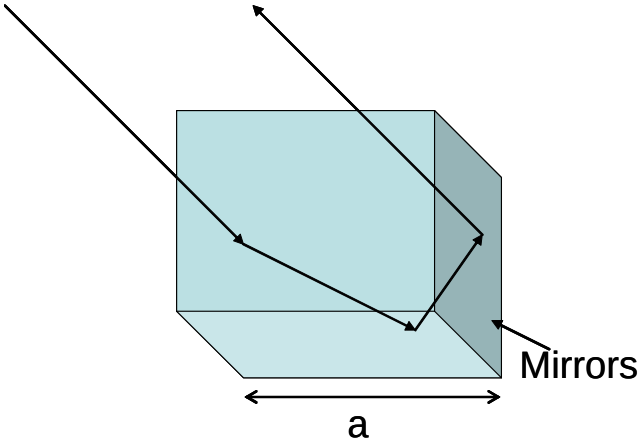

Figure 1.3: Corner-cube retro-reflector

An important consideration for retro-modulators is the amount of power that is returned to the interrogator. Since retro-modulators are used in far-field operation, the diameter of the retro-reflector can be mathematically simulated as a diffracting hole. As such, the amount of power returned is proportional to aperture of the retro-reflector. Equation 1.1 describes the metric representing the reflected power density, where a is the diameter of the retro-reflector, λ is the wavelength of the optical beam and z is the distance separating the interrogator and the retro-reflector.

$$\eta = \frac{a}{2.44\lambda z} \tag{1.1}$$

This shows that more light is returned as we increase the size of the retro-reflector.

Since long distances are involved, the alignment of the three sides of the corner-cube is crucial. If one mirror of the retro-reflector is tilted more than half the angle of the returning diffraction limited beam, then the retro-reflected beam will not be received by the interrogator. This is described by Eq. (1.2).

$$\Delta\theta < \frac{1.22\lambda}{a} \tag{1.2}$$

For example, for 1550 nm light and a 1 cm diameter retro-reflector, the mirrors need to be aligned to approximately one hundredth of a degree.

1.2.4 Retro-reflecting Modulators

These two retro-reflectors operate with different geometries; therefore, each are suited for different types of modulators depending on their mode of operation. For

example, modulation can be achieved by placing a large area, transmissive modulator in front of the retro-reflector. This mode has been demonstrated with EO [25] and AO [26] modulators, although studies of these forms of retro-modulators are not highly pursued due to their limited field of views.

A more promising area in this field has come with the discovery of the quantum confined Stark effect [27]. This phenomenon involves the spectral shifting of an absorption peak in multiple quantum wells when an electric field is applied to the stack. This is appropriately called an electro-absorption modulator (EAM). These modulators have the potential for modulation speeds up to 10 Gbit/s and have been used in reflective [28] and transmissive [29][30] modes. The current challenge governing these modulators is their manufacturing yields at large sizes [31][32][33] with a large angular field of view and wavelength insensitivity. Current EAM retro-modulator systems have demonstrated fields of view of ±10° for 5 mm apertures [34].

The other major area in retro-modulation employs MEMS modulators. These have come in various forms. One method simply employs phase modulation by moving the retro-reflector along the beam direction with MEMS actuators [35]. This is done using a spherical cat's eye retro-reflector while the mass of this retro-reflector is inversely proportional to the resonant frequency which it can be moved. Another variation consists of a corner-cube retro-reflector where MEMS actuate the orientation of one of the three mirrors [36][37][38]. This disrupts the tight alignment tolerances necessary for retro-reflection such that a signal is no longer returned when the mirror is tilted. Again, the mass which moves limits the speed of modulation. This

modulator achieved 1000 Hz resonance for a 500 μm moving mirror. The mass, and also the switching times, can be reduced by segmenting the moving parts. This was accomplished where one of the mirrors in a corner-cube retro-reflector was replaced with an MEMS actuated grating [39]. This grating consisted of deformable ribs which would convert it from a diffraction grating into a flat mirror. This had an increased switching speed of 13.4 kHz, but its diffractive nature limited its angular range to approximately ±5°.

1.3 Scope of the Dissertation

While there has been much development in FSO communications, we have seen that the existing devices are unable to meet all of the requirements which would make them cheap and versatile for a wide range of applications. For instance, a common theme that is seen is the tradeoff between large aperture and device speeds. In the area of UAV communications with involving a fast moving surveillance vehicle, the requirements would include a large angular field of view retro-modulator which can transmit video signals over a respectable (several kilometers) range. None of the aforementioned retro-modulators simultaneously satisfy all of these requirements. My work incorporates unconventional designs and optical phenomena into new retro-modulators and beamscanners to mediate the trade-offs and better suit the needs of specific FSO niches.

While my devices are not unrelated, the dissertation is organized such that each chapter details the work done on a different device. This is done as follows.

Chapter 2 discusses the work done on a MEMS deformable mirror retro-reflecting modulator. This includes mathematical simulation work to find the optimum deformable mirror arrangement as well as predictions on its performance. I has the deformable mirror fabricated based on the simulation results and demonstrate its performance both as a deformable mirror and when it is integrated into a corner-cube assembly.

Chapter 3 discusses the work done on a solid silicon corner-cube retro-reflector which modulates using the phenomenon of frustrated total internal reflection (FTIR). This begins with modeling of FTIR between silicon pieces and a discussion on possible ways to extinguish the light once it is outside of the corner-cube. I then created a nano-positioning system to have nanometer control over the FTIR gap size. This revealed that it was necessary to have pressure between the corner-cube and the parasitic absorber to achieve FTIR. I describe a new set of experiments which explore this realization and create a prototype accordingly. I then present the results from the characterization of this prototype.

Chapter 4 discusses the work done on creating a 2-dimensional wavelength controlled beamscanner. This describes the work in combining two dispersive devices to achieve raster scanning over a field of angles. Results show that this system can also be applied as an ultra large channel wavelength demultiplexer.

Chapter 5 outlines the major contributions of the collected work and gives some future directions that can be extrapolated from my findings.

Chapter 2

MEMS Deformable Mirror Retro-Reflector

2.1 Introduction

Several retro-modulator characteristics directly impact overall communications system performance: wavefront aberration and effective optical aperture affect maximum operational range; modulation response time and contrast ratio determine data bandwidth; and operational tolerances including modulator acceptance angle, wavelength range, and ability to withstand physical and thermal shock determine overall system utility and robustness. In remote telemetry the communications range may extend from 0.1 to 10 km, and must operate under varying environmental conditions. This means that the effective optical aperture must be 1 cm or larger, and the wavefront distortion should be below $\lambda/10$. Further, we require that the system operate under a wide range of incident angles: up to +/- 30° is possible with a hollow corner-cube retro-reflector. To allow spread-spectrum and wavelength-agile systems, and to avoid excessive system costs, we want the modulator to function over the 1.45 to 1.55 µm spectrum in the eye-safe communications range. Finally, we prefer a data modulation contrast of 10:1 (2:1 required) and a data modulation rate of at least 100 kHz. Data rates as high as GHz are desirable, but a wide range of remote telemetry application requirements can be satisfied with 100 KHz modulation.

Previous MEMS retro-modulators demonstrated using a full-aperture tilting mirror [38] successfully yielded large contrast ratios. Their functional angular range is limited only by the acceptance angle of the corner cube. However, the electromechanical switching of the tilting mirror requires switching time which is a function of the mirror size. This approach limits the response time of larger aperture (long-range) retro-modulators to milliseconds. Another successful MEMS retro-modulator used a diffractive structure [39], a reflective diffractive grating which is electromechanically switched into a flat, refractive surface. This grating light modulator provides faster modulation (~1 MHz) since very little mechanical deflection (~$\lambda/4$, or 0.3 μm) is required. However, this modulator requires wavelength and angle matching, which limited the operating angle range to 6 degrees even for low (0.4 dB) contrast. So far, researchers have not achieved the desired combination of speed, aperture, and wavelength and angle insensitivity.

Reflective MEMS etalons using a drumhead structure with a variable air gap have been extensively investigated for use in telecommunications as data modulators [40] and broad spectrum variable attenuators [41]. The response time of such devices depends on several parameters, including the drum diameter and membrane tension, but have been demonstrated to operate at well over 1 MHz [42]. This is still orders of magnitude slower than multiple quantum well modulators [43], but the MEMS devices are also far less expensive to manufacture (especially for large apertures) and less sensitive to operating wavelength and temperature. In fact, a large-aperture MEMS

etalon modulator based on this design and intended for use with cat's-eye retro-reflector optics was recently successfully tested [44].

In this chapter, we present theoretical and experimental results on a MEMS device based on the same device structure but modified to act as a first-surface deformable mirrors rather than an etalon. When this device is assembled into a corner cube, the result is a highly efficient wavelength and angle insensitive retro-modulator.

2.2 Deformable micro-mirror array concept and design

The basic device, shown in Figure 2.1, is a first-surface MEMS deformable mirror switching from flat to a hexagonal array of concave microlenses. This device concept was first proposed in 1996 [45], and a somewhat different rectangular structure was tested in Delft University of Technology [46]. When the device is structured as an array of spherical microlenses, the modulator operates midway between the geometrical and diffractive regimes; light distribution is substantially determined by geometrical curvatures, but interference between multiple diverging beams produces strong diffraction effects that suppress the zero-order reflectivity. The microlenses are separated with 1 mm pitch and have a 75% deformable surface area. The active area, when arrayed in smaller deformable sections, achieves greater lenslet curvatures and shorter switching times. This allows for scaling of the device to large (10 cm +) apertures without sacrificing speed or diffraction efficiency.

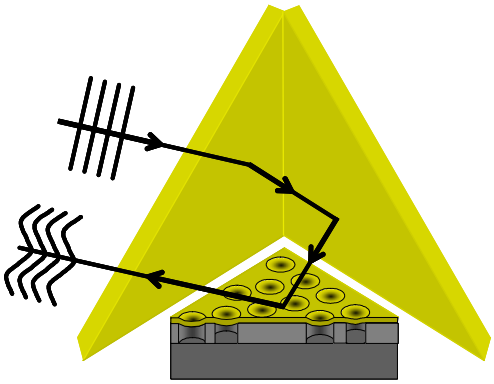

Figure 2.1: Diagram of the MEMS deformable mirror, showing a section of the device to reveal air pockets that allow deformation at selected areas.

We calculated the diffractive behavior of the lenslet arrayed micromirror using Huygens-Fresnel diffraction theory on a single deformable mirror structure. The other two mirrors of the corner-cube were not included in these calculations so that we could understand the direct effect of the deformable mirror on a reflected wavefront. The device surface profile was modeled and sampled by a 250x250 grid of pixels. In accordance with Huygens-Fresnel diffraction theory, each pixel on the device surface projected a spherical wave given by Eqs. (2.1) a and b.

$$u(x', y', z') = \sum_{m=1}^{M} \sum_{n=1}^{N} \frac{1}{j\lambda r_{mn}} e^{jkr_{mn}} \tag{2.1a}$$

$$r_{mn} = \sqrt{(x'-x_m)^2 + (y'-y_n)^2 + (z'-z_{mn})^2} \tag{2.1b}$$

The resulting phased signals are propagated 6.6 m to the readout plane, effectively in the far field. Figure 2.2 a and b shows the resulting far field diffraction patterns from the flat and deformed mirror when it is illuminated by a plane 1550 nm wavelength wavefront at normal incidence. The zeroth-order diffracted beam is

shown at the center of the figures. Both figures use a logarithmic scale to best display the diffracted far-field pattern which, by Fraunhoffer diffraction theory, is the Fourier transform of the deformed mirror surface. We see a hexagonal array of spots in an envelope created by the refractive aperture of the individual microlenses. Each spot in the array replicates the original reflected beam shaped by the mirror array aperture. The spots are separated by a pitch inversely proportional to the array spacing of the deformable mirror lenslets.

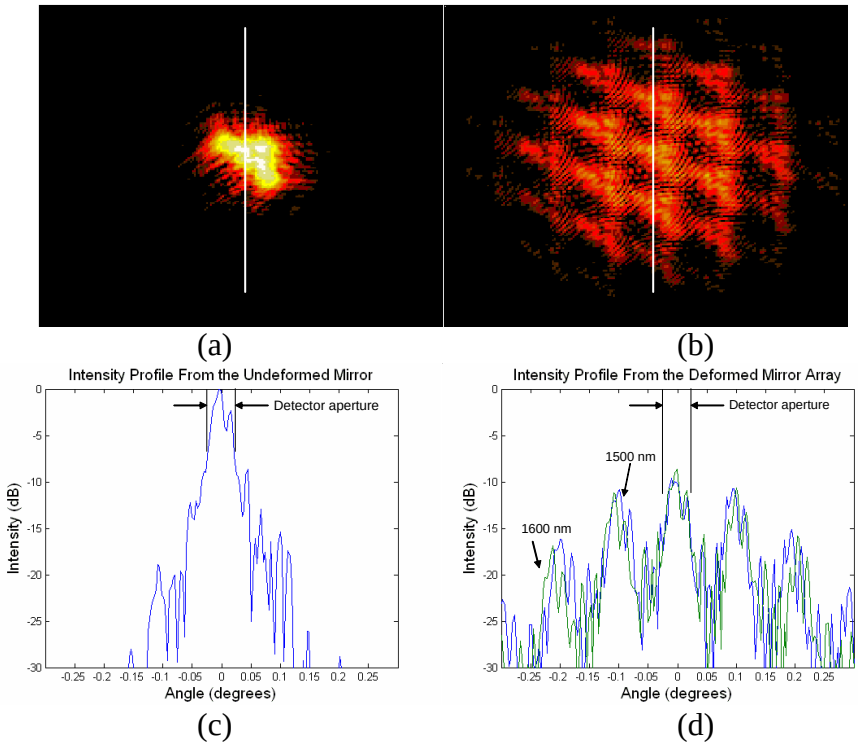

Figure 2.2: Calculated far-field patterns (normalized) with (a) 0 deflection and (b) 0.55 um deflection and their line profiles (c) and (d). The line profile from the deformed mirror (d) is calculated using 1500 nm and 1600 nm light to demonstrate the wavelength insensitivity of diffraction. Photos and plots both use a logarithmic intensity scale.

Fresnel diffraction theory predicts the near linear relationship, Eq. (2.2), between the period of the arrayed diffraction pattern and the spatial frequency (1/T) of the microlens array. Figure 2.2 c and d show the line profile of the far-field diffraction pattern where Figure 2.2 d is calculated with 1500 nm and 1600 nm light. These two line profiles are difficult to distinguish; showing that the simulations predict low wavelength sensitivity. Unlike a single-wave delay diffractive MEMS modulator, the diffraction pattern scales with wavelength by 4.0 μrad/nm, while maintaining approximately the same contrast.

$$\tan\theta_{period} = \frac{\lambda}{T\cos\left(\frac{\pi}{6}\right)} \tag{2.2}$$

For FSO communications, the signal energy collected by the original source transmitter is proportional to the power in the zeroth order diffracted beam. In all of our simulations, the detector aperture is taken around this beam. Figure 2.3 shows the computed relative power incident on the detector as we increase the device deformation. This is shown for different mirror tilt angles, α, which are also the angles of incident light. An increase in the deformation immediately results in a decrease of power at the detector for all incident angles. With further deformation, the detected power oscillates, typical of diffraction phenomena, and dampens to a lower intensity. The detected power does not approach zero since spaces between the deformable drums remain flat and always reflect light into the detector. We can note that 10 dB contrast ratio is maintained for incident angles up to +/- 68° at 1.5 μm

deformations. This demonstrates that the deformable mirror will work as a modulator for a large range of angles. The three mirrors in a corner cube retro-reflector are each oriented 54.7° to the normal of the corner cube, so light would typically be incident on the deformable mirror around this angle.

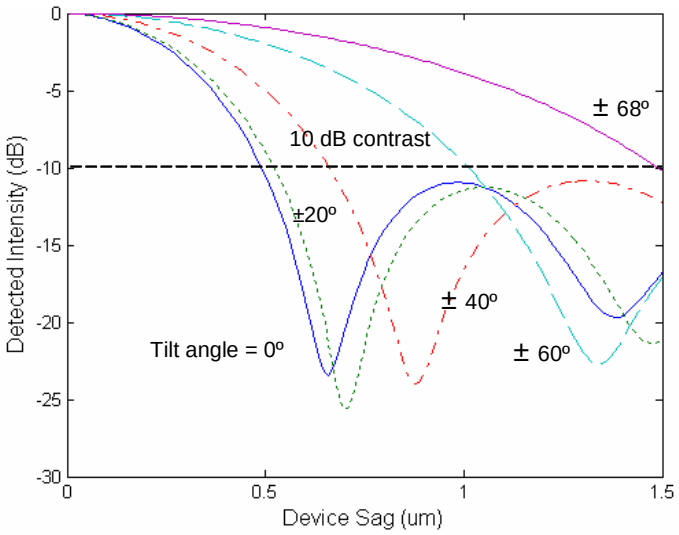

Figure 2.3: The relative intensity reaching the detector as a function of the mirror deformation. This relationship is shown at various mirror tilt angles.

A single deformable MEMS mirror can replace a mirror in the corner cube to form a retro-reflecting modulator. Furthermore, all three of the mirrors can be deformable MEMS mirrors. In this case, Figure 2.3 predicts 10 dB contrast with 0.8 μm sag for the entire angular aperture of the corner cube. Further calculations verify these contrast ratios are maintained for increasing propagation distances of at least 1 km. A mechanical deflection of less than 0.1% of the membrane width, combined with the non-contact nature of the structure, means that this device will be extremely robust to mechanical shock and sustained high-frequency operation.

2.3 Experimental demonstration of the deformable micro-mirror array

Our devices were fabricated by MEMSCAP using now-standard MEMS processes [40],[41][42]. The layered structure of the device is illustrated in Figure 2.4. A silicon substrate was covered with a 3 μm sacrificial layer of phospho-silicate glass (PSG), and a 1 um active structural layer of silicon nitride. The mechanically active "drum" regions were defined by patterning the nitride with sets of etch access holes arranged into a hexagon array on a 1 mm pitch. The etch access holes in the samples tested were 5 microns in diameter, distributed in a square array with a 46 microns center-to-center pitch. Reactive ion etching was used to cut through the nitride into the sacrificial layer, then a timed isotropic etch undercut the active layer to release the freestanding circular drumheads. The top gold mirror, with roughly 95% reflectivity in the near infrared wavelength of interest, was deposited on the released structure.

An applied voltage between the membrane and substrate layers cause an electrostatic attraction which pulls the membrane from its normal flat state, producing a dip in the reflective surface wherever there exists a pocket in the PSG layer. The honeycomb pattern of pockets in the PSG layer creates the hexagonal array of dips in the gold layer. Each dip acts as a concave, reflective lens. The resonant frequency of this device was measured to be 160 KHz which is suitable for video transmission. Moreover, we can increase the device response to above 1 MHz by increasing the nitride film stress and drive voltage.

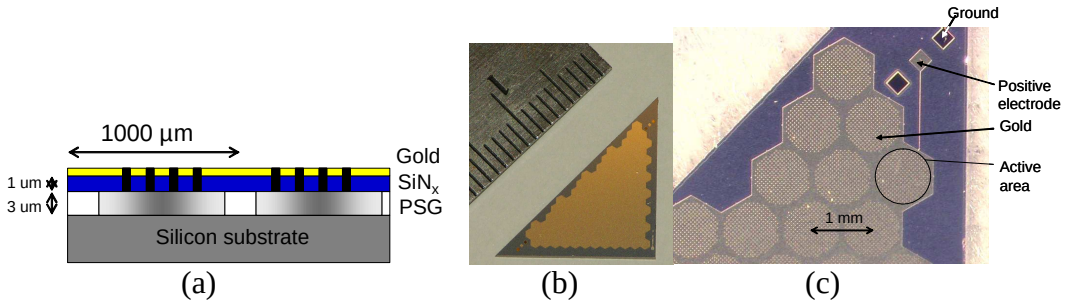

Figure 2.4: (a) Layered device diagram (b) fabricated die and (c) close-up of individual micromirror cells.

We first characterized the deformable mirror by substituting it as one of the mirrors in a michelson's interferometer. Thus, reflected 1550 nm light was combined with a plane wave to give an interference pattern corresponding to the deformations of our mirror. These patterns allowed us to extrapolate the profile of the deformable mirror surface, shown in Figure 2.5. The first experimental samples achieved a maximum sag of 0.55 µm with an applied voltage of 79 V, short of the intended 0.8 µm sag. This deformation limit is caused by an error in the deposition composition of the SiN_x layer, making the deformable membrane conductive and somewhat nonuniform in layer stress. This caused the deformation to be nonuniform on the large (10 mm) scale of the device, and also caused an electrical short circuit when we applied significantly more than 79 V to the device. A spare device was sacrificed to show that arcing from the short circuit punctured the membrane surface, rendering it useless as a reflective mirror. Although we could not produce greater than 0.55 µm deformations with this initial prototype device, all device problems can be corrected upon re-fabrication with a uniform non-conductive SiN_x layer.

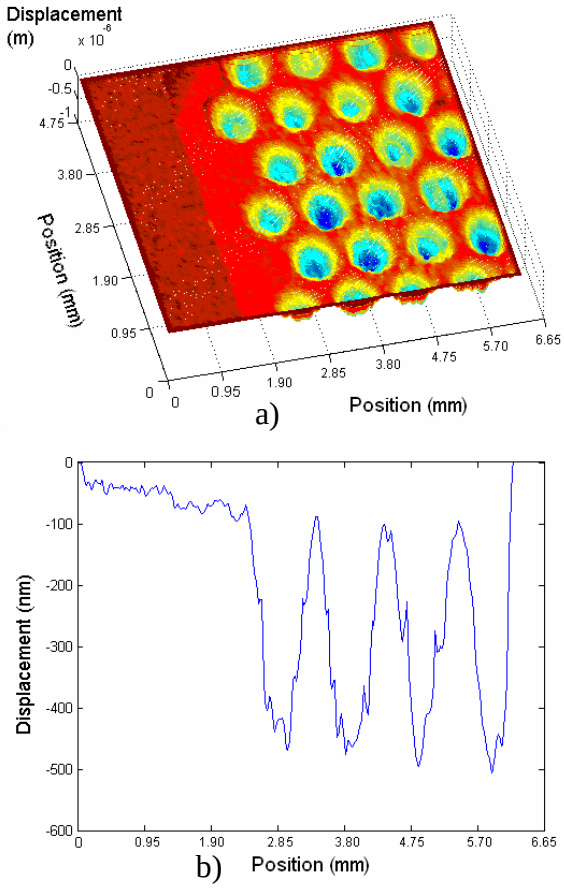

Figure 2.5: (a) Profile of the device surface after deformation, extrapolated from interferometry measurements. (b) Profile of the device deformation.

The device was illuminated with a collimated, 1460 nm to 1580 nm wavelength-tunable laser and the reflected light was propagated 6.6 m onto a white screen, effectively in the far field. The intensity pattern was captured on the screen by a Sensors Unlimited 320M InGaAs camera. Figure 2.6 a and b show the logarithmic far-field intensity pattern before and after 0.55 μm mirror deformation with near normal illumination by 1520 nm wavelength light. These patterns resemble the patterns predicted in the simulations; a repetition of the zeroth-order reflected light in

a hexagonal array that is confined by a circular envelope. The diffracted spots are noticeably smaller because the mirror was illuminated with an apodized Gaussian beam profile which was smaller than the aperture of the mirror.

Figure 2.6c and d correspond to the intensity line profiles along the horizontal white lines as indicated. These line profiles reveal the relative intensities of the diffraction patterns. Here, approximately 90% of the power has been diverted from the original beam into the hexagonal pattern of surrounding beams, yielding 10:1 extinction. These results agree with the theoretical predictions made earlier in this paper. Furthermore, diffraction patterns produced using 1460 nm and 1575 nm light created far field diffraction patterns which were indistinguishable from these results, thereby demonstrating wavelength insensitivity.

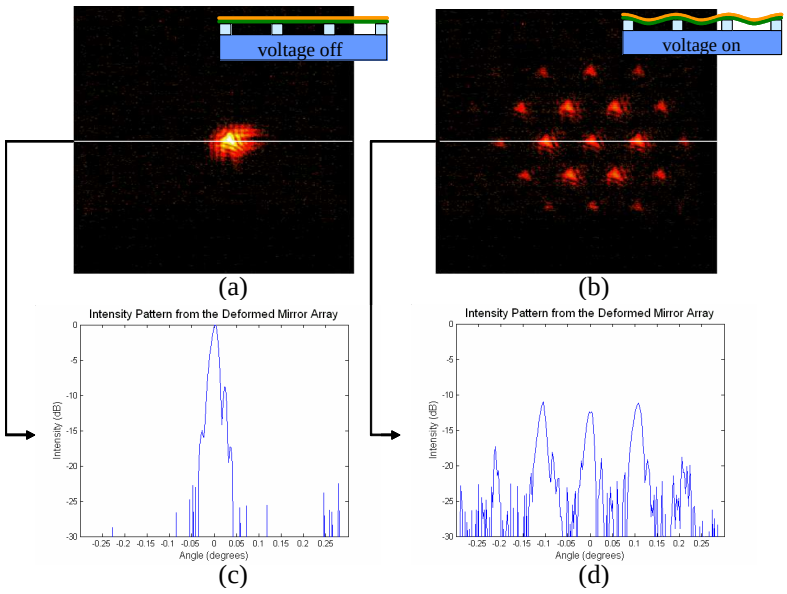

Figure 2.6: Experimentally measured far field intensity patterns from a triangular-aperture device in the (a) zero voltage (flat mirror) and (b) off state, and their line profiles (c) and (d). These far field patterns were observed using 1520 nm laser light. Photos and plots both use a logarithmic intensity scale.

Figure 2.7 shows the measured line profile for the same far-field diffraction pattern when the deformed mirror was illuminated with a 14 nm bandwidth ASE optical source centered at 1532 nm, instead of a monochromatic, coherent laser beam. There is a strong correlation between Figure 2.6d and Figure 2.7; there are distinct diffraction orders which are separated by approximately 0.11° divergence and the zeroth order beam experiences approximately 11 dB extinction. This example further demonstrates the wavelength insensitivity of the deformable mirror; moreover, the deformable mirror functions with temporally incoherent white light.

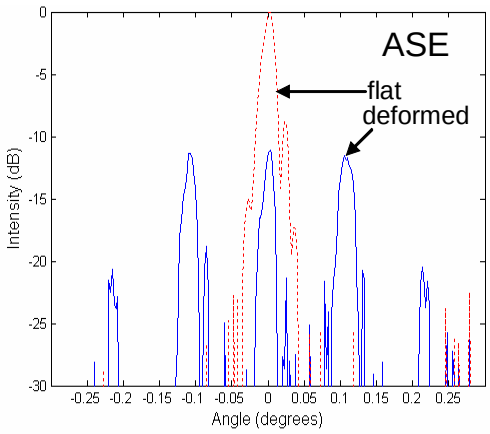

Figure 2.7: Line profile of the mirror far-field diffraction pattern using incoherent illumination.

Experiments verified that our device followed the angular response predicted by our calculations up to its maximum 0.55 µm achievable deformation, but a deformation of 0.8 µm would be necessary to observe significant diffractive effects at incident angles greater than 40°.

To study the temperature dependence of our devices, a deformable mirror was mounted on a thermo-electric cooler (TEC) with an attached thermistor. We used a deformable mirror with 50% (instead of 75%) deformable area because these mirror types were readily available for "test to destruction" sacrificing. As you might expect, these 50% active deformable area devices require more voltage and produce less extinction. The TEC and thermistor allowed for active temperature control during these experiments. The mirror was illuminated with a 1550 nm laser at near normal incidence and the reflection was propagated 6.6 m into a collection lens and detector. The detector aperture isolated the zeroth order diffracted beam and measured its

extinction ratio as the device was driven with an 85 V amplitude binary signal at 10, 50 and 100 kHz. Figure 2.8 shows a decrease in the extinction ratios as the device temperature was increased. Further interferometry measurements of the mirror surface profile revealed that thermal expansion resulted in the bending of the overall surface. The consequential curved mirror surfaced reduced signal power in the high signal power (flat mirror) state but had less of an effect on the off signal level when the mirror was sagged. These changes account for the measured decrease in extinction and can be mitigated with better packaging. Using a similar device, we ramped the temperature to over 400°C with no visible impact. These results are compatible with previous measurements on membrane modulators, which were shown to operate in liquid nitrogen and at 400°C temperatures.

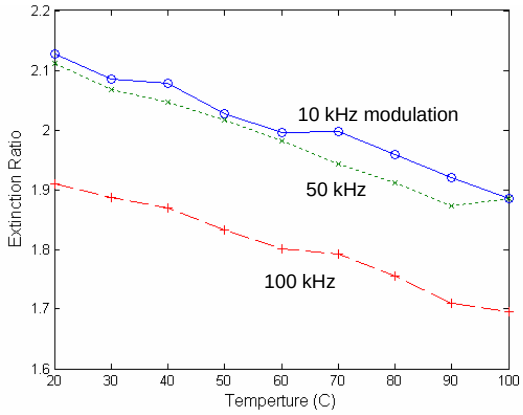

Figure 2.8: Optical contrast ratio (extinction) as a function of retro-modulator temperature. The modest decline in extinction comes from the thermally-induced curvature of the device mounted on the heater.

2.4 Experimental demonstration of the corner-cube retro-modulator

The deformable mirror was assembled with fixed dihedral (90° angle) gold mirrors to form the corner cube retromodulator shown in Figure 2.9. We apply voltage to the deformable mirror through the electrical leads displayed at the top of this photograph. We mounted the deformable mirror on a tilt stage to allow accurate alignment with respect to the other two mirrors.

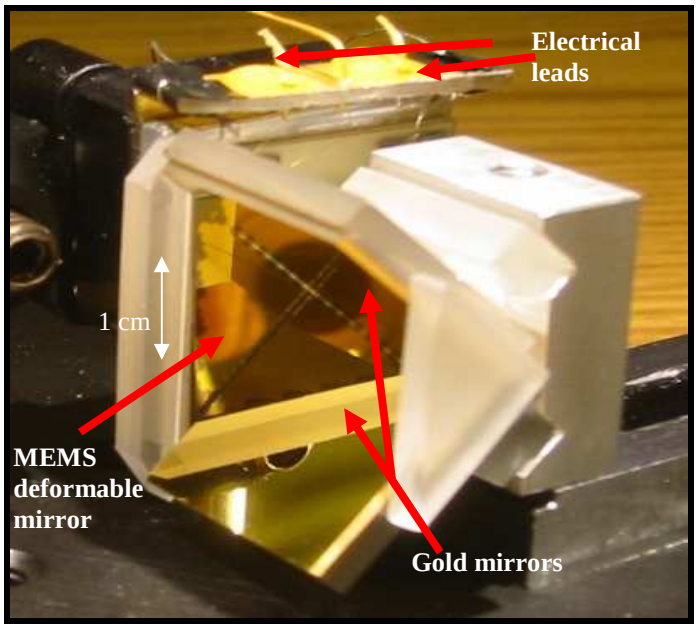

Figure 2.9: Photograph of the assembled MEMS deformable mirror retro-modulator

Light must strike each of the three mirrors for retro-reflection. Therefore, there are six different paths for retro-reflection; each path corresponds to a different permutation of reflections off of the three mirrors. Figure 2.10a is a photograph of the

retro-reflected light at the retro-reflector mirror surfaces. It is combined with a slightly tilted plane wave which creates the observable interference fringes. The reflected light is divided into the six sections by gaps between mirrors of the corner cube; each section corresponds to one of the six different paths of light. Each of these paths encounters the deformable mirror once, adding phase modulation to the entire signal. Figure 2.10b shows the retro-reflection from the deformed device, revealing at least λ/2 phase distortion over the entire return beam.

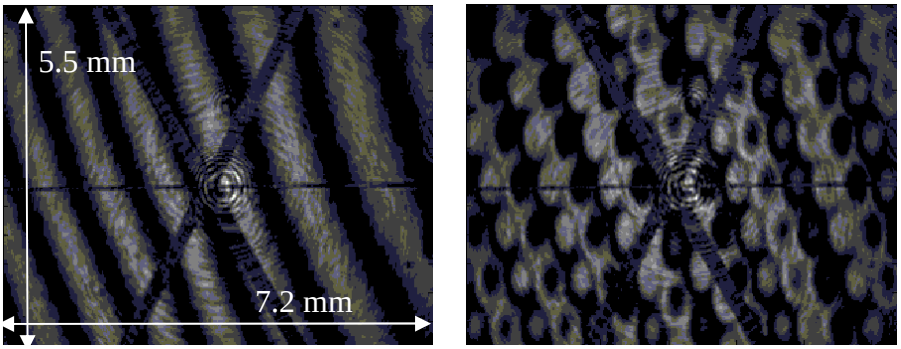

(a) (b)

Figure 2.10: Interferometer photographs of the retro-modulator surface (a) flat (λ/9 aberration) and (b) deformed (>λ/2 aberration).

Figure 2.11 shows the far-field intensity pattern created by the retro-modulator with normal incident light into the corner-cube (each mirror normal is oriented at the same angle, 54.7°, from the incident light). Recall that diffraction from only the deformable mirror created a single hexagonal array diffraction pattern. Figure 2.11 shows several hexagonal arrays patterns that are rotated by different angles and superimposed. This is a result of the different paths which the light can travel within the retro-reflector each creating a diffraction pattern of their own. Depending on the

order of reflections, the phase distortion acquired from the deformable mirror can become inverted at various angles with subsequent reflections within the corner-cube.

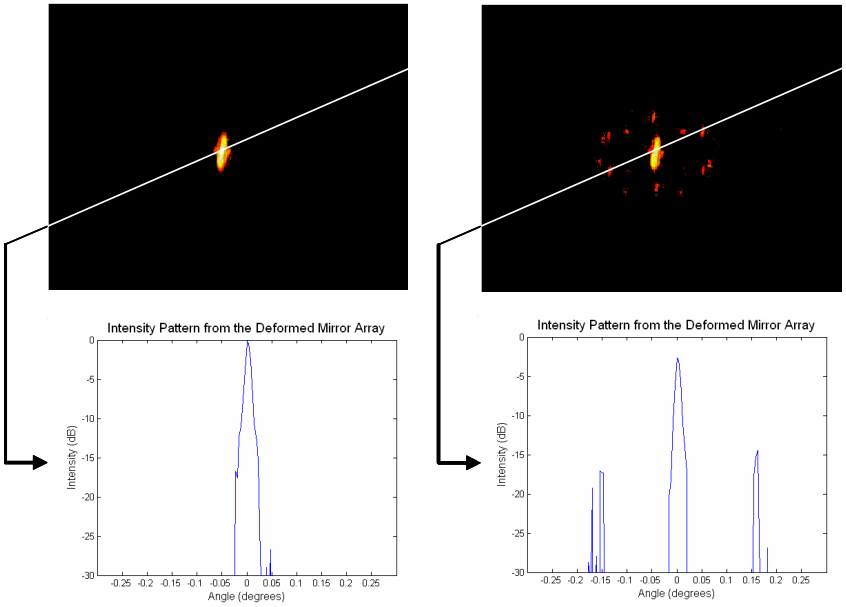

Figure 2.11: Far-field diffraction pattern from the retro-modulator with an applied voltage of (a) 0 V and (b) 79 V. Photos and plots both use a logarithmic intensity scale.

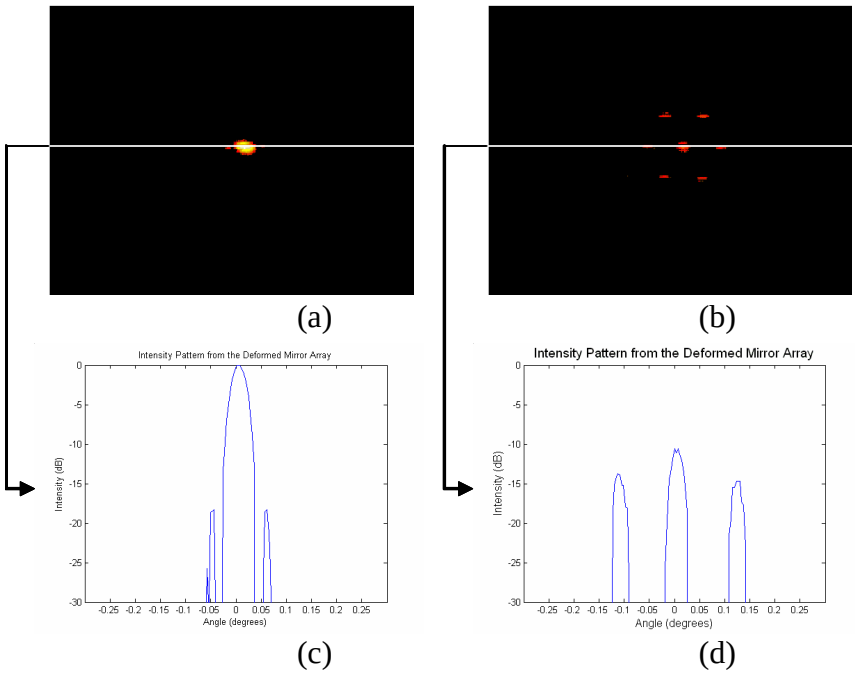

Figure 2.12: Far-field diffraction pattern from the retro-modulator, tilted 31.7° towards the deformable mirror, with an applied voltage of (a) 0 V and (b) 79 V. Photos and plots both use a logarithmic intensity scale.

To achieve better contrast, the corner-cube is tilted 31.7° towards its deformable mirror side such that the incident rays strike the deformable mirror at 23°. Figure 2.12 shows the resulting far-field diffraction pattern after this adjustment is made. This orientation is more indicative of minimum performance when using multiple MEMS mirrors instead of a single MEMS mirror with two fixed glass mirrors.

2.4.1 Modulation time response

The retro-reflecting modulator was driven by a square signal with 79 V amplitude. In these experiments, the retro-reflector was rotated by 31.7° towards the

deformable mirror for high extinction. The retro-reflected signal was separated from the incoming beam path using a 50/50 IR beam splitter and collected by a Fourier lens 6.6 m away. A detector was placed in the Fourier plane of this lens on axis and only captured the zeroth order diffracted spot. Figure 2.13 shows the detected signal intensity. This shows 7.1:1 signal contrast with rise and fall times of 4.3 µs and 6.8 µs respectively. Recall that the deformation was limited by the maximum deformation (0.55 µm) that could be achieved by our samples. According to Figure 2.3, from our calculations, a correctly fabricated device will achieve 17 dB extinction with 0.8 µm deformation.

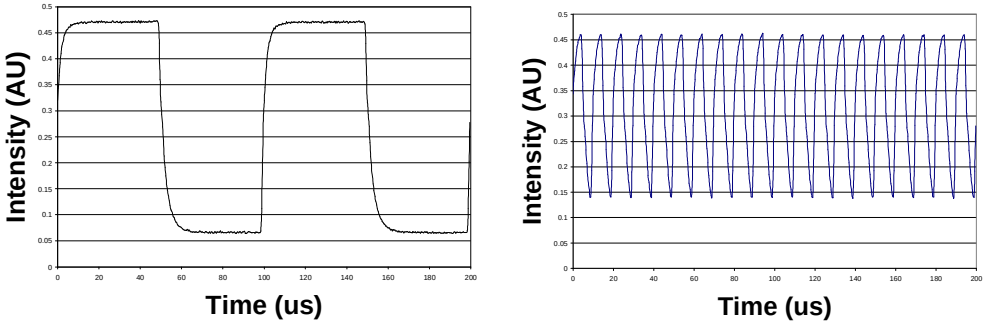

(a) (b)

Figure 2.13: Received (a) 10 kHz and (b) 100 kHz signal from the retro-modulator 6.6 m distant.

2.4.2 Angular Dependence

The retro-reflecting modulator is used in a FSO communication system to automate the alignment at one side of the link; therefore, retro-reflecting modulators must function at a wide range of incident angles. Accordingly, we tested the MEMS deformable mirror retro-modulator at a range of angles. Our simulations, shown in Figure 2.3**,** predicted a decrease in contrast with an increase in α, the angle between the incident light and the deformable mirror surface normal. We note that this angle, α, is not the same as the normal of the corner cube since each mirror is tilted 54.7° relative to the corner cube face. We measured the extinction ratios in relation to this angle and show these results in Figure 2.14 where both α and the tilt of the corner cube, β, are displayed. These results agree with our calculations of angular dependence and show 2:1 extinction from 23° to 58° for 10 kHz modulation. Thus, this particular device demonstrated a functional angular range of at least 35°. These extinction ratios are in strong agreement with the simulations presented in Figure 2.3. Based on these calculations, we expect that a correctly fabricated, fully deformable device can achieve higher extinctions and therefore, can operate with a much greater angular range.

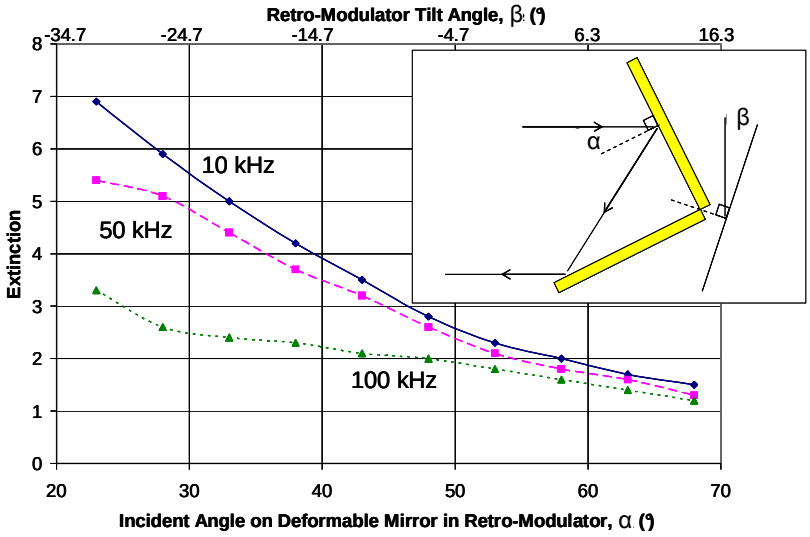

Figure 2.14: Extinction ratio achieved as a function of retro-modulator tilt angle.

2.4.3 Wavelength Dependence

Figure 2.15 shows the extinction ratio as a function of wavelength. It reveals constant extinction from 1520 nm to 1570 nm wavelength which is consistent with our calculations. This indicates that the MEMS deformable retro-modulator will reliably operate at a large range of wavelengths without measurable impact on contrast.

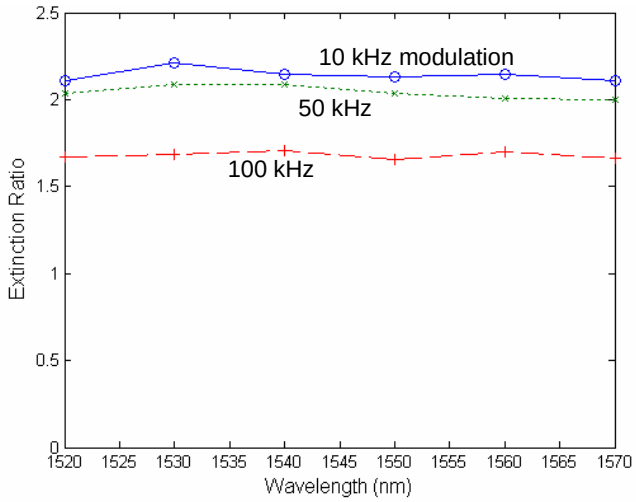

Figure 2.15: Extinction as a function of wavelength, showing essentially wavelength-independent contrast.

2.5 Conclusions

This chapter has described a novel MEMS retro-modulator for free-space optical communications and especially for remote telemetry applications. This retro-modulator combines excellent wavelength, angle and temperature insensitivity while maintaining scalability for large apertures and longer link distances. Our theoretical analysis of the MEMS deformable mirror accurately describes the device's diffraction performance in relation to the physical design of the mirror. The deformable mirror was fabricated and tested to verify the wavelength and angle insensitivity predicted by our calculations. We also demonstrated large thermal tolerance, observing consistent device performance from 20°C to 100°C. Finally, we assembled a single deformable micro-mirror array device into a prototype retro-modulator that demonstrated up to 7:1 extinction and modulation speeds up to 100 kHz.

The deformable mirror was designed to achieve greater deformations but was limited by the initial device fabrication run to a maximum mirror deformation of 0.55 µm as opposed to the design value of 0.8 µm. Future device fabrications with better control on the composition of the Silicon Nitride layer will enable better extinction ratios to extend the angular, temperature and wavelength operating range. Increasing the strain of the deformable membrane can increase the achievable switching speeds to 1 MHz.

This particular device is the first example of a class of optical MEMS components based on spatially segmenting the physical optical aperture into an array of smaller sub-aperture devices that require a correspondingly small physical movement to control the optical response. This allows the device to scale to very large physical apertures, limited only by the wafer size of device fabrication, and also enables a much faster mechanical response than would otherwise be possible. The particular design demonstrated here was an array of reflective micro-mirrors with variable focal length. This concept can be extended to other segmented structures, for example an array of planar tilt-mirrors, only providing that one state of the MEMS device is uniformly flat to within a fraction of a wave across the full device array.

The authors gratefully acknowledge support from Cubic Corporation and the Natural Sciences and Engineering Research Council of Canada. We also acknowledge PROsystems, Inc. for fabricating the gold mirror dihedral which we used as part of the prototype retro-modulator.

The text of Chapter Two, in part or in full, is a reprint of the material as it appears in the following publications:

- T. K. Chan, J. E. Ford, “Retroreflecting optical modulator using an MEMS deformable micromirror array”, J. Lightwave Tech., 24 (1), January 2006.

The dissertation author was the primary researcher and author. The co-authors listed in these publications directed and supervised the research which forms the basis for these chapter.

Chapter 3

Frustrated Total Internal Reflection (FTIR) Retro-Modulator

3.1 Introduction

One key purpose for using a retro-reflecting modulator is to eliminate the need for active alignment for one size of a free-space optical communication link. The retro-modulator described in the previous chapter had an operational field of view of 35°. For hollow corner cube retro-modulators, this is relatively large; however, this retro-modulator would still need to face the interrogator for retro-reflection to occur. Active control can be eliminated by using multiple retro-modulators to cover the entire 360° planar field of view. This means that 11 of our MEMS retro-modulators would be needed for completely passive alignment. Moreover, more devices would be required to account for a full 3-dimensional spherical field of view. With this consideration, one can understand the appeal of a large angular ranged retro-modulator.

One method for creating a larger angular field of view is by introducing a solid, high index retro-reflector. Unlike a hollow corner-cube retro-reflector, light reflects within the device in a high index material such as silicon. When light strikes the entrance face of the corner-cube retro-reflector, refraction bends the light towards

the normal direction of the corner-cube. This is shown in Figure 3.1 where the same incident ray of light is seen escaping a hollow corner cube while retro-reflecting within the solid one.

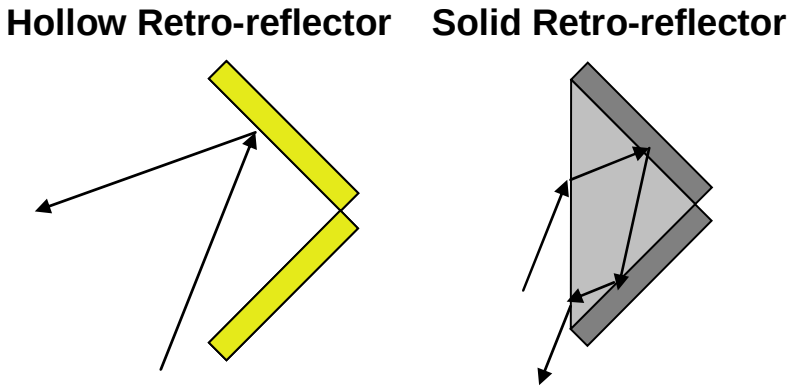

Figure 3.1: Illustration of the increased field of view which is caused by selecting a solid, high index corner-cube retro-reflector.

If we consider a 2-dimensional corner cube, as depicted in Figure 3.1, we can calculate the amount of power returned by calculating the retro-reflecting area which is visible to the optical source. We calculated the returned light from both a hollow corner-cube, and a solid corner-cube using the index of silicon. The results from this calculation are shown in Figure 3.2 where the amount of reflected light is plotted as a function of incident angle. Here, we assume that there are no losses due upon refraction or reflections. Figure 3.2 shows that by using a solid corner cube, we can double its angular range; the full-width-half-max value has increased from 45° to 90°.

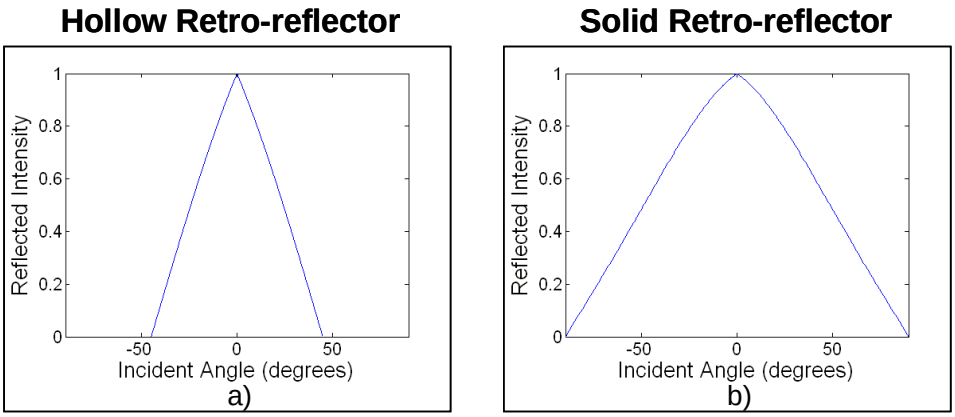

Figure 3.2: The amount of retro-reflected light from a a) hollow and b) solid silicon corner cube retro-reflector as a function of incident angle.

The reflection surfaces can be coated with a metal reflector, or they can be left bare since total internal reflection (TIR) will occur at incident angles above the critical angle. When TIR occurs, an evanescent wave is created outside of the medium, or in this case, the silicon corner-cube. Reflection occurs as the evanescent wave couples back into the high index medium. This process is theoretically 100% reflective but drops off sharply below the critical angle. In the context of the incident angles within a corner-cube, the condition for TIR is easily met and there is virtually no power lost upon reflections.

In the previous chapter, we accomplished modulation by deforming one of the mirrors to distort the reflection. For that case, the mirror was fabricated using MEMS processes where a thin, flexible layer could be deformed by electro-static attraction. In the case of the solid silicon retro-reflector, this is not possible since nothing inside the corner-cube can be mechanically manipulated. To modulate the reflected signal from a solid corner-cube retro-reflector, a method of external manipulation is needed. This has been accomplished previously with external electro-optic [25] acoustro-optic

[26] and quantum well [34] modulators. These methods modulate the optical beam while it is outside of the retro-reflector.

Rather than applying modulation to the optical beam outside of the corner-cube, we take advantage of the fact that the light undergoes TIR at the uncoated faces of the corner-cube. One of the requirements for TIR to occur is that there is a low index space for the evanescent wave tail outside of the medium. If, however, this evanescent wave encountered another high index medium, TIR would no longer occur and the optical wave would be transmitted into this new medium. This process is appropriately known as FTIR. We can use a similar MEMS arrangement that was employed in our hollow retro-reflector to move an absorbing material in and out of FTIR range.

3.2 Frustrated Total Internal Reflection

TIR occurs when a wave strikes an interface from a medium with a higher index of refraction at an incident angle greater than the critical angle. Under this condition, the transmitted electric wave found by the Fresnel equations is given by Equation 3.1 where E is the, θ_i is the incident angle, n_{ti} is the ratio of indices of the external to the internal medium, y is the direction perpendicular to the interface and x is the direction parallel to the interface.

$$\vec{E}_t = \vec{E}_{0t} e^{\pm \beta y} e^{i(k_t x \sin\theta_i / n_{ti} - \omega t)} \tag{3.1}$$

$$\beta = k_t \sqrt{\frac{\sin^2 \theta_i}{n_{ti}^2} - 1}$$

Eq. 3.1 describes the evanescent wave that is created upon TIR. There is an exponentially decaying factor in the y-direction coupled with a resonating surface wave along the interface. Since this wave cannot maintain power, the surface wave creates a reflection back in the initial media. Our goal is to capture the light and pull it out of the media during TIR. For this purpose, the decaying factor, β, is important here because it gives us the extent of the field outside the solid corner-cube. This is the portion of the field which we must manipulate in order to achieve FTIR.

The evanescent field can be pulled out of the corner-cube by absorbing it with another solid silicon substrate. This is done by bringing the absorber in contact with the evanescent field. Although we know the amplitude of this field from Eq. 3.1, this is not an indication of the amount of field that would be transmitted instead of reflected. To calculate the amount of light which is transmitted across the air gap, we treat the gap like a thin film and use characteristic matrixes of thin films [47] which are derived from Maxwell's equations. The characteristic matrix is given by

$$\begin{bmatrix} B \\ C \end{bmatrix} = \begin{bmatrix} \cos\delta & \frac{i\sin\delta}{\eta_1} \\ i\eta_1 \sin\delta & \cos\delta \end{bmatrix} \begin{bmatrix} 1 \\ \eta_2 \end{bmatrix} \tag{3.2}$$

where

$$\delta = \frac{2\pi n d \cos\theta}{\lambda} \tag{3.3}$$

and

$$\eta = \gamma n \cos\theta \text{ for s-polarizations} \tag{3.4}$$
$$\eta = \frac{\gamma n}{\cos\theta} \text{ for p-polarizations}$$

where a subscript denoted the corresponding layer. Here, n is the index of refraction for the media, d is the thickness of the film and θ is the angle which the light travels in that layer. Multiple layers can be accounted for by multiplying their corresponding matrixes (the first matrix on the right hand side of Eq. 3.2 in the appropriate order. The reflectance and transmittance are given by Eqs. 3.5 and 3.6 respectively.

$$R = \left(\frac{\eta_0 B - C}{\eta_0 B + C}\right)\left(\frac{\eta_0 B - C}{\eta_0 B + C}\right)^* \tag{3.5}$$

$$T = \frac{4\eta_0 \,\mathrm{Re}(\eta_m)}{(\eta_0 B + C)(\eta_0 B + C)^*} \tag{3.6}$$

The most effective way to get transmission from FTIR is to use an index matched substrate to collect the evanescent wave. For our purposes, our corner-cube retro-reflector will be made of silicon since it has a high index of refraction (n = 3.628) and it does not absorb light in the C-band range. Using Eq. 3.6 for the case of an air gap between two silicon pieces, we calculated the amount of TIR across the air gap at the nominal angle of a corner-cube, 54.7°. This result is shown in Figure 3.3 where we require a mechanical translation of approximately 200 nm to go from total reflection to near zero reflection.

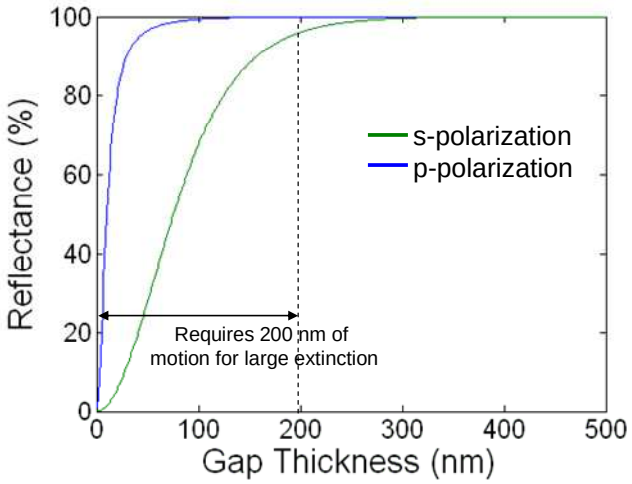

Figure 3.3: Calculated TIR from an air gap between two silicon substrates at 54.7° incident angle. This is shown as a function of the spacing between the substrates and gives an indication of the gap size change that is needed for mechanical modulation by FTIR.

To have absolutely no reflection, the substrates would need to be in contact with each other. Contact is not practical as any sort of repeated collision will expedite wear of the device. For our purposes, an extinction of 5:1 would suffice. Figure 3.3 reveals that this is achieved when the substrates are within 30 nm of each other. This close proximity is primarily due to the sharp drop off of the p-polarization component of light. In practical uses, we cannot take advantage of the polarization dependence since the orientation of this device and the angle of the incoming optical waves will be unknown.

Despite the sufficiency of near contact, this still presents a practical problem since close contact does not allow for much error in the motion. If electrostatic attraction, like that which was used for the MEMS modulator in Chapter 2, was the method for modulation, the close proximity would run the risk of the electric current

arcing across the gap. As seen with the MEMS modulator, the arcing would result in the destruction of the device.

Thin-film coatings offer a potential solution to this problem. Anti-reflection coatings have been fabricated where destructive interference eliminates any back-reflected light. In this case, the amount of light which is collected by the parasitic substrate can be tunneled back into the corner-cube to destructively interfere with the internally reflected optical power.

We used the characteristic equations shown above to calculate the behavior of an anti-reflection coating designed for FTIR. The assembly examined consisted of the structure shown in Figure 3.4. Here, the parasitic substrate is shown on below the air gap separating the two pieces. 1550 nm light is shown striking the interface at the nominal angle for a corner-cube retro-reflector. At the interface, the light splits as some of it tunnels across the gap while the rest is transmitted. The thin film of TiN ($n = 3.1477 - 5.8429i$ at 1550 nm) embedded in the parasitic substrate reflects some of the light back towards the interface. A portion of the back-reflected light tunnels back into the corner cube to destructively interfere with the internally reflected power, thereby leading to extinction.

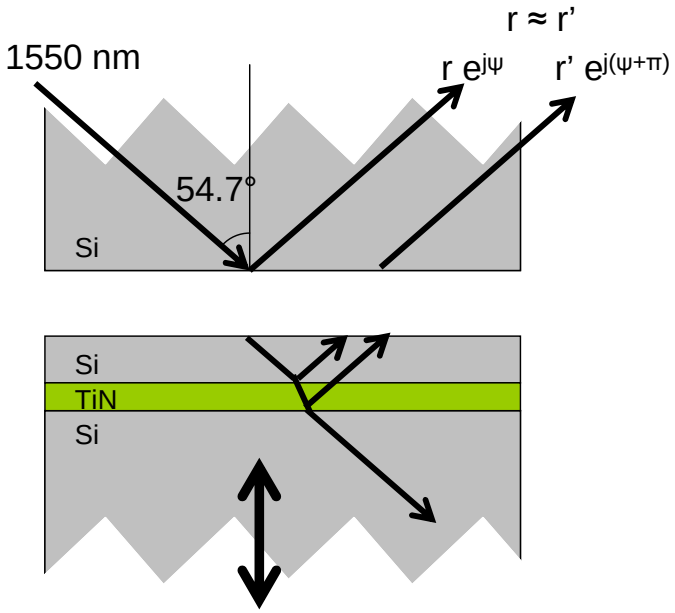

Figure 3.4: Thin-film anti-reflection coating for FTIR. This is the basic structure that was optimized for lowest internal reflection.

The design parameters are the thickness of the TiN layer and the thickness of the Si layer on top of the TiN. Since TiN absorbs C-band light, its thickness affects the amplitude of light which is reflected back while the thickness of the above Si layer determines the phase of light which is returned. This thickness will be adjusted so that the wave returned to the corner-cube is out of phase with the internally reflected light for maximum cancellation.

As an example, the film thicknesses were optimized to produce extinction for a 100 nm gap at the nominal angle for the corner cube. For these parameters, the most FTIR was generated with a 114.3 nm TiN layer and a 259.5 nm Si layer. The resulting reflectance is shown in Figure 3.5 when this parasitic layer is brought to within 100 nm of the corner-cube. At this large of a gap size, the s component of polarization can

be completely transmitted out of the corner-cube; however, the p component remains in the cube. Figure 3.6 shows that these antireflection coatings are also very wavelength insensitive; 70% of the s-polarized light still undergoes FTIR into the substrate within 100 nm of the designated wavelength.

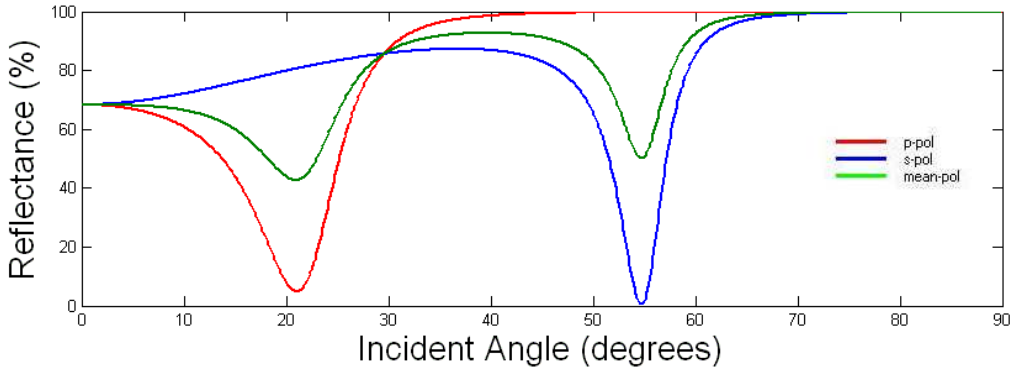

Figure 3.5: Calculated residual reflection after FTIR with an antireflection coating on the parasitic substrate. This is optimized for an incident angle of 54.7° to produce a maximum extinction when the gap size is 100 nm.

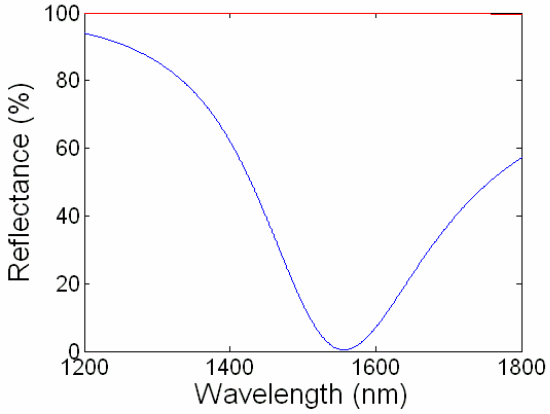

Figure 3.6: Wavelength dependence of FTIR with an anti-reflection coating.

Despite the strong angular dependence exhibited by the calculations displayed in Figure 3.5, the high index of the silicon corner-cube will bend the light towards the nominal angle of a corner cube. Moreover, a larger modulation contrast can be

obtained by using a modulator at all three reflective surfaces of the corner-cube. This was calculated using the beam path shown in Figure 3.7. The amount of internal reflection is shown in Figure 3.8 a and b. This includes the calculated "on" state which was found when the gap size is increased to 285 nm for near TIR within the corner-cube. The angles displayed here are now the external incident angles before entering the corner cube, plotted with respect to the normal of the entrance face. Along the z-axis of rotation, 2 to 1 contrast can be obtained for ± 15° field of view. In the x-y axis, we see that this contrast ratio will exist for the entire field of view.

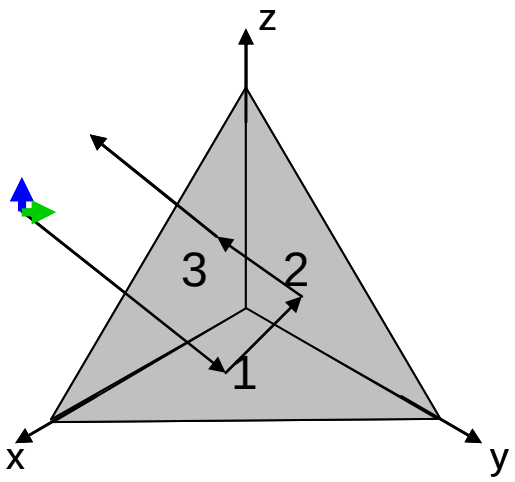

Figure 3.7: Beam path used in calculations of retro-reflector modulation contrast. In this arrangement, all three mirrors are FTIR modulators. The polarization of the light is divided into the blue and green components shown.

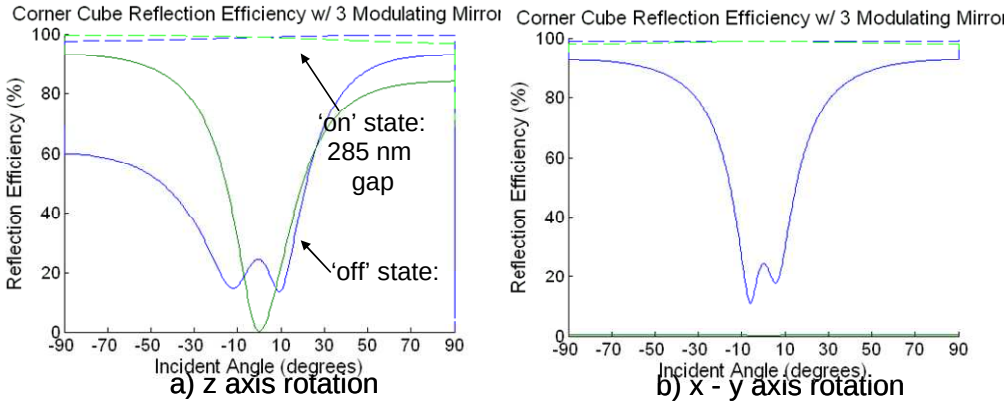

Figure 3.8: Reflection from the solid silicon corner-cube where all three mirrors experience FTIR. The green and blue lines represent the polarization directions shown in Figure 3.7 while the dashed lines represent the "on" state where the gap is increased to relieve FTIR.

A similar analysis was done when we designed for a 15 nm air gap. The best structure for this design consisted of a 3.7 nm TiN layer beneath a 243.1 nm silicon layer. The calculated results are shown in Figure 3.9 where 10:1 extinction is achieved along both directions of rotation.

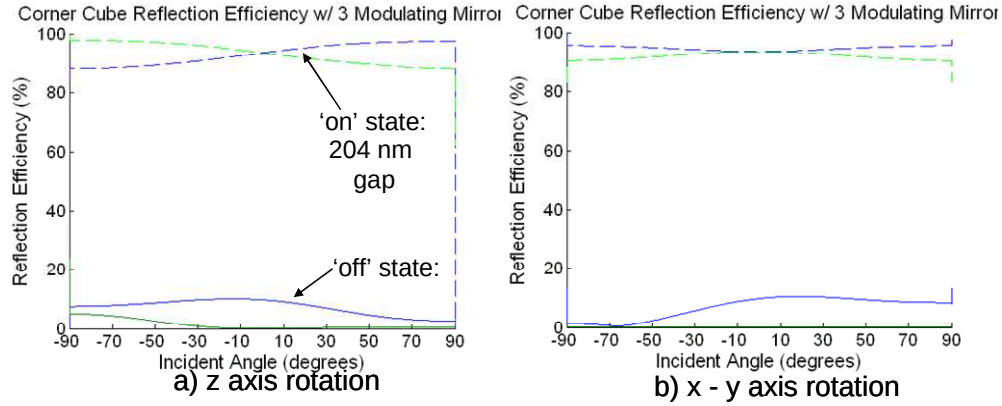

Figure 3.9: Reflection from the solid silicon corner-cube where all three mirrors experience FTIR. The green and blue lines represent the polarization directions shown in Figure 3.7 while the dashed lines represent the "on" state where the gap is increased to relieve FTIR.

These calculations of an anti-reflection coating show much promise in decreasing the proximity requirements needed for creating FTIR. In the scope of this

thesis, this technique was not experimentally pursued but shows worthiness for further investigation.

3.3 Extinction of the FTIR energy

Fabrication processes makes it convenient to use a silicon wafer as the substrates which collects the evanescent wave. Once FTIR has been achieved, a silicon wafer, which has two coplanar surfaces, would act as an etalon and return optical power back into the corner cube by the same FTIR phenomena. If this happens, then the light would return into the corner-cube at the same angle as TIRed light and retro-reflection would still occur. Thus, we need to extinguish the optical power once it has been transmitted across the air gap.

One method to absorb the infrared light is to embed chromium in the substrate. The index of refraction of chromium at 1550 nm light is 4.24 + i4.81. The imaginary component of this index shows that c-band light is highly absorbed by chromium. We introduce this chromium component to the parasitic substrate by coating the back with a chromium layer. With time and heat, the chromium readily diffuses into the silicon as described by Eq. 3.7 which is derived from Fick's Law. Here, Cs is the concentration of chromium at the edge of the substrate, x is the depth under the surface, t is the time and D is a diffusion constant. For chromium diffusing through silicon doped with boron, D is given by Eq. 3.8 [48] where T is the temperature and k is Boltzman's constant. Here, it is important that the chromium does not diffuse all the way to the front side of the wafer. This maintains the silicon index at the front side for index matching with the corner-cube which in turn allows for efficient FTIR.

$$C(x,t) = Cs \cdot erfc\left[\frac{x}{2\sqrt{Dt}}\right] \tag{3.7}$$

$$D = 0.01e^{-\frac{1}{kT}}\ cm^2/s \tag{3.8}$$

Figure 3.10 shows an example of the calculated concentration profile of chromium diffusing in silicon for 4 hours at 250 °C. The concentration level of 1 represents the concentration of chromium at the edge of the wafer.

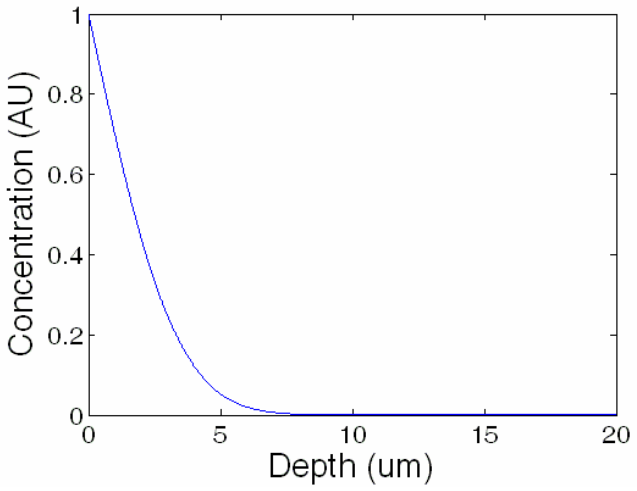

Figure 3.10: Calculated concentration levels of chromium diffusing into a silicon wafer. In this calculation, the diffusion time was 4 hours at 250 °C.

Accordingly, we coated a 100 μm thick silicon wafer with an approximately 230 nm thick layer of chromium. This wafer was then annealed at various temperatures to achieve various diffusion lengths.

We can estimate the amount of absorption within a silicon wafer by measuring the spectrum of reflected, normal incidence light. This is because a silicon wafer functions as an etalon and creates a period reflectivity spectrum. With the backside

covered by chromium, this etalon yields approximately 12 dB contrast between the peaks and valleys of the spectrum. When an absorbing agent lies within the silicon, the amount of light reflecting within the silicon wafer becomes attenuated. This results in a decrease in the contrast ratio in the reflectivity spectrum. This relationship is described by Eq. 3.9 where the variables are defined in Figure 3.11. Here, the variable T is included to account for any absorption which may occur in the silicon. T accounts for the amount of the field that is not absorbed in a double pass through the wafer (T = 1-a, where a is the fraction of light absorbed). If all of the light is absorbed within the wafer (T = 0), the etalon becomes a single surface reflector and the reflectivity will be equalized for all wavelengths ($I_r = E_0^2 r_0^2$).

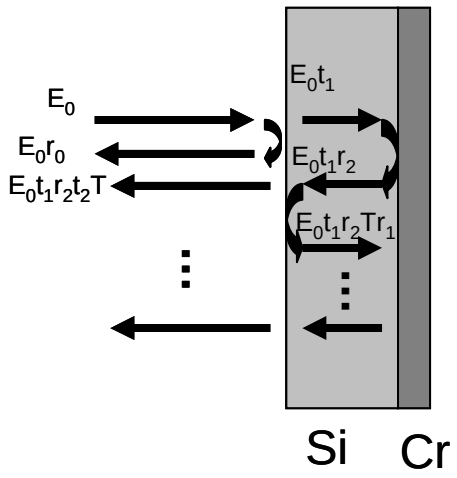

Figure 3.11: Diagram defining the variables involved in a Fabry-Perot Etalon. This etalon has two different interfaces, one between silicon and air and the other between silicon and chromium.

$$I_r = E_0^2\left[\left|r_0\right|^2 + \left|\frac{r_2 t_1 t_2 T e^{-i\delta}}{1 - r_1 r_2 T e^{-i\delta}}\right|^2 + 2 r_1 T t_1 t_2 \, real\left[\frac{r_2^*}{e^{-i\delta} - r_1 r_2 T^*}\right]\right] \tag{3.9}$$

A number of chromium coated wafers were annealed at various temperatures up to 240 °C for 4 hours. Their reflectance spectra are plotted in Figure 3.12 along with theoretical spectra having different levels of absorption within the silicon etalon. These curves are plotted at increments of 10% changes in absorption. In general, this reveals that annealing the wafer at higher temperatures increases the amount of absorption in the wafer by a very slight amount where all wafers had an estimated absorption within 5% of 55%. Since annealing the wafers appeared to have little effect on their absorption, our subsequent experiments used unheated, chromium coated silicon wafers.

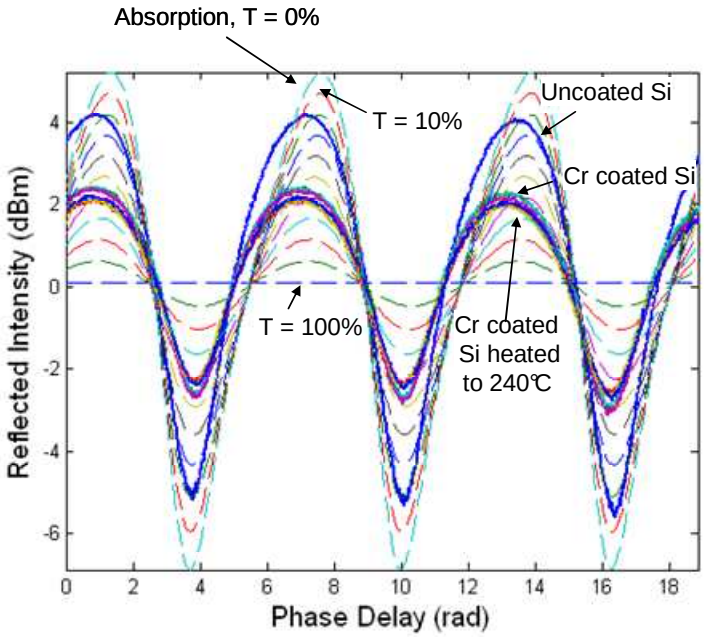

Figure 3.12: Measured reflectance spectra for silicon annealed at various temperatures. These are plotted along with theoretical spectra for an absorbing etalon at various absorption magnitudes. This allows us to estimate the amount of absorption in our wafers.

3.4 Nanopositioning

According to Figure 3.3, the change in FTIR becomes significant when the air gap decreases below 30 nm. To investigate the FTIR performance, this means that we require nanometer positioning accuracy. In MEMS, this is easily achievable with a properly fabricated device; however, for proof-of-principle experiments involving bulk components, nanometer positioning presents a challenge.

We used a Thorlabs Three Axis MicroBlock^{TM} Translation system to perform the motion in our system. This device operates using piezo-actuators controlled by voltage signals. By using small increments in voltage, we hoped to gain nanometer positioning accuracy. As shown in Figure 3.13, the vertical distance of a wafer

attached to the piezo-actuator is measured relative to a reference wafer using a MicroXAM Profilometer. This profilometer measures profiles interferometrically with 0.1 nm accuracy which is sufficient for our needs. In order to use this profilometer, the reference wafer needed to be coplanar with the controlled wafer.

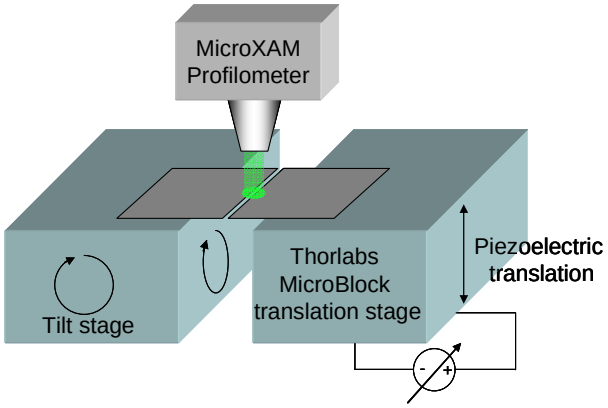

Figure 3.13: Setup used to calibrate the motion of the piezoelectric translation stage. Here, the vertical displacement between two wafers (arranged coplanarly) is measured by a MicroXAM Profilometer while the voltage applied to the piezo-actuator is adjusted.

Extraordinary steps were required because of the sensitivity needed for nanometer alignment. These included isolating the entire system for wind and temperature stability, gluing components in place, locating it on the ground floor, placing it on a large, air stabilized optical table and giving the system hours to settle before taking measurements. All of these things eliminate external disturbances which would lead to extraneous motions detrimental to our device characterization experiments.

Figure 3.14 shows the performance of the stabilized system as the voltage is monotonically increased. This shows two separate curves taken on different days

which demonstrate repeatability of motion and a near-linear response. Most importantly, we see that we have sub-nanometer positioning accuracy. Due to the nature of a piezo-electric motion system, hysteresis exists meaning that the linearity and repeatability of motion would not exist if the motion was reversed.

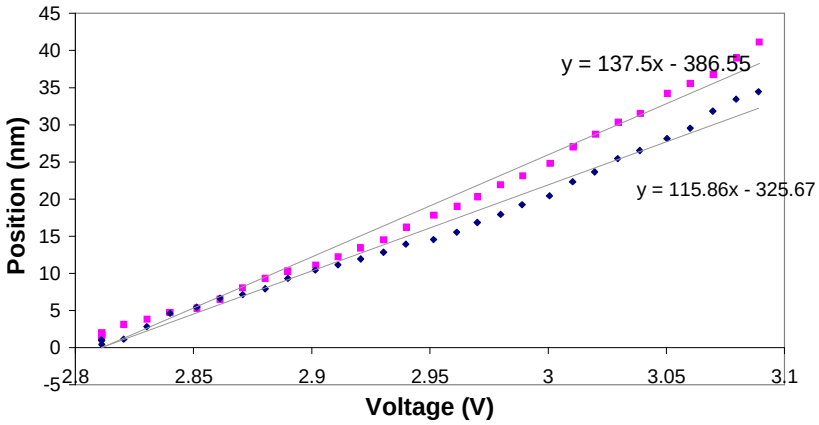

Figure 3.14: Response from the pizeo-actuator to an increasing voltage signal. The two curves were carried out on different days to demonstrate repeatability.

3.5 FTIR Setup

The calibration setup for the piezo-actuator was modified to demonstrate FTIR from a solid silicon corner-cube retro-reflector. The modifications are shown in Figure 3.15. Here, the wafer resting on the piezo-electric stage is replaced with a 450 nm thick silicon wafer coated with chromium underneath to act as the parasitic wafer with an absorbing element. The MicroXAM profilometer measured a +/- 6 nm surface roughness of this wafer. A 7.5 mm diameter corner-cube is supported by the reference wafer. The corner of the retro-reflector hangs off the reference wafer by approximately 1.5 mm so that the silicon absorber can be moved into proximity with the corner. In this setup, we can only achieve FTIR modulation at the small

overhanging surface of the corner-cube. Light which reflects in the corner-cube further from the over-hanging corner will experience a slight translation upon retro-reflection. Thus, this arrangement is sufficient for our proof-of-principle experiments as light reflecting off this overhanging corner will follow the same path back and comprise of most of the light returning to the collimator.

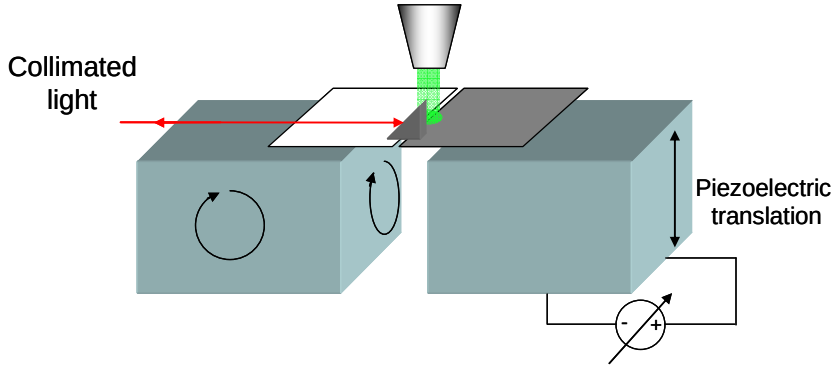

Figure 3.15: Mechanical portion of the setup used to measure FTIR when an absorber is brought within nanometers of the corner-cube retro-reflector.

The complete setup, including the optical components, is shown in the photographs in Figure 3.16. A beamsplitter divides the retro-reflected beam and sends it to a Sensors Unlimited 320M InGaAs IR camera and the collimator. The camera is focused on to the back plane of the retro-reflector so that we can see where FTIR is occurring. The light sent back into the collimator is circulated into a detector to measure the entire return signal. Also, the corner-cube is now held down a spring loaded clamp. This pressure keeps the substrate and bottom face of the corner cube in alignment. These sit on a stage which is tilted so that the reference wafer and the parasitic wafer are collinear.

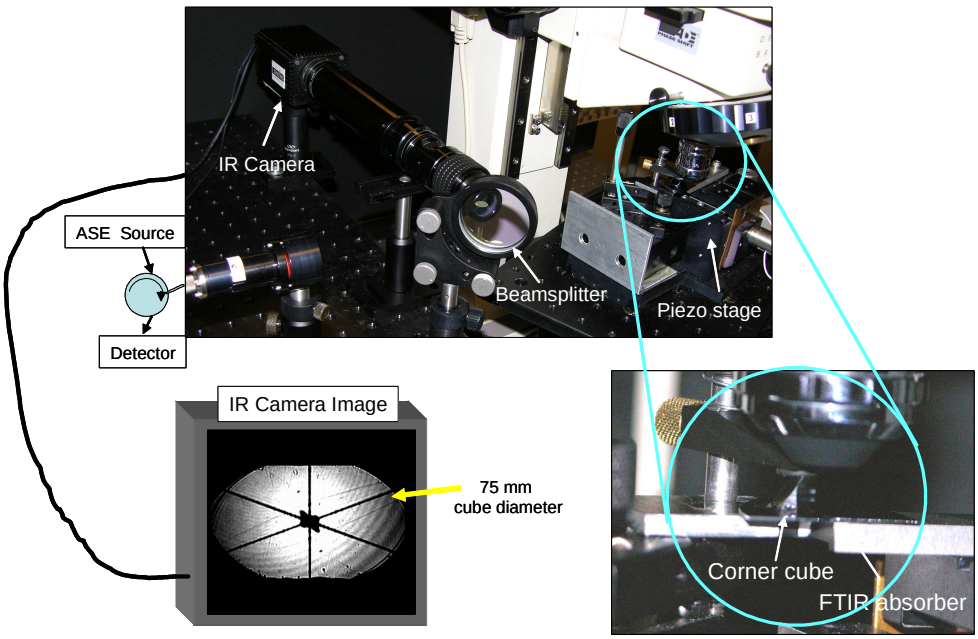

Figure 3.16: Photograph of the setup used to achieve FTIR in a solid silicon corner-cube retro-reflector. For the purposes of illustration, the housing used to stabilize the air and temperature in the setup is not present. The housing would shelter everything in the photograph except for the beam collimator which would project the beam through a small hole in the housing.

In our experiments, we increased the voltage applied to the piezo-actuator once it was brought into close proximity. No changes in the retro-reflected signal were obvious until contact was made. The point of contact was identified when the MicroXAM had shown that the reference substrate moved. Figure 3.17 shows the images of FTIR as the absorber is lifted into contact with the corner cube to the point where the corner cube has been slightly lifted. During this process, the voltage applied to the piezo-actuator is increased by approximately 167 V from the point of contact. Since the reference wafer moves during this process and there is an added load silicon absorber, we were not able to know the exact position of the silicon absorber during this process.

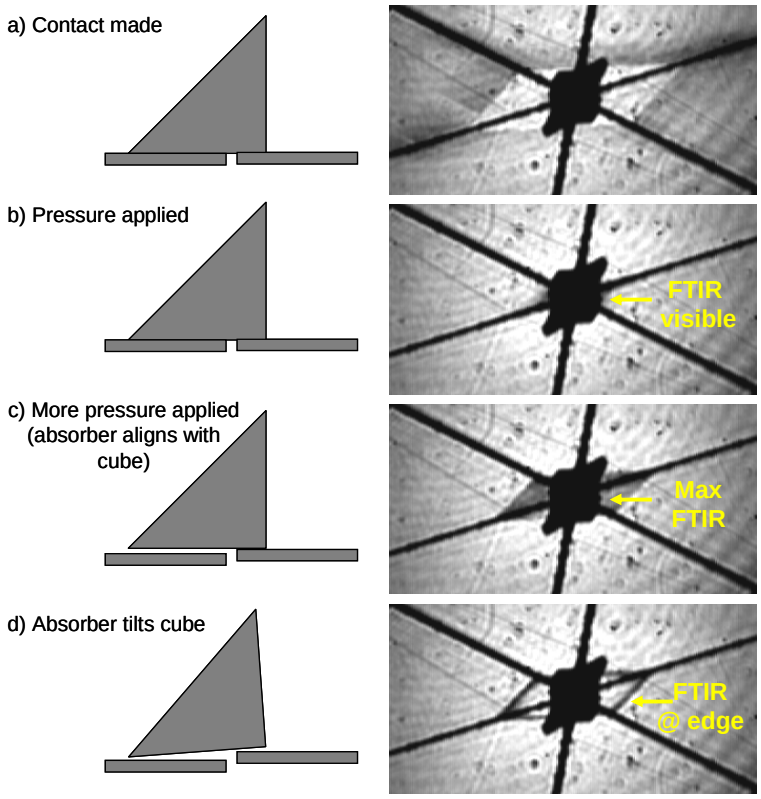

Figure 3.17: Images of the retro-reflected light as the voltage on the pizeo-actuator is increased. The dark center is caused by damage to the delicate corner of the retro-reflector. As the voltage to the actuator lifts the silicon absorber, the absorber a) makes contact with the corner-cube, then b) shows signs of FTIR. Eventually, c) the maximum amount of FTIR is achieved and then FTIR decreases as d) the corner-cube becomes tilted.

Figure 3.17 a) shows a dark box surrounding the center of the image. This dark area is caused by FTIR occurring between the corner cube and the silicon wafer holding it. As the absorber is lifted, FTIR does not occur until after there is pressure between the absorber and corner cube. We observe approximately 2:1 contrast until the corner-cube begins to tilt. Once the corner-cube is tilted, the darkest areas in the image, the areas where the pressure is the greatest, show approximately 5:1 contrast. This is contrary to our calculations which suggested that FTIR could be achieved

before contact. It is not clear to us why contact is necessary to observe modulation; however, our experiments have shown that the modulation of pressure between the absorber and the corner-cube is still effective. Since contact is required, this idea can no longer be applied to a MEMS device.

3.6 FTIR by Pressure

The results from the previous section suggest that we turn our attention to applying pressure between the corner-cube and silicon absorber to achieve FTIR. In a simple study, we simply placed the corner-cube retro-reflector on a 100 nm thick silicon wafer absorber. We chose a thinner wafer which is more flexible and susceptible to bowing, allowing for the pressure to spread evenly between the surfaces. We simply applied approximately 30 pounds of pressure to the top of the corner-cube using human force and observed the changes shown in Figure 3.18. This shows only localized regions of extinction which expand as more pressure is applied. The extinction in these areas is approximately 6:1. I conclude that it is necessary to flex the silicon absorber since the submicron proximity required to observe FTIR is smaller than the roughness and alignment tolerances of the surfaces.

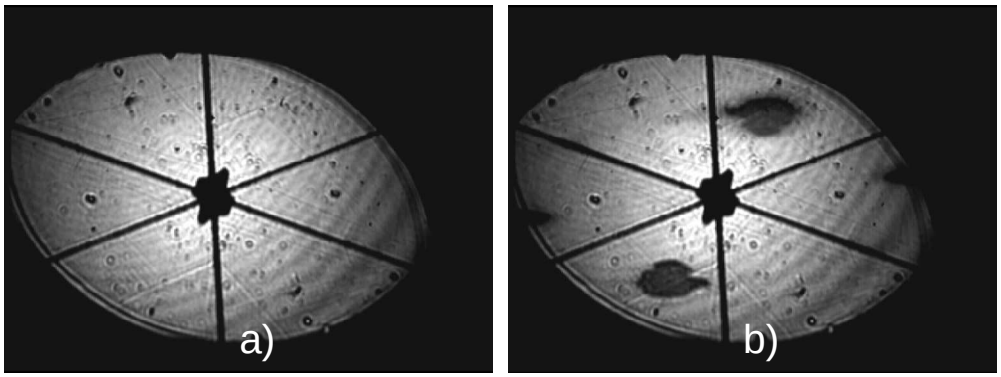

Figure 3.18: Images of the reflecting surface of the corner-cube retro-reflector as a) it rests on top of a silicon absorbing wafer and b) the corner-cube is pressed down onto the wafer.

We designed a housing to create a prototype device that operated on the principle of using pressure to generate FTIR. Although this strays from our original conception of a MEMS based, non-contact device, this new arrangement provides a less expensive alternative. A photograph of this device is shown in Figure 3.19 a).

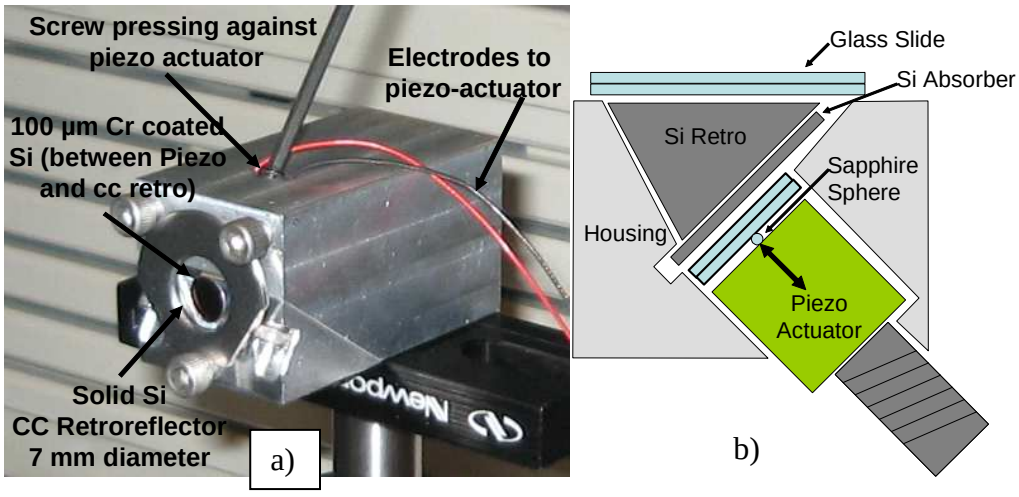

Figure 3.19: a) Packaged FTIR retro-modulator and b) the cross-section revealing mechanisms of modulation.

Figure 3.19 b) shows the cross section of this device which reveals its operation. Here, the piezo actuator rests in a cavity within the housing. A sapphire sphere is attached to the end of the piezo with NOA 68 UV cured epoxy. Two glass

slides are UV-cured together and rest on top of this sphere. This creates a glass layer totaling 2 mm in thickness. A thin layer of flexible, two toned epoxy holds the silicon absorber on the top slide. The glass slides are used to apply the force from the piezo uniformly across a large area of the silicon absorber. They are allowed to freely pivot on top of the sapphire sphere. This freedom allows the silicon absorber to align collinearly with the surface of the corner-cube retro-reflector. A biased pressure can be applied by tightening the screw located under the piezo. This will minimize the work needed by the piezo actuator.

We also used this device with a glass corner-cube retro-reflector which exhibits looser tolerances for FTIR due to its lower index of refraction. Calculations show that FTIR occurs in glass with approximately 100 nm gap separation. Consequently, the silicon absorber was also removed and the glass slides were used to collect the light. The bottom of the top slide was painted black to absorb the light and insure that it would not be retro-reflected.

The prototype was characterized using the setup photographed in Figure 3.20. The transceiver consisted of a Thorlabs, ASE-FL7002 broadband source which passed through an optical circulator before exiting the free-space collimator. The received signal entered the collimator, and was guided to a HP 81531A power sensor by the circulator. The beamsplitter, shown in Figure 3.20, directed 50% of the retro-reflected light into an SU 320 InGaAs camera. This camera allowed us to view the reflecting surface of the retro-reflector so that we could see the occurrence of localized FTIR.

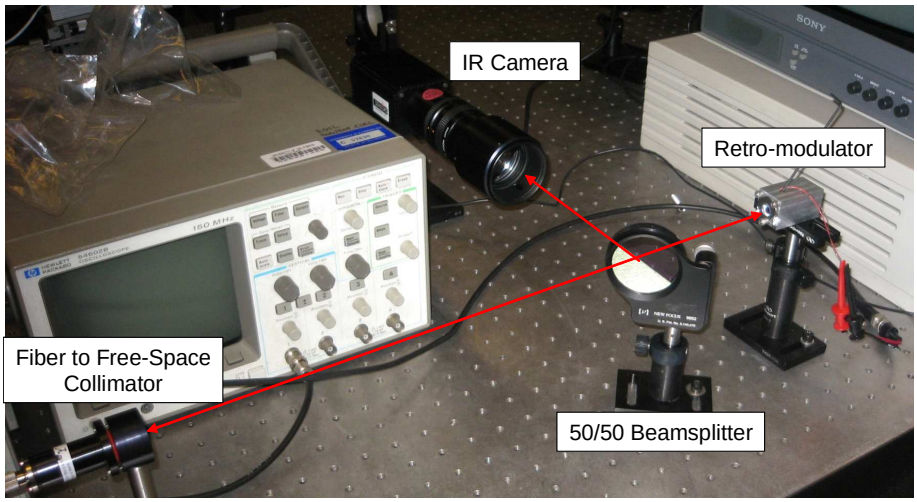

Figure 3.20: Photograph of the setup used to characterize the retro-modulator.

3.6.1 Driver Circuit

The piezo actuator had 600 nF capacitance. To achieve suitable switching speeds, a driver would require more power than was offered by standard signal generators and voltage amplifiers. One cost effective solution to this was to recycle the drive energy by using it in resonance with a similar capacitor. This was accomplished in a circuit designed by Justin Hallas. Its description follows.

"The purpose of this circuit is to modulate a fairly large capacitance at high voltage with minimum power. The basic idea of the circuit is that a dummy capacitor that is approximately the same capacitance as the modulating device stores the charge when the modulating device is in a low voltage state instead of discharging to ground. This is accomplished with an inductor and switch between the two capacitors. When the switch closes, the energy is resonantly transferred from one capacitor through the inductor to the other capacitor. Two unidirectional transfer paths between the

capacitors are implemented such that the only requirement for full transfer is that the switch be closed at least half of the resonant period. Since losses exist and the Q of the resonant circuit is finite the capacitors must be recharged periodically, but only a small fraction of the total energy needs to be re-added."

The mismatch in capacitance between the dummy capacitor and the piezo actuator resulted in more losses and more energy that needed to be re-added. Thus, the achievable voltage amplitudes and speeds were limited as shown in the following results.

3.6.2 Experimental results

Extinction could be seen simply by tightening the screw. This could be done to the point of failure where cracking would result in one of the components. In failed experiments, cracking occurred in the corner-cube retro-reflector, the silicon absorber or the glass slides transferring the force from the piezo. Therefore, the force was limited to an arbitrary amount, depending on the condition and arrangement of the components. FTIR can be seen with the maximum amount of pressure applied in Figure 3.21. This shows localized and non-uniform extinction of approximately 13 dB near the central region. This occurs along an edge of the corner-cube, suggesting that there is still some linear tilt between the corner-cube face and the silicon absorber.

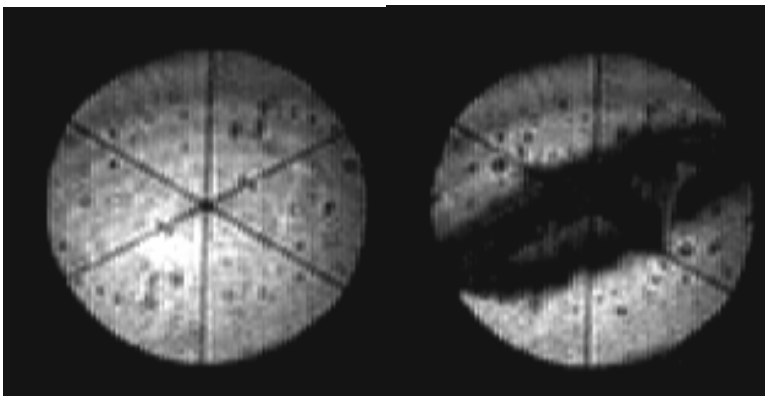

Figure 3.21: Image of the silicon retro-reflector focused on the reflecting plane when pressure is applied (left) and released (right).

Figure 3.22 shows the reflection surface when modulation is done on a glass retro-reflector. This shows FTIR occurring over the entire aperture where the extinction in these areas is approximately 10.5 dB. This is expected since glass does not confine light as well as silicon, and it is therefore easier to pull out of the corner-cube.

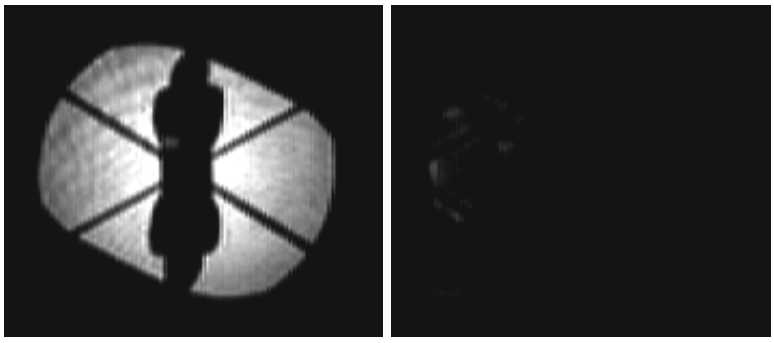

Figure 3.22: Image of the glass retro-reflector focused on the reflecting plane when pressure is applied (left) and released (right).

The signal received by the optical detector, shown in Figure 3.23, shows that signal modulation is achieved. Figure 3.23 was taken with a silicon retro-modulator at

500 Hz and 10 kHz modulation with the drive signals also displayed. These drive signals were taken at the maximum amplitude achievable by the drive circuit at that frequency. They are not true square waves; rather, they contain an artifact resulting from the driving method.

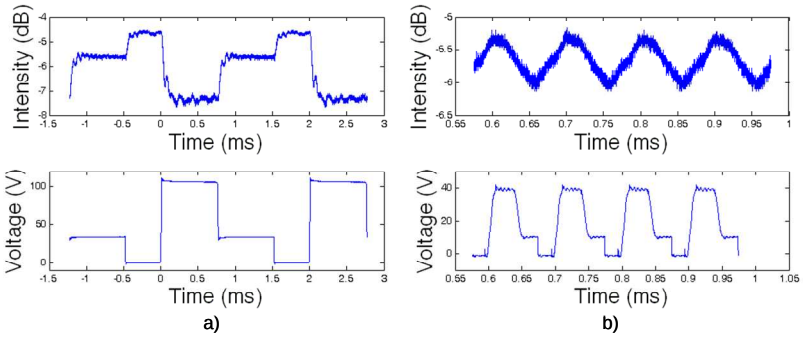

Figure 3.23: Optical signals from the silicon retro-modulator measured with the drive voltage signal for a a) 500 Hz and b) 10 kHz signal.

The same measurements were done with the glass retro-modulator and the results are shown in Figure 3.24. As expected, higher modulation depths are easier to achieve. The maximum depth observed was 8 dB shown in Figure 3.24 a).

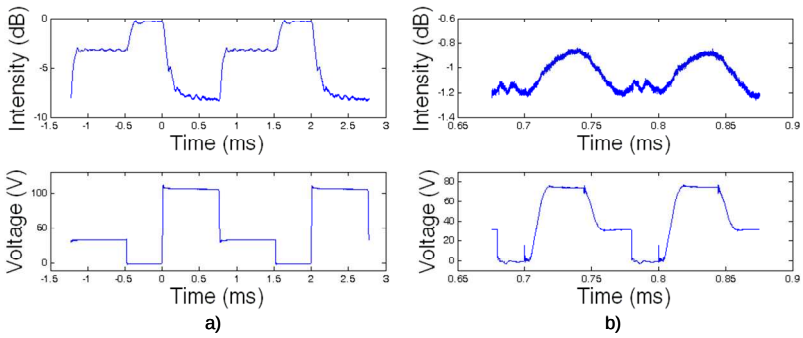

Figure 3.24: Optical signals from the glass retro-modulator measured with the drive voltage signal for a a) 500 Hz and b) 10 kHz signal.

Although we were not able to achieve the same voltage amplitudes at higher speeds, we can still extrapolate the modulation limits inherent to our modulator design. Figure 3.25 shows the relationship between the extinction and the drive voltage amplitude over a range of drive speeds using a silicon retro-reflector. The higher frequencies were not run at high voltages because the drive circuit could not provide enough power. Regardless, we can observe a drop in modulation ratios beginning at speeds of a few kilohertz.

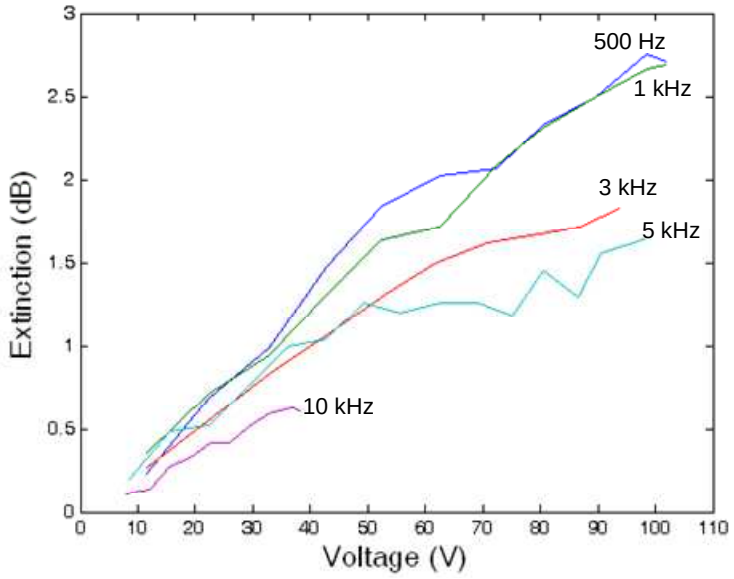

Figure 3.25: Relationship between the modulation ratios and the voltage for the silicon retro-reflector at different frequencies.

Figure 3.26 shows the measurements taken with a glass retro-modulator. As seen before, the glass retro-modulator achieved higher modulation depths; however, it follows a nearly identical trend of decreasing modulation as the signal frequency increases. One possibility for this decrease is in the response of the piezo actuator.

Although the piezo actuator is specified with a resonant frequency of 135 kHz, its response at lower frequencies is not documented. Another possibility lies in the transient response of the mechanics used in our device. When the pressure is applied, a mechanical deformation occurs. The motion required for this deformation may also limit the device speed.

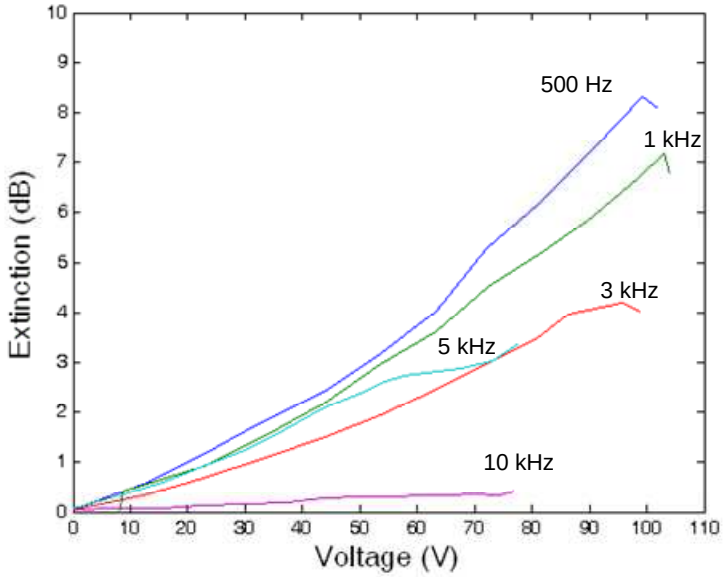

Figure 3.26: Relationship between the modulation ratios and the voltage for the glass retro-reflector at different frequencies.

The main advantage of using a silicon retro-reflector over a hollow MEMS retro-reflector is in the greater angular range associated with the refraction into the device. Figure 3.27 shows are experimental demonstration of this angular consistency in both extinction and overall insertion loss. In these experiments, the bottom surface of the corner cube experienced FTIR while it was rotated around a vertical axis. This modulator was run with a 500 Hz signal with 80 V amplitude. As expected, the power returned from the retro-reflector remains within 3 dB of the maximum power up to

±70°. The extinction gradually decreases with higher angles. This is to be expected since this would increase the angle hitting the FTIR interface, thereby creating more TIR. The other corner-cube surfaces may experience a decrease in incident angle; therefore, the contrast may also increase if the FTIR occurred on the appropriate surface.

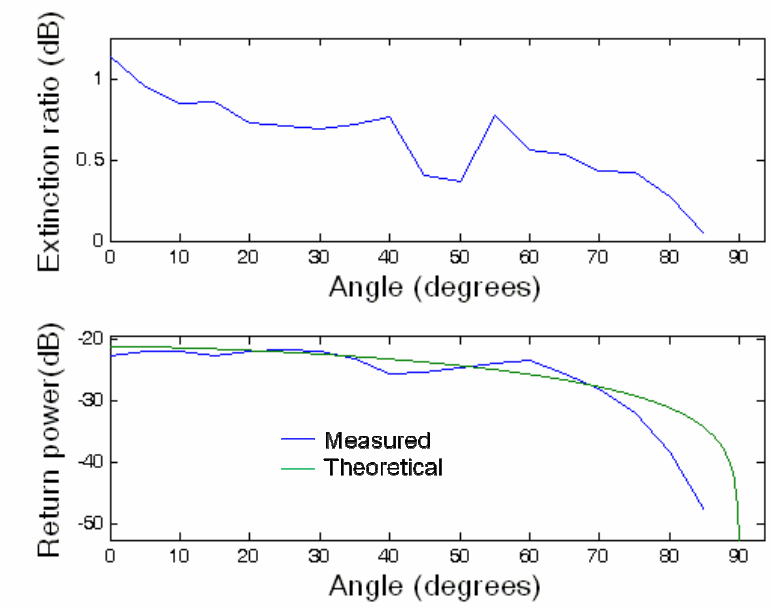

Figure 3.27: Angular dependency of the silicon retro-modulator.

3.7 Conclusion

Retro-modulation involving solid corner-cube retro-reflectors have involved modulating the light outside the entrance of the retro-reflector since it is difficult to manipulate it once it is in a solid material. In this chapter, I presented an alternative method for modulating light in a solid corner-cube retro-reflector by using FTIR to extract the light. I presented calculations showing that FTIR can be achieved in a

silicon corner-cube by bringing a silicon wafer within less than 100 nm of proximity. With bulk optics, I was able to demonstrate FTIR on a CCR; however, the modulation suffered from non-uniformity due to difficulties with aligning the pieces collinearly to maintain the proximity over a significant area. Our trials showed that FTIR became observed after contact and pressure was applied between at the FTIR interface. This resulted in an attempt to create a retro-modulator which applied pressure by using a voltage actuated piezoelectric stack. Here, I was able to demonstrate 3 dB modulation at 1 kHz. We also used a glass retro-reflector which demonstrated 8 dB modulation. At higher speeds, the contrast ratio began to drop off, falling below 1 dB at 10 kHz for both types of modulators.

Chapter 4

Beamsteering

4.1 Introduction

An inherent complexity in establishing a FSO communication link is that the optical beam must be aimed to its targeted receiver. This is routinely accomplished between stationary nodes [4] where large angle, active alignment is not required.

FSO alignment becomes more complex when the points of communication (either or both) become mobile, as this requires real-time alignment. In order to maintain the communication link, the laser beam must be constantly pointed at the receiver, thereby requiring fast beamsteering speeds for a large angular range. In addition to the relative motion of the receiver, atmospheric effects such as scintillation may also misdirect the beam, thereby calling for beamsteering speeds much faster than the pointing errors caused by scintillation (on order of a few milliseconds[49]).

In our work, we accomplish phased array beamsteering with passive phased arrays. Passive phased arrays can be diffraction gratings, arrayed waveguide gratings (AWG) or virtually imaged phased arrays (VIPA). More conventional 'beamsteering' optics controls the properties of the steering device to deflect an entire wavefront (or image). Instead, orthogonal diffraction uses fixed-response optics and directs a single beam of monochromatic light by changing the wavelength of the beam. This effectively decouples the speed dependence from the other parameters by utilizing

wavelength flexibility as another degree of freedom; one that can have a negligible effect on the FSO link.

4.2 2-D Wavelength beam-scanning concept

A diffraction grating has the ability to disperse light in one dimension. When a single wavelength is transmitted through a grating, it is diffracting according to the grating equation, Eq. (1), where P is the grating period, m the diffraction order, λ the wavelength, and θ_m and θ_i the transmitted and incident angles respectively.

$$P(\sin\theta_m - \sin\theta_i) = m\lambda \tag{4.1}$$

This equation shows that the deflection by the grating changes as the wavelength is changed. Thus, when a laser is tuned across a wavelength range, the beam scans along a line [50]. This alone is insufficient for FSO pointing and tracking since objects exist in a 2-dimensional field of view. To reach the second dimension, we can include another diffraction grating that is oriented orthogonally to the first. This arrangement is shown in Figure 4.1.

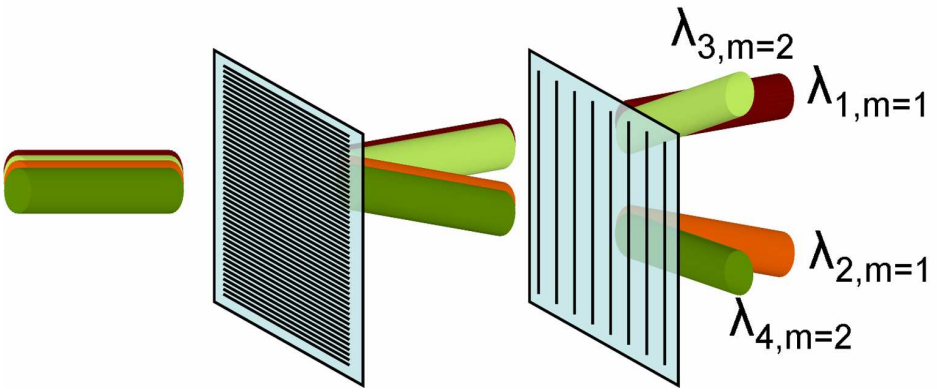

Figure 4.1: 2 diffraction gratings oriented to achieve beamscanning in 2-dimensions. The difference in diffraction orders between the two diffractive structures allows for raster scanning as the wavelength is increased.

There are three characteristics which these gratings must have in order to function as a viable beam scanner that raster scans an entire 2-dimensional range. Firstly, both gratings should be fabricated such that most of the power is diffracted into one diffraction order. For example, in the case of a diffraction grating, a blaze angle would be required to restrict the power within an angular range that contains only one order. Second, the free spectral range of the lower order grating should be greater than the total wavelength scanning range. Thirdly, the total wavelength range should be greater than N times the free spectral range of the higher order grating, where N is the number of lines that are scanned across in the raster scan. When the second and third conditions are combined, a scan through the wavelength range will make one pass across the angular range of one grating while also making N passes through the range of the other. Since the gratings are oriented orthogonally, this creates a raster scan through a 2-D range of angles.

4.2.1 An AWG and a free space optical grating

One such arrangement that can meet the above criteria is an AWG followed by a free-space optical grating. The AWG has high dispersion because it operates in a high diffraction order. The diffraction order is determined by the increment in length, ΔL, between adjacent waveguides in the array, as defined by Eq. 4.2. Here, n_{awg} is the index of refraction of the waveguides and λ_m is the central output wavelength within the m^{th} diffraction order.

$$m = \frac{n_{awg}\Delta L}{\lambda_m} \tag{4.2}$$

The wavelength separation between diffraction orders is known as the free-spectral range (FSR). Eq. 4.3 gives the FSR which is directly related to the final angular separation created by the diffraction grating.

$$FSR = \lambda_m - \lambda_{m+1} = \frac{\lambda_m}{m+1} \tag{4.3}$$

To determine all of the achievable directions, we must first know the exact wavelengths that are transmitted through our system. When we assume no wavelength dependant losses from reflections and transmission through optical materials, the transmitted wavelengths from our system are entirely determined by the diffractive properties of the AWG. To explore this, we start with the grating equation, and modify it to account for optical path delays in the AWG. This yields Eq. 4.4 which now includes the index of the waveguides, n_{awg}, and the phase shift induced by the incremental length, ΔL, of successive waveguides.

$$n_{awg} P_{awg} \left(\sin\theta_m - \sin\theta_i\right) + n_{awg} \Delta L = m\lambda_m \tag{4.4}$$

In the AWG, the diffracted light out of the waveguide array is coupled into another array of output waveguides. Each of these waveguide channels collect the light at a certain angle, θ_N, coming out of the waveguide array. The wavelength at channel N and order m is found by isolating λ_m in Eq. 4.4 to arrive at Eq. 4.5.

$$\lambda_m = \frac{n_{awg}}{m}\left(\Delta L - P_{awg}\sin\theta_i\right) + \frac{n_{awg} P_{awg}}{m}\sin\theta_m \tag{4.5}$$

Here, we make the assumption that the output waveguides are arranged with an angular period θ_o, and that the output waveguides are centered such that θ_m is zero at the middle of the output array. When these are assumed, the first term on the right hand side of Eq. 4.5 is equal to the wavelength hitting the middle of the array, λ_c. These are found using Eq. 4.3. With these considerations, we now arrive at Eq. 4.6 where N is the output channel number and N_{max} is the total number of channels.

$$\lambda_{N,m} = \lambda_c + \frac{n_{awg} P_{awg}}{m}\sin\left[\theta_o\left(N - \frac{N_{\max}+1}{2}\right)\right] \tag{4.6}$$

Eq. 4.6 can be rewritten as Eq. 4.7 to explicitly yield N.

$$N = \frac{\sin^{-1}\left[\dfrac{m\left(\lambda_{N,m} - \lambda_c\right)}{n_{awg} P_{awg}}\right]}{\theta_o} + \frac{N_{\max}+1}{2} \tag{4.7}$$

Ideally the AWG waveguide would be directly integrated with the second stage, avoiding intermediate fiber coupling losses. In our system, however, we connected a fully-packaged AWG to a linear v-groove array to spatially separate the

wavelengths within each diffraction order. The output array of spots yielded by the v-groove array (pitch P_v) is re-imaged by the free-space grating demultiplexer before it is directed by the output lens (with f_o focal length). The output angle is given by Eq. 4.8.

$$\tan\theta_1 = \frac{P_V\left(N - \frac{N_{\max}+1}{2}\right)}{f_o} \tag{4.8}$$

The output angle in the orthogonal direction is created by the dispersion of the diffraction orders by the free-space grating demultiplexer. This demultiplexer might contain a 4-f imaging system with a reflection grating of period P_g, tilted by θ_g, at the Fourier plane and uses identical Fourier lenses with focal length f. The resulting output angle deflection caused by the diffraction grating is given by Eq. 4.9.

$$\tan\theta_2 = \frac{f}{f_o}\tan\left[\sin^{-1}\left(\frac{m\lambda}{P_g} + \sin\theta_g\right) + \theta_g\right] \tag{4.9}$$

4.3 2D wavelength demultiplexer

A natural application of this wavelength dispersive concept is in the area of 2D wavelength demultiplexing. A 2D wavelength demultiplexer is created by simply excluding the final output lens described in the previous section. This system is illustrated in Figure 4.2. Because of its potential application, this intermediate step towards a 2D beamscanner is worth exploring in further detail.

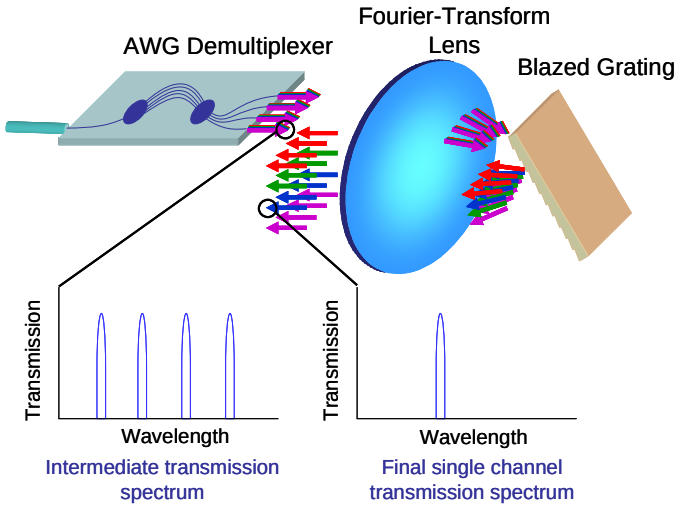

Figure 4.2: Hybrid waveguide – free-space grating multiplexer producing a two-dimensional array output.

This hybrid multiplexer was proposed by Ford and Dragoni in 2001 [51]. In 2004, Xiao and Weiner successfully demonstrated a related array multiplexer using a virtual imaged phased array (VIPA) multiplexer operated with multiple diffraction orders, followed by a free space grating demultiplexer to create the 2-D array output [52]. This system produced 41 demultiplexed channels (4 rows of 10 channels) with about 1.75GHz spectral bandwidth per channel and a minimum 17 dB insertion loss.

In our work on wavelength demultiplexers, we first showed a proof of principle demonstration of the demultiplexing concept (see Appendix A) which produced 72 demultiplexed channels, and then created an demultiplexer intended for ultra-large data capacity (see Appendix B). The ultra-large data capacity demultiplexer carries over 1000 individual channels at approximately 50 GHz pitch and spread over a 600 nm wavelength spectrum, for an aggregate potential data capacity of over 40 Tb/s. Due to its free-space arrayed output, this optical system is

primarily intended to be integrated with optoelectronic or micromechanical devices to construct wavelength switches and dynamic spectral equalizers for ultra-large data capacity networks.

4.3.1 Demultiplexer setup

Figure 4.3 shows a photograph of the experimental system. The first stage of our system consisted of a conventional 1x40 AWG demultiplexer with 50 GHz output channel pitch. The 40^{th} channel of the AWG had anomalously high loss and therefore, only 39 outputs were used. At 1560 nm, the AWG showed less than 5 dB insertion loss and a 27.2 nm free spectral range (FSR). The relation between FSR, wavelength and diffraction order m is given by Eq. 4.3.

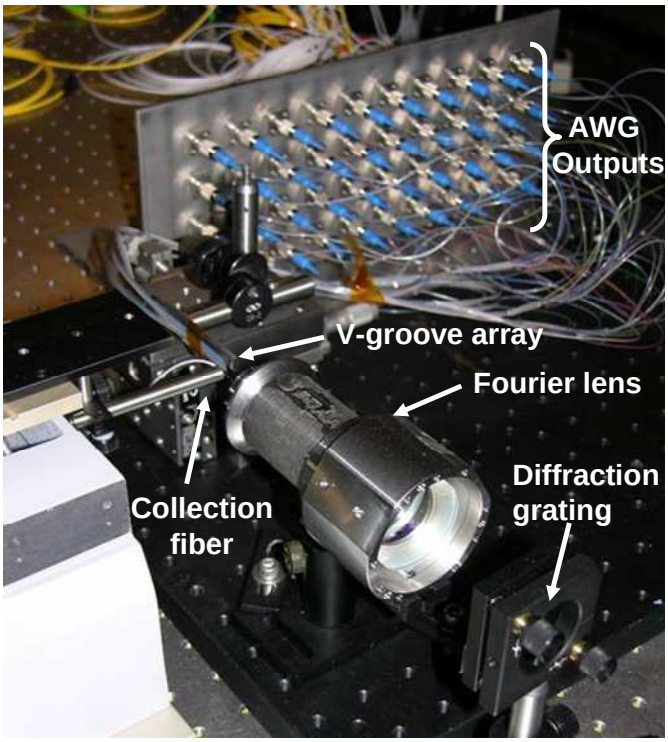

Figure 4.3: Experimental setup, showing the V-groove array that carries the 40 outputs from the first stage multiplexer, and the free space grating multiplexer that produces a 2-D output array which is tested using an single individually-aligned output fiber for channel characterization

We find that the channels near 1560 nm lie in the 53rd diffraction order. The AWG is designed for this order and is typically not used outside of this range. However, other diffraction orders are produced with equally high transmission efficiency when the AWG is illuminated outside of this range.

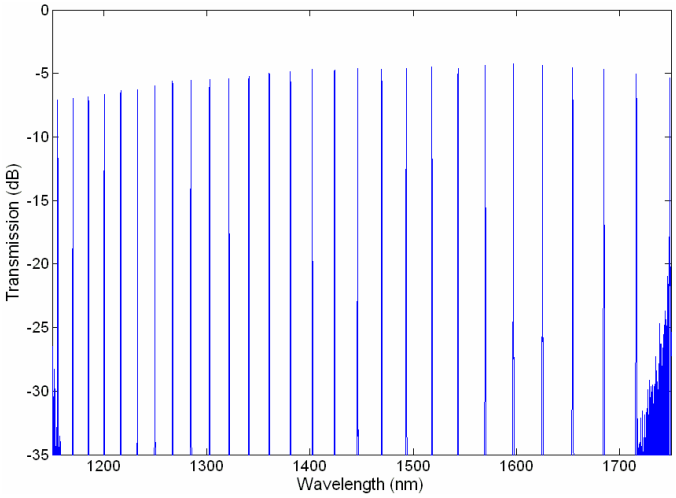

Figure 4.4: Transmission spectra carried by a single AWG output fiber when illuminated with a 600 nm bandwidth, showing 28 diffraction orders separated by the approximate 25 nm FSR. This is the first stage (partially demultipled) output of our demultiplexer.

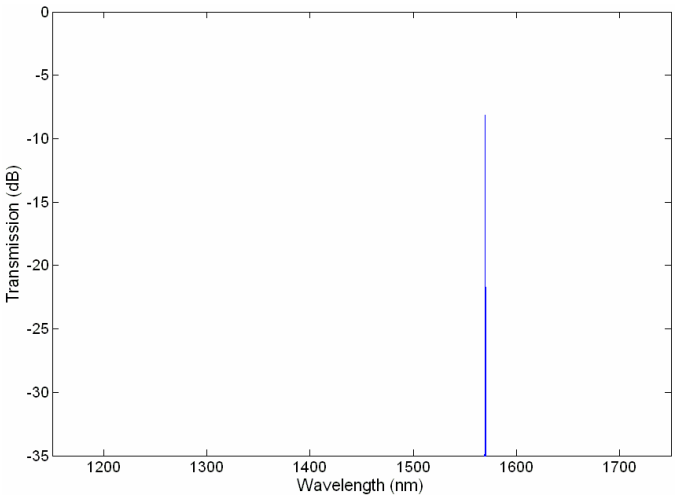

Figure 4.5: Transmission spectra coupled to a fiber positioned at the image plane of the second stage FSG demultiplexer, showing a single AWG diffraction order in the final output.

For our system, we illuminated the AWG with a high-brightness supercontinuum source with spectral output ranging from 1150 nm to well over 1800 nm. With this source, the AWG operation bandwidth was limited only by the spectral

range of our optical spectrum analyzers, from 1100 nm to 1800 nm. With a 600 nm input bandwidth, the AWG produces a spectral comb of at least 28 diffraction orders in each output channel, as shown in Figure 4.4.

All outputs of the AWG must be integrated with the second stage (FSG) multiplexer to create the fully demultiplexed output. Ideally the AWG waveguide would be directly integrated with the second stage, as shown in Figure 4.2, avoiding intermediate fiber coupling losses. In our system, however, we connected a fully-packaged AWG to a 1x40 linear v-groove array with polished fibers at a 127 μm pitch.

The second stage demultiplexer consists of a 5 cm focal length Fourier transform lens followed by a 75 lp/mm blazed reflection grating. The grating is coated with aluminum for adequate reflectivity of a broad spectrum of visible to near infrared wavelengths. The grating is oriented near Littrow angle, so that the first-order diffracted output is backreflected and returns through the Fourier lens and is refocused, creating an image of the v-groove array adjacent to itself. Since the grating is a diffractive element, the horizontal position of the image is determined by its wavelength. Since each diffraction order lies at a different wavelength range, we generate multiple images which are horizontally displaced from each other. Moreover, the image of the array appears slanted due to wavelength variations among the channels within a diffraction order. We tilt the v-groove array in the opposite direction to align the spots in a vertical column. With broadband input into our system, this ultimately produces a rectangular array of spots raster positioned according to their wavelength. These spots each represent the output position of a

demultiplexed wavelength channel. The signal coupled to an optical fiber positioned at one of these output spots is shown in Figure 4.5, showing suppression of all but one diffracted orders visible in Figure 4.4. This is the fully demultiplexed (single channel) output of the hybrid demultiplexer.

4.3.2 Arrayed demultiplexer output

We photographed the entire spot array using an infrared camera, a Sensors Unlimited 320M camera with a 320x240 array of InGaAs detector pixels at a 25 micron pitch. The output array is located adjacent to the fiber V-groove array, so to obtain this photograph we temporarily inserted a gold mirror to reflect the light out of the demultiplexer and into an imaging system consisting of two identical Fourier transform lenses in a unit-magnification 4f configuration. The image of the spot array is shown in Figure 4.6. Each column of the array represents a single AWG diffraction order, or in other words, a single image of the intermediate v-groove array. These spots are raster positioned according to wavelength from top to bottom, and then from left to right. The nonuniformity of the array is a result of several factors, including the relatively course sampling grid of the detector pixels, the nonuniformity of the supercontinuum source (which varied by 15 dB over the 600 nm operating range), and wavelength dependent losses. An accurate measure of the insertion loss for each wavelength channel is shown in Appendix B.

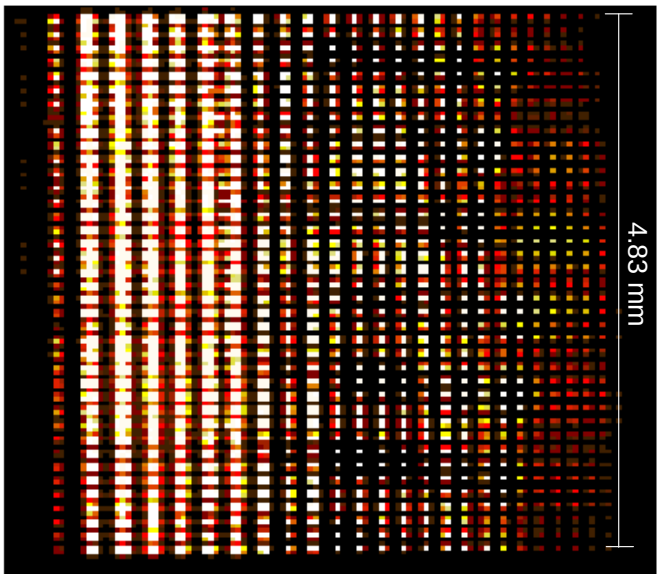

Figure 4.6: Photograph of the entire output array taken by relay imaging the output into an InGaAs sensor array, showing the 39 columns (first stage AWG fiber inputs) of 28 diffraction orders each (dispersed by the FSG). The 320x240 InGaAs camera does not fully resolve the 1090 spots.

A standard SMF-28 single mode fiber mounted in a silicon V-groove and polished flat was used to characterize the each of the 1092 individual channel outputs. The fiber was mounted on a PI model F206 hexapod stage (visible at left in Figure 4.3) to provide <0.1 micron absolute positioning accuracy. This fiber was scanned across the plane of best overall focus. The fiber coupled signal was connected to external components for intensity measurements, spectral analysis, polarization dependence loss measurements and bit error rate tests.

Figure 4.7 diagrams the calculated output spot distribution. The rows are separated by 0.127 mm, equal to the pitch of the 1x40 v-groove array. The separation between the columns is set by dispersion from diffraction from the free space grating,

and so is proportional to the FSR (Eq. 4.3) and increases monotonically with wavelength. In the equations shown, m_n is the AWG diffraction order at wavelength λ_n, and f is the lens focal length and d is the grating period of the free space demultiplexer.

The output spot wavelengths are distributed in a raster fashion. The shortest wavelength signal is in the lower right, increasing in 50 GHz steps as you move up the column. There is a longer interval before you reach the next diffraction order, which starts at the next column to the left. The longest wavelength output is in the upper left corner. The design of the AWG (delay arm length distribution and output waveguide arrangement) determines the space between diffraction orders.

Figure 4.8 shows crosses at the measured position of maximum coupling efficiency for each channel into the fiber. These are plotted against their predicted positions, represented by circles, calculated based on their diffraction order in the AWG and the grating equation, and measured focal length of the Fourier transform lens. The absolute position of the predicted and experimental data are aligned to minimize the RMS difference, which was 6.5 μm. In our measured data set, the column pitch decreases by more than half, from 0.268 mm near 1800 nm (at left) to 0.114 mm near 1160 nm (at right).

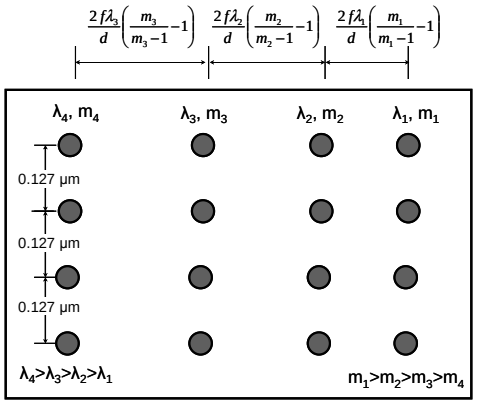

Figure 4.7: Expected arrangement of the output spots. The vertical separation of the rows is constant, assuming negligible imaging system distortion, but the space between columns is a function of the diffraction order.

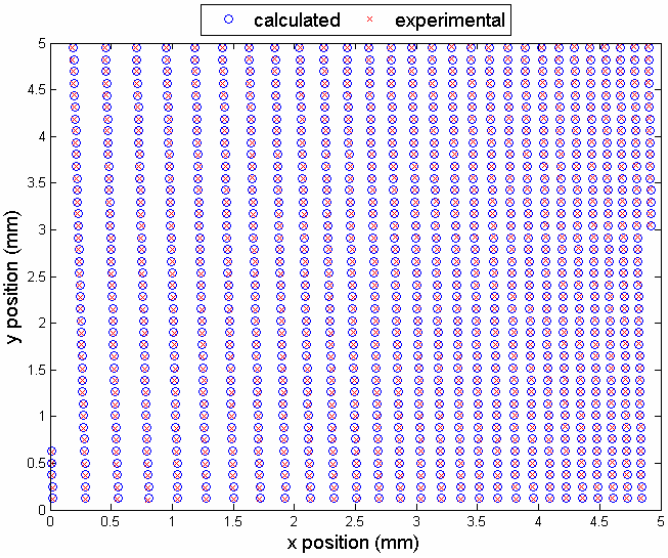

Figure 4.8: Mapping of both theoretical and experimental spot locations in the output plane.

4.4 Experimental setup

For our experimental demonstration of beamscanning, we used the system illustrated in Figure 4.9 and Figure 4.10. We used a JDSU 1x8 channel arrayed waveguide grating as the first diffractive element which operated in the 194th diffraction order at 1550 nm. Since the AWG gives discrete outputs at specific wavelengths, the achievable scanning angles exist in a nearly rectangular array rather than a set of lines. The AWG channels were transferred into free space through a 635 μm pitch v-groove array. This led into a free space optical grating demultiplexer, taken from a Network Photonics WDM switch, consisting of a 100 mm focal length Fourier lens followed by a 3rd order, 300 lp/mm reflection grating (Newport catalog code 53-*-013R). Like the demultiplexer shown previously, the output from the two demultiplexers is a grid of single mode Gaussian spots where each one corresponds to a different wavelength. This is converted into a beam scanner with the addition of a gold mirror (to divert the light away from the components) and a Nachet Vision 8x, 25 mm focal length microscope objective to collimate and direct the beam.

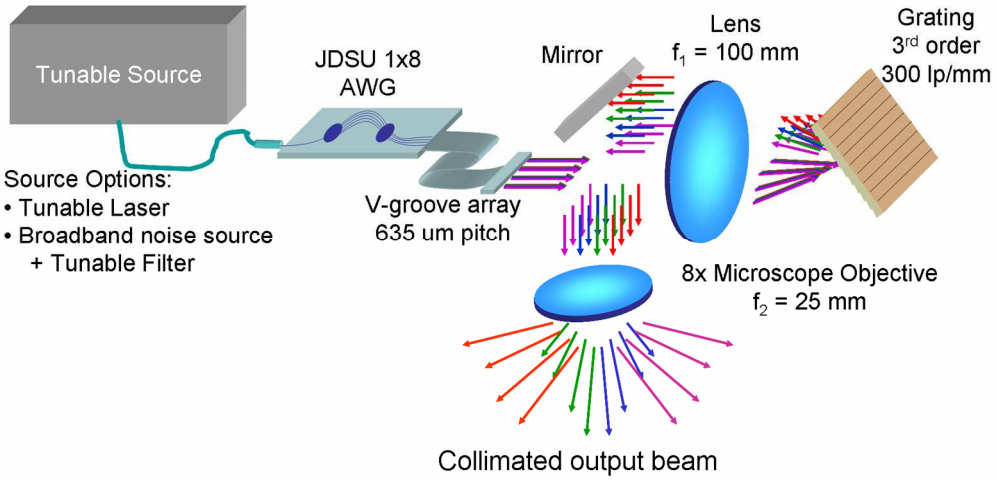

Figure 4.9: System and components used to demonstrate beamscanning. The demultiplexed channels from the AWG are ejected into free space by a V-groove array which sits at the focal plane of a Fourier lens. This lens is part of a free space grating demultiplexer which separates the multiple orders from the AWG. The output is focused at the focal plane of a microscope objective which collimates and directs the light.

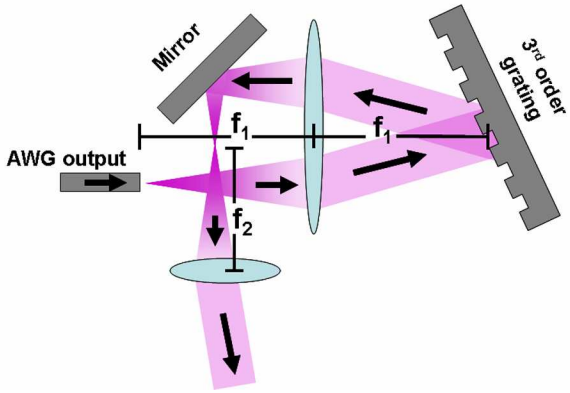

Figure 4.10: 2-dimensional illustration of a monochromatic beam propagating through the system.

The AWG and free-space optical grating were both designed for the C-band (1530 – 1562 nm) of the telecommunication spectrum. These wavelengths are also

popular for free-space optical communications; thus, our demonstrations are appropriately carried out using wavelengths near 1550 nm.

Figure 4.11 shows the predicted output angles of the directed beam for wavelengths from 1546 to 1590 nm using the equations shown previously and the parameters illustrated in Fig. 2. Here, we used a waveguide index, $n_{awg,}$ of 1.5 and a ΔL of 199 μm to have the AWG operate in the 194th diffraction order at 1550 nm. We also assumed that there is no apodization from any apertures which might have limited the field. The figure shows 6 columns and 8 rows of achievable directions. Each row corresponds to a single channel from the AWG, and the horizontal separation between the rows is created by dispersion from the diffraction grating. The 6 columns are a result of fitting 5 FSRs (~ 8nm for the AWG) in the total wavelength range.

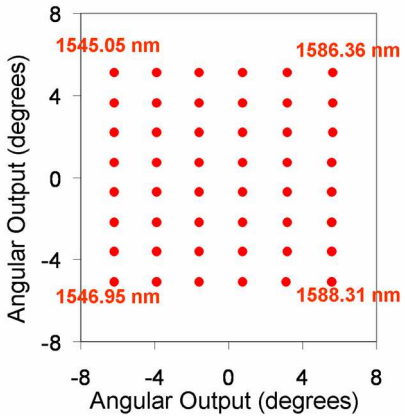

Figure 4.11: Calculated output angles from the beam scanner.

Ideally, the range of a beam scanner should be continuous instead of a discrete array of spots. This functionality can be incorporated into our beam scanner with the addition of a continuous beam scanner to cover the range in between the spots. The requirements of this beam scanner are achievable with existing technology (such as an electro-optic scanner) since the required scanning range is now limited to the distance between our discrete directions.

4.5 Experimental results

Figure 4.12 shows a photograph of the actual setup where the output beam is projected onto a white screen 20 inches distant. We used a Sensors Unlimited 320M camera with visibility in the NIR wavelength range to image the projected beams. This photograph also shows an Agilent tunable laser as the optical source. In our experiments, we used a number of different optical sources to characterize different properties of the beam scanner. For fast beamscanning, the ideal source would be a fast, wavelength tunable laser. To the author's knowledge, the fastest tunable lasers are grating-assisted codirectional coupler with rear sampled reflector (GCSR) lasers which can switch across its entire wavelength range in under 50 ns [53]. The wavelengths from these lasers are limited to a discrete set of wavelengths; however, this does not harm our system's scanning ability.

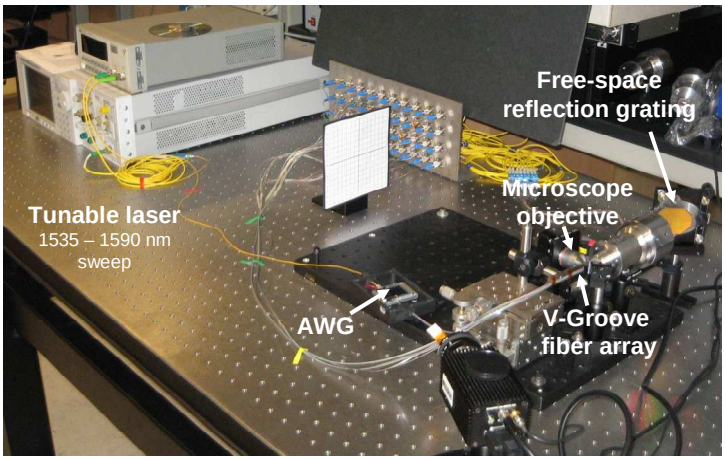

Figure 4.12: Photograph of the beam scanner with a tunable laser acting as the optical source.

We used a C- and L-band ASE source to simultaneously transmit power into the entire output array of beams. Figure 6 shows the captured image of all of these beams projected onto the screen.

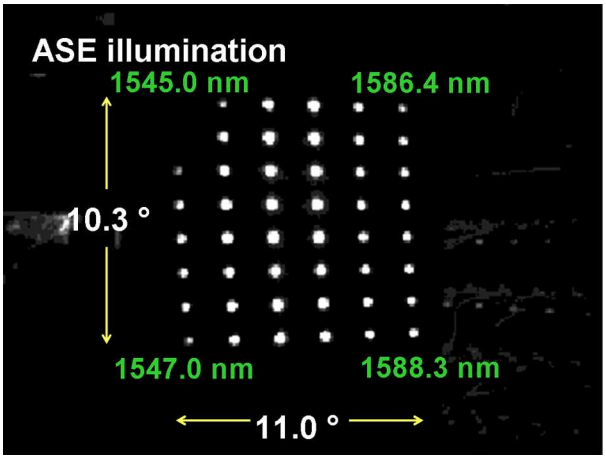

Figure 4.13: An ASE optical source is used to send power towards every achievable direction of the beam scanner. The camera is saturated to show all spots.

Figure 4.13 shows that the achievable range from our beam scanner was 10.3° and 11.0° and exists as discrete directions in an 8 by 6 array. This is consistent with the predictions shown previously. The apparent power variation over the different directions is primarily due to the spectral profile of the ASE source. Our work on creating a wavelength demultiplexer suggests that the insertion losses are uniform across the wavelength tuning range with approximately 8 dB loss.

For the next part of our experiments, we used an Agilent 81642A tunable laser to send power to a single direction. The output beam of a single wavelength is shown in Figure 4.14a. While this laser's slow tuning speed (2.8 seconds to scan through 100 nm) makes it infeasible for FSO beamscanning, the Agilent tunable laser was still useful in observing the output beam quality of the beam scanner. The beam profile is a result of a re-imaged fiber output (from the v-groove array) directed and collimated by the microscope objective. Figure 4.14b shows an image of the single spot. This was captured using a bare InGaAs sensor placed immediately after the output of the beam scanner. We measured a 6 mm $1/e^2$ beam diameter which matches the expectations of a bare fiber output being collimated by the microscope objective. We note that this beam waist can be changed by selecting a different collimating lens.

Figure 4.14b also shows that the beam maintains a primarily Gaussian form which is indicative of low distortion through the system and yielding a smooth wavefront.

Our work with the 2D demultiplexer also showed that in these 2D dispersive systems, the crosstalk inherent in the AWG and the linewidth of the optical source

determines the amount of crosstalk between neighboring wavelength channels. The prior results also show that there is virtually no (> 30 dB) crosstalk between channels which are separated by one FSR. Using the devices in our setup as an example, the Agilent laser linewidth is 100 kHz which is negligible compared to the 100 GHz AWG channel pitch. This means that the crosstalk is determined by the crosstalk between AWG channels which we measured as greater than 35 dB. Figure 4.14a also shows no apparent leakage of the optical power into neighboring channels.

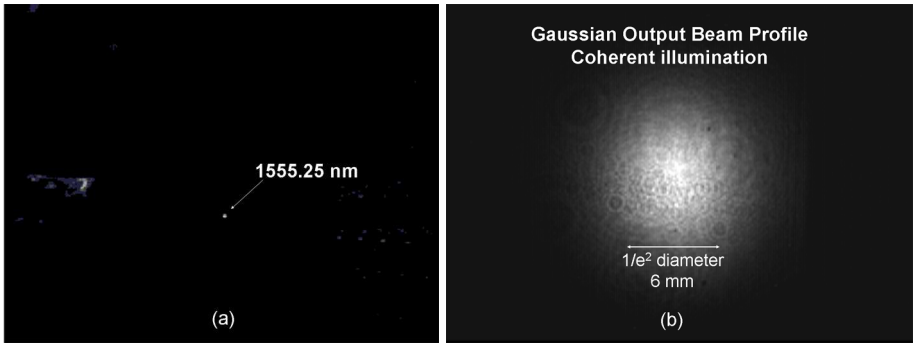

Figure 4.14: a) The output of a single wavelength and b) its profile immediately exiting the beamscanner.

Since this system is intended for use in FSO communications, the transmitted beam may carry a modulated signal and would inherit a finite bandwidth. Since our system is dispersive, a significant bandwidth would stretch the output beam over a linear range of directions. The amount of stretching would depend on the degree of dispersion of the free space optical grating. Crosstalk may also cause a limitation when the signal is modulated with a bandwidth greater than those of the AWG channels.

An alternative to using a tunable laser as the source is to use an ASE source passed through a tunable filter. We demonstrated this option using the same ASE source used above along with a CoreTek MEMS tunable etalon filter. Two separate detectors were placed at different points in the field of view. These points corresponded to 1546.7 nm and 1578.3 nm wavelengths. Figure 8 shows the transient response of the power at the simultaneously measured positions when the filter was switched between these two wavelengths. This shows a 183 μs switching time (time for the signal to go from 10% to 90% of its steady value) which is purely determined by the switching speed of the tunable filter. The CoreTek MEMS filter used here had a passband of 0.47 nm which is larger than the channel pitch of our AWG. Thus, this filter produced approximately 5 dB of crosstalk in adjacent channels and would not be suitable as a secure FSO beamscanner.

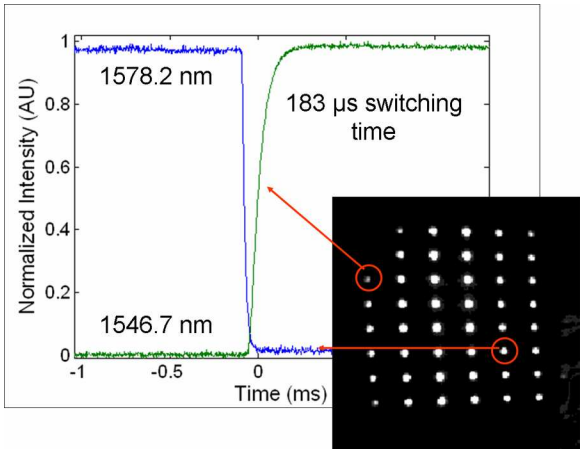

Figure 4.15: Transient response when switching between two directions.

4.6 Beam scanner with VIPA

An alternative implementation of this beam scanner is one that uses a VIPA in place of the AWG. The VIPA, invented by M. Shirasaki [54][55], is a glass slab that acts much like a highly dispersive diffraction grating. The VIPA operates on the principle of virtual images interfering with one another, as illustrated in Figure 4.16. These virtual images are of a line source which is created by focusing a collimated beam with a cylindrical lens. This line source is focused at the entrance aperture of the glass slab which is tilted at a small angle. The back surface of the slab is nearly 100% reflective with the exception of the entrance aperture, while the front slab has a graded reflectivity to allow output light. In this arrangement, the light will undergo multiple reflections and create a series of staggered virtual line sources. The light leaks out of the front surface into free-space where the cylindrical waves created by the virtual line sources interfere with each other. The graded reflectivity equalizes the leaked power of successive reflections. Ultimately, this resembles a diffraction grating operating with a large tilt and very high order.

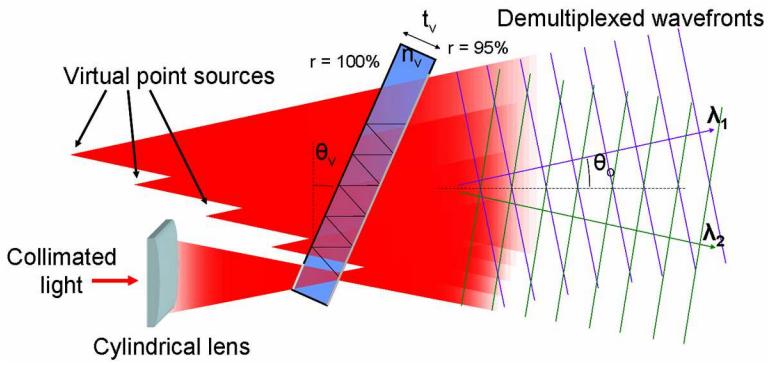

Figure 4.16: A VIPA with the virtual line sources illustrated.

One beneficial advantage of the VIPA over the AWG is that the VIPA can easily operate in a much higher diffraction order. This allows for more raster lines over a chosen wavelength range. This is described by the grating equation for the VIPA, Eq. 4.10, where m_v is the diffraction order, t_v is the thickness of the VIPA, n_v is its index of refraction, θ_v is the tilt angle of the VIPA and θ_o is the output angle.

$$\frac{m_v \lambda}{2 t_v n_v} = \sin\left(\frac{\pi}{2} + \theta_o - \theta_v\right) \tag{4.10}$$

The output angle, θ_o is shown explicitly in Eq. 4.11.

$$\theta_o = \theta_v - \frac{\pi}{2} + \sin^{-1}\left(\frac{m_v \lambda}{2 t_v n_v}\right) \tag{4.11}$$

The f-number of the cylindrical lens determines the field of view of the virtual line sources. This subsequently restricts the range of possible output angles, θ_o and will therefore keep the optical power in diffraction orders that fall within this angular range. In a beamscanner, especially one used for secure free-space optical communications, only one diffraction order should exist within the field of view for each wavelength. To ensure this, the optical path length of the VIPA, $t_v n_v$, inherits a maximum limit. When this optical path length is small, the value of the last factor in Eq. 4.11 is significantly different at adjacent diffraction orders. This difference should be large enough such that the adjacent diffraction orders fall outside the possible range of θ_o and only one diffraction order exists for each wavelength. This requirement is shown in Eq. 4.12 where $f_{\#}$ is the f-number of the cylindrical lens.

$$\tan^{-1}\left(\frac{2}{f_{\#}}\right) < \sin^{-1}\left(\frac{m_v\lambda}{2t_v n_v}\right) - \sin^{-1}\left(\frac{(m_v - 1)\lambda}{2t_v n_v}\right) \tag{4.12}$$

The VIPA is made into a 2D beamscanner by layering a diffraction grating on the VIPA's output surface. This is depicted in Figure 4.17 where every wavelength, represented by different colors, is shown projecting out of the beamscanner. Also, a planar waveguide creates the line source entering the VIPA instead of a cylindrical lens. This creates a more seamless and compact integration of fiber optic input into the VIPA. The angular range of the cylindrical wave is now determined by diffraction from a slit. In other words, the angular range of the beamsteerer is inversely proportional to the width of the slit and independent of the total aperture. To increase the aperture size, the length of the line source can be mechanically increased and the transmissivity through exit surface of the VIPA can be decreased to create more internal reflections and distribute the power over a longer distance. Unlike the fiber coupled AWG, the VIPA gives a spatially continuous, free-space output meaning that the beamscanner can scan continuously along one of the directions.

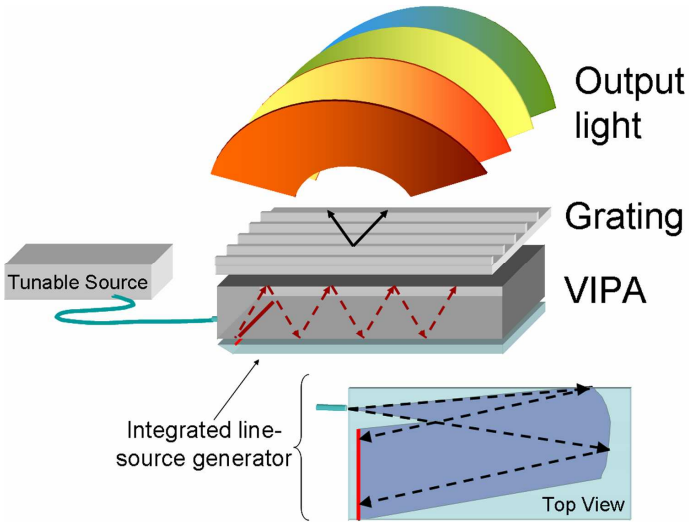

Figure 4.17: Beam scanner consisting of a VIPA and a free-space optical grating demultiplexer.

Eq. 4.10 can be used to find the wavelength range of each diffraction order in the VIPA's field of view as well as the output angle of each wavelength in one direction. The grating determines the output angle in the orthogonal direction which is predicted by Eq. 4.1.

We envisioned a VIPA beamscanning system with the following parameters to demonstrate its potential performance. The cylindrical wave feeding into the VIPA has a numerical aperture of 0.05 and the diffraction grating has a 500 lp/mm pitch operating in the 1st order. VIPAs typically have a 1.5 index, 1 mm thickness. Figure 4.18a shows the output if we use a typical VIPA tilted at 2.5° where the spots at 1553 nm are circled. This figure reveals that multiple diffraction orders are created. As mentioned earlier, this is because the optical path, $t_v n_v$ of the VIPA is too large.

In order to create a viable beamscanning system which transmits only one beam, the VIPA would have 1.5 index of refraction and 0.1 mm thickness. The thinness of the VIPA is atypical and may pose additional problems such as coupling the light into the slab, sturdiness or uniformity of the VIPA. For the purposes of this investigation, we assumed that such a device could exist and operate with the same properties of a typical VIPA. The same section of the output is shown in Figure 4.18b with the thinner VIPA.

Figure 4.19 shows the entire calculated output field where the optical wavelength range used is 1400 – 1600 nm. With these parameters, Figure 4.19 shows approximately 5° x 9° total output range existing over 26 columns of output angles.

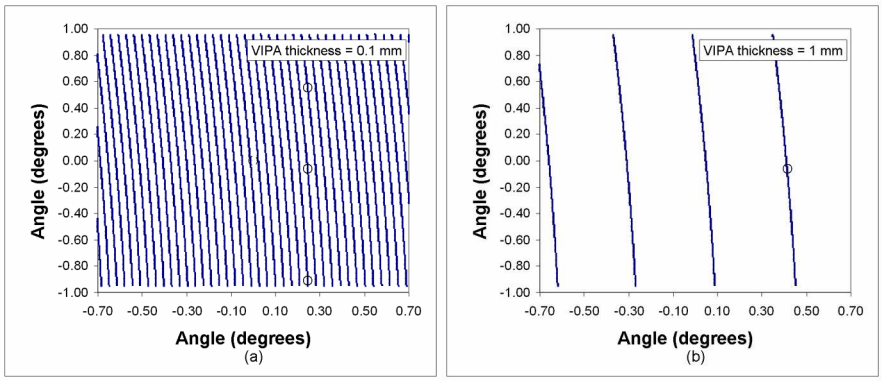

Figure 4.18: A section of the output of a 2D demultiplexer which uses a) a 1 mm thick VIPA and b) a 0.1 mm thick VIPA. Spots created at 1553 nm are circled and show degeneracy through multiple diffraction orders when the VIPA is too thick. For secure FSO communications, only one diffraction order should exist.

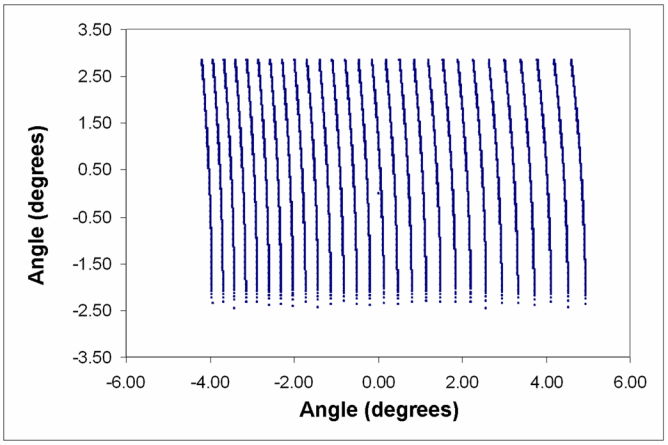

Figure 4.19: Calculated output directions (in degrees) using a VIPA in the beam scanner.

4.7 Conclusion and discussion

I presented a beamscanning method where the input wavelength is directly related to the output direction in a 2-dimensional field of view. This is accomplished by combining two wavelength dispersive devices orthogonally and in series. With the proper devices, the beam raster scans through the 2-dimensional field as the wavelength from an optical source is increased.

An intermediate step in this work was the creation of a 2D hybrid wavelength demultiplexer by combining an AWG with a free-space optical grating demultiplexer. With the goal of a large channel count, we designed a demultiplexer which created a near-rectangular array of 1092 distinct wavelength channels which were focused onto a plane in free space. The measured output grid was consistent with our calculations of channel positions.

I have experimentally demonstrated beamscanning by adding a 25 mm focal length microscope objecting to collimate and direct the free-space array of points from

a customized version of the wavelength demultiplexer. Using this combination of parts, we obtained 2-dimensional beamscanning on an 8x6 grid of discrete directions. This output yielded a total angular range of 10.3° by 11.0°. These results were consistent with calculations based on diffractive theory and geometric optics. We achieved 183 μs scanning times using an ASE source followed by a CoreTek tunable filter which switched the power from 1546.7 nm to 1578.2 nm.

We also discussed an improved version of the beam scanner which uses a VIPA combined with a free-space optical grating demultiplexer. Because the VIPA has a continuous output, one dimension in the output field of view can be scanned continuously. In the other dimension, the high dispersion of the VIPA allows us to point to a greater number of discrete directions which are spaced closer together. This was verified with theoretical calculations on a conceptual system.

The text of Chapter Four, in part or in full, is a reprint of the material as it appears in the following publications:

- T. K. Chan, J. Karp, R. Jiang, N. Alic, S. Radic, C. F. Marki, J. E. Ford, “1092 channel two-dimensional array demultiplexer for ultra-large data bandwidth”, J. Lightwave Tech., 24 (1), March 2007.
- T. K. Chan, E. Myslivets, J. E. Ford, “2-Dimensional beamsteering using dispersive deflectors and wavelength tuning”, Opt. Express, 16 (19), September 2008.

The dissertation author was the primary researcher and author. The co-authors listed in these publications directed and supervised the research which forms the basis for these chapter.

Chapter 5

Conclusion

5.1 Summary

FSO is a maturing technology which has yet to garner the advantages and viability to become attractive for large scale implementation. This has come from the lack of technology and innovation to fulfill the requirements of a large scale, dynamic and economical communication system. This dissertation has presented a number of my contributions in the form of devices which bring new ideas to realize a more practical FSO system. This was based on asynchronous retro-communication; a method ideal for many short range applications including remote sensing, identification, UAV communication and the “last mile” problem.

First, I designed a hollow MEMS corner-cube retro-reflector. This device was utilized an arrayed MEMS deformable mirror which performed the optical modulation. I simulated the optical response of the deformed state of the mirror to show that more than 10 dB attenuation in the reflected beam was possible at achievable deformations. In addition, I showed that this attenuation was maintained for large angle and wavelength ranges. This mirror was fabricated and characterized to verify the predicted performance. The speed and temperature response of this mirror was also characterized. Despite fabrication errors which limited the total deformation of the mirror below the designated amount, the mirror still produced

adequate modulation. This mirror was integrated into a corner-cube with two gold coated mirrors to complete the retro-reflecting modulator. The overall motion of the MEMS components remained well under 1 µm, thereby maintaining 100 kHz speeds. The arrayed aspect of this device garnered the scalability lacking from alternative MEMS devices.

To accommodate a larger angular range, I designed a modulator for a solid silicon corner-cube instead of a hollow one. The modulation was created by disrupting the internal reflections within the cube by creating FTIR when a parasitic wafer was brought close to the reflecting surface. Despite theoretical calculations suggesting that no contact was necessary for modulation, the experiments showed that physical restrictions made modulation only possible once contact was made between the parasitic wafer and the corner cube. Suitable modulation was only created with the application of pressure. A more thorough study is needed to understand why this is necessary. Although I could not produce a non-contact FTIR modulator, I prototyped a solid retro-modulator using a piezo-actuator to control the pressure. Experiments demonstrated that this method of modulation was limited to speeds of a few kilohertz and produced larger extinction when glass was used as the corner-cube retro-reflector. This provides a low cost alternative for applications requiring low data modulation such as friend or foe identification.

Finally, I created a fast beamscanner to accomplish alignment from the interrogator side of the FSO link. This system succeeded work on a 2-dimensional hybrid wavelength demultiplexer which produced an array of raster scanned spots in

free-space. The demultiplexer consisted of an AWG combined with a free-space optical grating which orthogonally separated the diffraction orders from the waveguide array output in space. This demultiplexer concept was modified into a wavelength controlled beamscanner by directing the array of spots into an array of directions. This arrangement separates the scanning control from the optical components, meaning that the optical beam can be modified independent of the scanning speed. This increases the potential scanning speeds to the limits of wavelength scanning speeds (currently reaching switching speeds of under 50 ns). Diffractive analysis was done on this system to accurately predict the achievable beam directions which were possible with different AWG and grating demultiplexer parameters. I also proposed an improved system which used a VIPA instead of an AWG. Its performance was predicted and showed more achievable angles over a lower wavelength range.

5.2 Future Work

When the MEMS deformable mirror retro-modulator was prototyped, a fabrication error with the silicon nitride layer in the MEMS component limited its performance. In the future, proper fabrication of the layer can be carried out to improve upon the possible deformation and observed performance. According to simulations, an increase in deformation would yield over 10 dB extinction for a larger range of angles. Experiments can be done to verify these simulations and ultimately create a more reliable and effective retro-modulator.

Our experimental work creating the FTIR retro-reflector showed that the goal of obtaining modulated FTIR in silicon requires more development. A more viable solution was shown with glass which had a looser requirement for FTIR while sacrificing angular range. While this became a cheap solution for a slow, piezo actuated retro-modulator, there is the opportunity to investigate using glass in a non-contact, MEMS retro-modulator.

The driver circuit which designed by Justin Hallas showed that the power could be provided to our retro-modulators in a compact package; however, this circuit was limited in speed and voltage amplitude. For future work, this circuit can be developed to drive our high capacitance devices to suitable speeds and voltages. This drive should also be designed to read an arbitrary input signal and encode into its drive voltage.

Once the driver circuit is completed, it can be packaged with the packaged retro-modulators into a free-standing, portable device that can function outside the laboratory environment.

The beamscanner was shown as a viable table top system. For practical use, the optics of this device should be integrated into a portable device. This work can be continued to completion by integrating these components together as a freestanding component which can be tested in a real world setting.

By combining a packaged beamscanner and either of the retro-modulators, we can create a dynamic bi-directional FSO link. The addition of a tracking algorithm

would allow us to create an active tracking system where the retro-modulator can become mobile as it is functioning. By overcoming the challenging of implementing these devices in a system, we can provide a true test of our device's abilities as they are used in real world situations.

5.3 New Directions

A common trend seen in modulators is the inverse relationship between modulator size and speed. This applies to the aperture size of retro-modulators since modulation is usually done on a large field. One method of simultaneously creating both size and speed is by dividing the aperture into an array of smaller devices; each element of the array would have the speed advantage of a device of that size. This also limits the lateral dimension of a device, allowing for planar devices for easy integration. In an array, each element contributes as part of the larger aperture; however, there is now a phase mismatch between the elements. In other words, the retro-reflected beam from each element will interfere with each other, likely destructing the retro-reflected beam. To accommodate for this phase mismatch, phase control of each element needs to be introduced. This can be done with an array of phase modulators that are lined up with the array of retro-reflectors. This in and of itself becomes a method of modulation since the presences of phase matching determines if the retro-reflected signal is returned back to the interrogator.

To create the proper phase match, the incident angle of the incoming beam must be known. An angle detector must be introduced at which point our retro-modulator become an active retro-reflector. For a 32x32 array of 1.5 mm pitch retro-

reflectors, the return beam has a divergence of 0.0063°. This divergence is the degree of accuracy required by the angle detector; an accuracy which is not achieved by conventional angle detectors. One idea for an ultra-sensitive angle detector is an array of etalons followed by an array of detectors. The transmission through an etalon is highly wavelength and angle sensitive. However, a transmission value through an etalon is not unique to a specific angle; therefore, a series of etalons which each have a different thickness is needed. The quantization error in the detectors decreases the accuracy of each etalon-detector combination, meaning that more etalons are required. Early analysis suggests that complex optimization algorithms are needed to find the best combination of etalon thicknesses for the least amount of etalons.

In this arrangement, we assume that the incoming wavelength is known. Conversely, if the incoming angles are fixed, this device can be used as an ultra-sensitive wavelength detector.

Preliminary calculations were done using a VIPA as part of a beamscanner. These calculations showed viability in such a device, although they revealed tight tolerances on parameters such as VIPA thickness and uniformity. Nevertheless, the advantages gained from using a VIPA warrant the need for more investigation of this system.

Appendix A:

2-D Array Wavelength Demultiplexing by Hybrid Waveguide and Free-Space Optics

Trevor K. Chan, Maxim Abashin and Joseph E. Ford
University of California San Diego, Electrical and Computer Engineering, La Jolla CA 92073-0407
tkc@ucsd.edu, jeford@ucsd.edu

Abstract: We demonstrate wavelength demultiplexing into a raster-scanned 8x9 array by combining a 1x8 arrayed waveguide grating with a free-space grating multiplexer. 9 diffraction orders from each AWG output are separated onto a 2D array on an InGaAs camera or coupled into a scanned output fiber. This first proof-of-principle device had 0.2 nm channel -20 dB width, >35 dB spectral extinction and 1.5 to 2.5 dB insertion loss over the 70 nm operating range.

OCIS codes: (060.1810) Couplers, switches, and multiplexers; (060.2340) Fiber optics components

1. Introduction

Wavelength demultiplexers for high channel-count (32+) WDM systems are made using arrayed waveguide gratings (AWG) waveguide [1] or blazed diffraction grating [2] free-space optics (FSO). Both approaches convert a multiplexed input spectrum into a linear array of output channels where the separate signals are either coupled into individual output fibers or into devices (e.g., detectors or sources). Very large channel count WDM systems for access networks may require more than 1000 channels, where linear array demultiplexers become unwieldy; 1024 output fibers on the standard 250 micron pitch would create a 256mm long fiber array.

2-D array demultiplexers are capable of handling large channel counts in a reasonable footprint: a 32x32 channel array on a 250 micron pitch would cover an 8x8 mm area. 2-D output fiber arrays are difficult to fabricate, but may not be necessary for many important applications. Surface-normal optical devices include optoelectronics passive filters (detector, modulator, and VCSEL arrays) active components [3] as well as MEMS (spectral equalizers, add/drop switches, and dispersion compensators) [4-6]. Array demultiplexers are ideally suited to such devices, where the physical layout of the individual elements is often limited only by the electrical connections to the package. Here we experimentally demonstrate 2-D array demultiplexing using a free-space optical / arrayed waveguide grating (FSO/AWG) as shown in Figure 1. This system was proposed by Dragone and Ford [7] but not, to our knowledge, previously implemented.

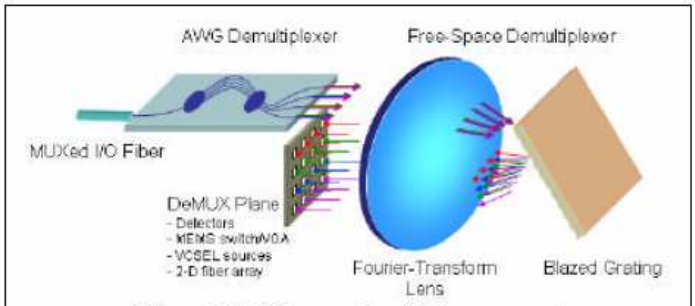

Figure 1: Hybrid array demultiplexer concept

2. Hybrid Arrayed Waveguide Grating / Free-Space Optical Demultiplexer

A conventional AWG is operated with a restricted band of wavelengths such that the output wavelengths are all contained within the free spectral range (FSR) of a single output diffraction order, but each fiber output of an AWG illuminated with a broader spectrum will contain multiple diffraction orders. For an AWG operated near the design wavelength of $?_c$, the FSR is given [8] by FSR = $?_c$ [$(^{M}/_{(M-1)})(^{n_f}/_{n_o} -1)$], where M is the diffraction order, n_f is the waveguide core index and n_o is the waveguide cladding index. For example, JDS Uniphase 1x8 AWG multiplexer model AWG-WB-1x8-50G-1.5-M-LC/SPC used in this experiment has a channel pitch of 50 GHz (0.4 nm), a design wavelength of 1554 nm, a FRS of 8.1 nm, which means that it is operated in approximately 193rd diffraction order. Illuminating this AWG with the 80 nm bandwidth of a C+L-band ASE source produces 9 diffraction orders on each fiber output, as shown in Fig. 2. These diffraction orders can be further separated by cascading a second wavelength demultiplexer. The FSO/AWG arrangement of Figure 1 separates the diffraction orders so that they are effectively raster scanned into a 2-D array, each line separated by the FSR of the AWG. If the AWG is designed with waveguide outputs across the entire FSR, there can be little or no wavelength separation between output rows.

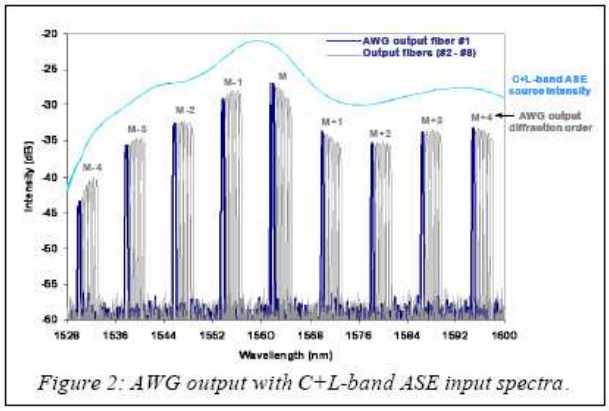

Figure 2: AWG output with C+L-band ASE input spectra.

The $(^{M}/_{(M-1)})$ dependence of the FSR on diffraction order means that even if the FSO deMUX is perfectly linear, the vertical pitch of the output array increments by about 0.5% for each output order. If the output is to be coupled into a 2-D fiber array, the separation between rows must compensate as the shift will add up to more than the 1 micron lateral alignment tolerance. For surface normal devices the shift can be corrected by device layout, though it is typically negligible compared to the individual element apertures.

The physical format of the array MUX output is quite flexible. The horizontal pitch depends on the spacing of the waveguide outputs while the vertical pitch is determined by the FSO deMUX dispersion, which is proportional to the lens focal length times the grating spatial frequency. With reasonable physical parameters, the grid pitch can be varied from 20 microns to over 1 mm, depending on application requirements.

3. Proof-of-Principle Experiment

The experimental system was constructed using the JDS Uniphase AWG described above. This AWG was fiber coupled, and rather than de-package the AWG waveguide the outputs were connected to a separate 1x40 silicon V-groove fiber array with fibers separated by 127 micron pitch. We chose to use every 5th fiber, producing a 0.635 mm pitch between inputs to the FSO system.. The FSO deMUX, which was taken froma Network Photonics wavelength add/drop switch, used a f=100 mm Fourier-transform lens and a 600 line/mm holographic grating, with a ?/2 plate to rotate the output light polarization as described in ref [5]. This combination yields 130 micron/nm spatial dispersion and so converts the 8.1 nm FSR separation between diffraction orders seen in Figure 2 into a 1.05 mm line spacing. A polarizing beam splitter (PBS) was inserted between the AWG inputs and transform lens to separate the output to the orthogonal plane, where the demultiplexed spot array was detected by an InGaAs imager and later measured with a fiber mounted on a translation stage to provide fiber coupling efficiencies and measure output power spectra.

Figure 3 shows the array demultiplexed output. At left, the detected output intensity shows 8 columns (AWG output channels) and 11 rows (AWG diffraction orders), as well as a faint tilted row of spots near the center from a surface reflection off the beamsplitter. This illustrates the angle between the input fiber array and demultiplexed output. The center image is a perspective view with height corresponding to intensity, defocused to make the spot location more visible, and labeled with wavelengths on selected spots. The nonuniform output intensity indicates the ASE source power spectra. At right is the position of the output coupled into the output fiber on a rectangular grid.

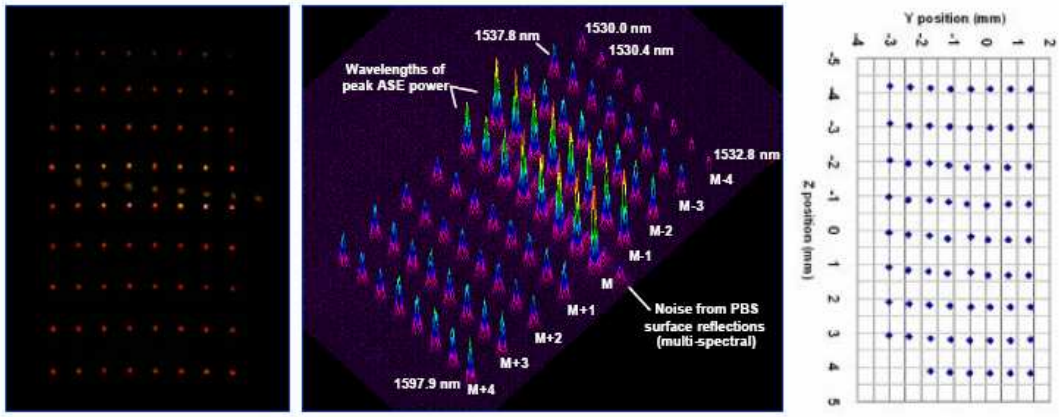

Figure 3: Array demultiplexed output showing ASE source spectral power variations. Left, image-plane intensity. Center, a defocused perspective plot of the output. Right, peak power locations plotted on a rectangular grid.

The output wavelength spectra is shown in Figure 4 and 5. Figure 4 shows the output wavelength spectra for all 72 outputs superimposed on a single plot. The signal to background level is 35 to 40 dB, consistent with WDM communications systems. The noise near the edges arises from the low ASE input power, not from the deMUX performance. The insertion loss of the system ranges from 17 to 23 dB, much greater than the sum of the AWG (~5 dB) and FSO demultiplexer (~3 dB) losses. The difference comes from inserting the 12.5 mm thick PBS into the gap between input fiber and transform lens, which was designed for an 11 mm air gap. The optical beam profile aberrations were revealed by measuring the intensity coupled into multimode fiber, which was approximately 10 dB higher in efficiency. Figure 5 shows the individual passband profile for three channels taken near the midpoint and edges of the wavelength spectrum. The 0.2 nm 20 dB rolloff passband is identical to the AWG output.

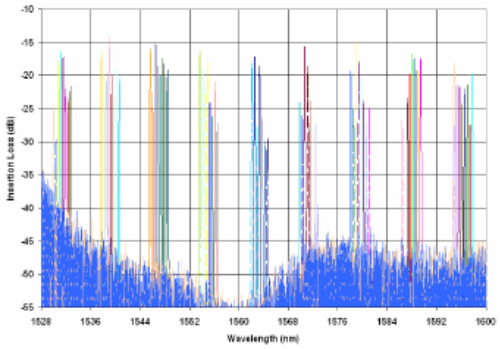

Figure 4: 72 channel FSO/AWG array deMUX output

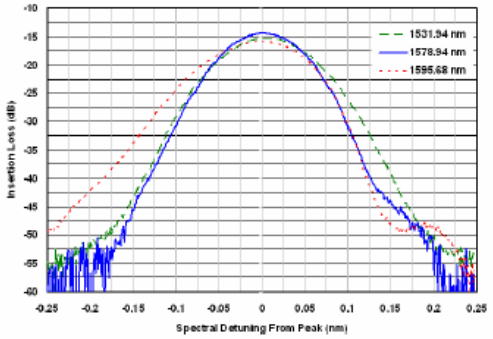

Figure 5: Representative channel passband profiles.

4. Conclusions

We presented a first proof-of-principle demonstration of a hybrid free-space / waveguide spectral demultiplexer which produces a 2-D array output. The spectral performance (passband and signal to background level) of the hybrid device is excellent. In on-going research, the insertion loss will be improved by modifying the FSO optics to reduce aberrations and by integrating the AWG device directly into the system. We believe that such 2-D array demultiplexers will prove valuable for large channel-count WDM systems, especially those based on surface normal opto-electronic and MEMS devices.

5. References

[1] Jean-Pierre Laude, *Wavelength Division Multiplexing* (Prentice Hall, 1994)

[2] K. Takada, M. Abe, M. Shibata, K. Okamoto, "Low-crosstalk 10-GHz-spaced 512-channel arrayed-waveguide grating multi/demultiplexer fabricated on a 4-in wafer," IEEE Photonics Tech. Letters 13(11) pp. 1182-4, 2001.

[3] A. V. Krishnamoorthy et al, "The AMOEBA network: an optoelectronic switch for multiprocessor networking using dense-WDM," IEEE Journal of Selected Topics in Quantum Electronics 5 (2), 261-275, March 1999.

[4] J. E. Ford and J. A. Walker, "Dynamic spectral power equalization using micro-opto-mechanics," IEEE Photonics Technology Letters 10 (10), 1440-1442, October 1998

[5] J. E. Ford, V. A. Aksyuk, D. J. Bishop and J. A. Walker, "Wavelength add/drop switching using tilting micromirrors," IEEE Journal of Lightwave Technology 17 (5), 904-911, May 1999.

[6] D. T. Neilson et al, "MEMS-based channelized dispersion compensator with flat passbands," IEEE J. Lightwave Tech. 22(1) pp. 101-105, Jan. 2004.

[7] C. Dragone and J. E. Ford, "Free-Space / Arrayed Waveguide Router," US Patent #6,263,127 Issued July 2001.

[8] C. Dragone "An N x N Optical Multiplexer Using a Planar Arrangement of Two Star Couplers," IEEE Photonics Tech. Letters 3(9), September 1991.

Appendix B

JOURNAL OF LIGHTWAVE TECHNOLOGY, VOL. 25, NO. 3, MARCH 2007

1092 Channel 2-D Array Demultiplexer for Ultralarge Data Bandwidth

Trevor K. Chan, Jason Karp, Rui Jiang, Nikola Alic, Stojan Radic, Christopher F. Marki, and Joseph E. Ford

Abstract—**We demonstrate 1 × 1092 channel wavelength demultiplexing with 50-GHz channel pitch and a 600-nm total bandwidth. Outputs from 1 × 40 channel arrayed waveguide gratings operating with multiple orders enter a free-space optical grating demultiplexer which separates the orders into a 2-D spot array, where the light can be coupled into discrete output fibers or operated on by a surface normal device (i.e., microelectromechanical system switch or detector array). Supercontinuum source input from 1140 to 1750 nm produced a 28 × 39 spot array at the output plane. The insertion loss for light is coupled into a single mode fiber ranged from 7 to 18 dB with less than 10-dB loss in channels between 1300 and 1750 nm. Bit-error-rate measurements show a negligible 0.1-dB power penalty at 10 GB/s.**

Index Terms—**Broadband communication, gratings, microelectromechanical systems (MEMS), optical communication, wavelength division multiplexing.**

I. Introduction

THE POTENTIAL bandwidth capacity of optical fibers, estimated to be over 100 Tb/s [1], remains unfulfilled in modern fiber communication systems, which reach up to 1.6 Tb/s. Even in research experiments, the maximum data capacity shown is on the order of 12 Tb/s [2]. Achieving 100-Tb/s capacity requires a combination of large channel counts and large per-channel data rates, with nearly an order of magnitude increase in wavelength spectrum over the ~100 nm used in current communication systems. One key component in reaching this goal is a large channel count and broad spectral-bandwidth wavelength multiplexer to combine and separate the data streams. Wavelength multiplexers are also instrumental in other wavelength management components including channel level monitors, wavelength switches, and spectral power equalizers.

Commercial wavelength multiplexers, including both waveguide and planar grating-based components, use a single diffractive element to separate wavelength channels into a spatially linear 1-D array of outputs. This is practical when dealing with approximately 100 channels, but a single linear array becomes problematic for large channel counts. For example, the linear alignment of 1000 collection fibers at a 125-μm pitch (from the diameter of single mode fiber) requires submicrometer alignment accuracy for each fiber in a 125-mm-long array. This is a major packaging challenge especially for components which may need to be hermetically sealed, leading to costly and potentially unreliable components.

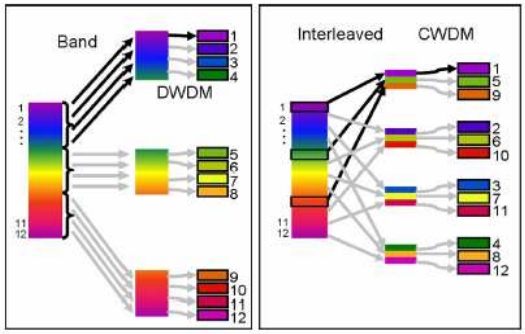

Fig. 1. Two approaches to hierarchical wavelength multiplexing. (Left) Banded. (Right) Interleaved.

This problem is avoided by using hierarchical (multistage) multiplexing. Takada *et al.* showed multistage demultiplexing using a cascade of two arrayed waveguide gratings (AWG) [3]. A course-spectral-pitch multiplexer was followed by multiple fine spectral multiplexers. The first stage consisted of a single AWG to create 25 channels spaced by 1 THz (8 nm). Each of these channels was further divided into 168 channels spaced at 5 GHz (0.04 nm) by the second stage of AWG. A separate AWG is used for each output of the primary stage, leading to 26 individually packaged components. The entire multiplexer produced a total of 4200 channels over a 159-nm spectrum. Assuming 80% bandwidth utilization, reasonable for the AWG Gaussian passbands, Takada's staged demultiplexer potentially allows up to 16.8-THz aggregate data bandwidth.

There are two categories of multistage multiplexing, as shown in Fig. 1. "Banded" multiplexers, as a first stage, use a course-pitch filter to separate spectrally adjacent clusters of channels, and as a second stage, a set of fine-pitch filters which further separate these groups into individual channels. Takada's is one example of a banded multiplexer. The alternative "interleaved" multiplexers, as a first stage, use a filter which isolates sets of individual data channels separated by some multiple of the individual channel pitch. The second stage is a relatively course filter which further separates these widely spaced channels into individual output channels. More complex (higher level) hierarchical multiplexers can also be constructed

Manuscript received January 5, 2006; revised November 10, 2006. This work was supported in part by the Natural Science and Engineering Research Council of Canada.

The authors are with the Department of Electrical and Computer Engineering, University of California, San Diego, La Jolla, CA 92093 USA (e-mail: tkc@ucsd.edu; jkarp@ucsd.edu; rjiang@ucsd.edu; nalic@ucsd.edu; radic@ece.ucsd.edu; cmarki@ucsd.edu; jeford@ucsd.edu).

Color versions of one or more of the figures in this paper are available online at http://ieeexplore.ieee.org.

Digital Object Identifier 10.1109/JLT.2006.889686

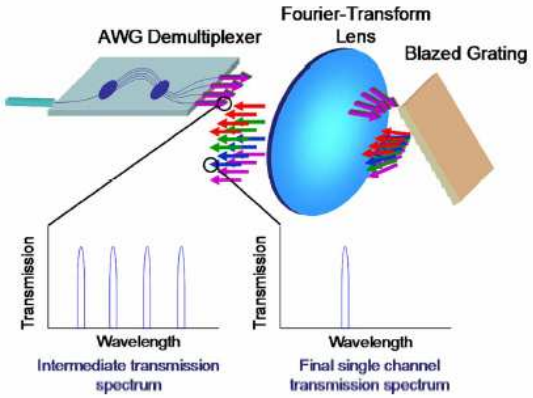

Fig. 2. Hybrid waveguide—FSG multiplexer producing a 2-D array output.

with three or more stages, potentially combining both banded and interleaved approaches.

AWG multiplexers are normally operated with a restricted spectral bandwidth so that each output waveguide carries a single channel. This is true in the multiplexer of Takada *et al.* [3] as each secondary AWG receives a signal that has been filtered to within one free spectral range (FSR) by the first AWG stage, which has a much wider FSR. However, as with all diffractive elements, AWG can yield multiple diffraction orders for a sufficiently broad input spectrum.

An interleaved multiplexer can be constructed using, as the first stage, an AWG in this higher order mode, where the input spectrum is much larger than the FSR. Each output waveguide then carries multiple channels, each corresponding to one diffraction order, and each separated from the adjacent channels by the AWG's FSR. These channels can be separated into individual waveguides by the second stage. Because the first-stage output produces fine channels with large gaps, the second-stage multiplexer can be a course wavelength multiplexer with narrow passbands. Free-space-grating (FSG) multiplexers are ideal for the second stage, especially because a single optical multiplexer can operate with a row of parallel inputs, provided the direction of dispersion is oriented perpendicular to the input row, so that the final output is a 2-D array of individual wavelength channels. The resulting system is shown in Fig. 2.

Such a hybrid multiplexer was proposed by Dragone and Ford in 2001 [4]. In 2004, Weiner and Xiao successfully demonstrated a related array multiplexer using a virtual imaged phased array multiplexer operated with multiple diffraction orders, followed by an FSG demultiplexer to create a 2-D array output [5]. This system produced 41 demultiplexed channels (four rows of ten channels) with about 1.75-GHz spectral bandwidth per channel, yielding a potential aggregate data bandwidth of 71.75 GHz. In 2005, we demonstrated an array multiplexer using the system in Fig. 2, a 1×8 AWG with 50-GHz pitch, and an FSG second stage, yielding 72 demultiplexed channels (nine rows of eight channels), which, again assuming a maximum spectral channel utilization of 80%, provided a potential aggregate data capacity of 2.88 Tb/s [6].

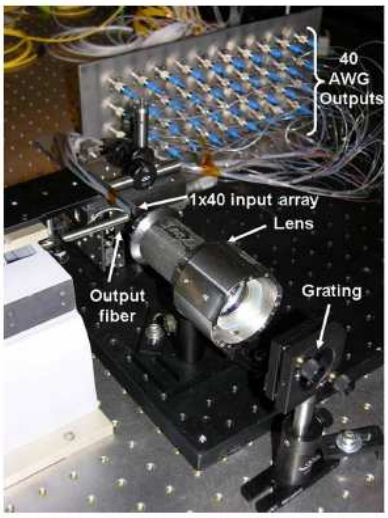

Fig. 3. Experimental setup showing the v-groove array that carries the 40 outputs from the first-stage multiplexer and the FSG multiplexer that produces a 2-D output array which is tested using a single individually aligned output fiber for channel characterization.

In this paper, we extend our earlier results to an ultralarge data capacity multiplexer which carries over 1000 individual channels at approximately 50-GHz pitch and spreads over a 600-nm wavelength spectrum for an aggregate potential data capacity of over 40 Tb/s. We characterize the performance of individual demultiplexed channels using a single-mode output fiber. This optical system, however, is primarily intended to be integrated with optoelectronic or micromechanical devices to construct wavelength switches and dynamic spectral equalizers for ultralarge data capacity networks.

II. Demultiplexer Setup

Fig. 3 shows a photograph of the experimental system. The first stage of our system consisted of a conventional 1×40 AWG demultiplexer with 50-GHz-output channel pitch. The 40th channel of the AWG had anomalously high loss, and therefore, only 39 outputs were used. At 1560 nm, the AWG showed less than 5-dB insertion loss and a 27.2-nm FSR. The relation between FSR, center wavelength λ_c, and diffraction order m is given by [7]

$$\mathrm{FSR} = \lambda_c \left[\frac{m}{m-1} - 1 \right]. \tag{1}$$

We find that the channels near 1560 nm lie in the 53rd diffraction order. The AWG is designed for this order and is typically not used outside of this range. However, other diffraction orders are produced with equally high transmission efficiency when the AWG is illuminated outside of this range.

For our system, we illuminated the AWG with a high brightness supercontinuum source with spectral output ranging

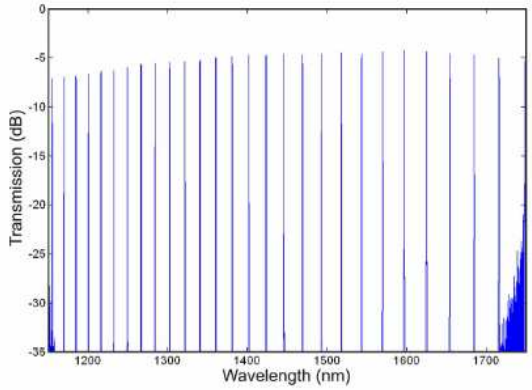

Fig. 4. Transmission spectra carried by a single-AWG output fiber when illuminated with a 600-nm bandwidth showing 28 diffraction orders separated by approximately 25-nm FSR. This is the first-stage (partially demultipled) output of our demultiplexer.

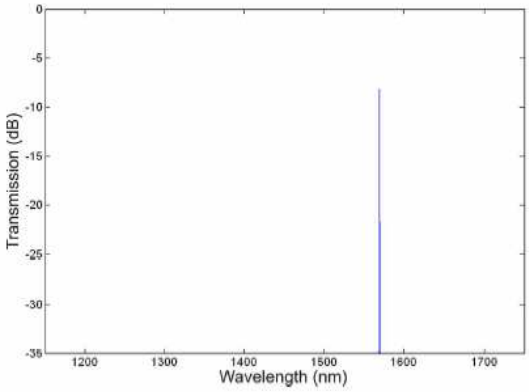

Fig. 5. Transmission spectra coupled to a fiber positioned at the image plane of the second-stage FSG demultiplexer showing a single-AWG diffraction order in the final output.

from 1150 to well over 1800 nm. With this source, the AWG operation bandwidth was limited only by the spectral range of our optical spectrum analyzers (OSAs) from 1100 to 1800 nm. With a 600-nm input bandwidth, the AWG produces a spectral comb of at least 28 diffraction orders in each output channel, as shown in Fig. 4.

All outputs of the AWG must be integrated with the second-stage (FSG) multiplexer to create a fully demultiplexed output. Ideally, the AWG waveguide would be directly integrated with the second stage, as shown in Fig. 2, avoiding intermediate fiber coupling losses. In our system, however, we connected a fully packaged AWG to a 1×40 linear v-groove array with polished fibers at a 127-μm pitch.

The second-stage demultiplexer consists of a 5-cm focal-length Fourier transform lens followed by a 75-lp/mm blazed reflection grating. The grating is coated with aluminum for adequate reflectivity of a broad spectrum of visible-to-near infrared wavelengths. The grating is oriented near Littrow angle, so that the first-order diffracted output is backreflected and returns through the Fourier lens and is refocused, creating an image of the v-groove array adjacent to itself. Since the grating is a diffractive element, the horizontal position of the image is determined by its wavelength. Since each diffraction order lies at a different wavelength, we generate multiple images which are horizontally displaced from each other. Moreover, the image of the array appears slanted due to wavelength variations among the channels within a diffraction order. We tilt the v-groove array in the opposite direction to align the spots in a vertical column. With a broadband input into our system, this ultimately produces a rectangular array of spots raster positioned according to their wavelength. Each of these spots represents the output position of a demultiplexed wavelength channel. The signal coupled to an optical fiber positioned at one of these output spots is shown in Fig. 5, showing suppression of all, but one diffracted order is visible in Fig. 4. This is the fully demultiplexed (single channel) output of the hybrid demultiplexer.

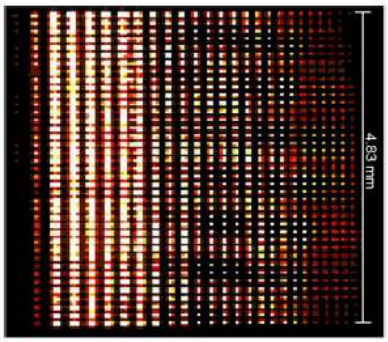

Fig. 6. Photograph of the entire output array taken by relay imaging the output into an InGaAs sensor array showing the 39 columns (first-stage AWG fiber inputs) of 28 diffraction orders each (dispersed by the FSG). The 320×240 InGaAs camera does not fully resolve the 1090 spots.

III. Array-Demultiplexer Output

We photographed the entire spot array using an infrared camera, a Sensors Unlimited 320M camera with a 320×240 array of InGaAs detector pixels at a 25-μm pitch. The output array is located adjacent to the fiber v-groove array; therefore, to obtain this photograph, we temporarily inserted a gold mirror to reflect the light out of the demultiplexer and into an imaging system consisting of two identical Fourier transform lenses in a unit-magnification 4f configuration. The image of the spot array is shown in Fig. 6. Each column of the array represents a single-AWG diffraction order, or in other words, a single image of the intermediate v-groove array. These spots are raster positioned according to wavelength from top to bottom and then from left to right. The nonuniformity of the array is a result of several factors, including the relatively course sampling grid of the detector pixels, the nonuniformity of the supercontinuum source (which varied by 15 dB over the 600-nm operating range), and wavelength dependent losses. An accurate measure of the insertion loss for each wavelength channel is shown in the following section.

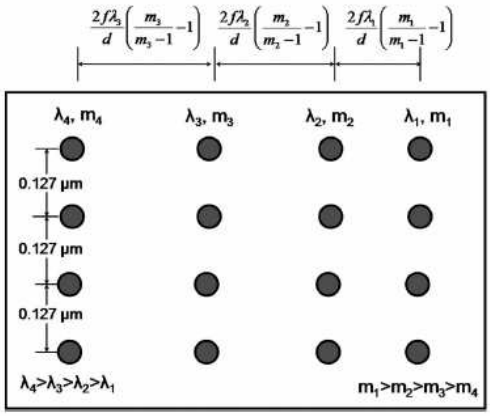

Fig. 7. Expected arrangement of the output spots. The vertical separation of the rows is constant, assuming negligible imaging system distortion, but the space between columns is a function of the diffraction order.

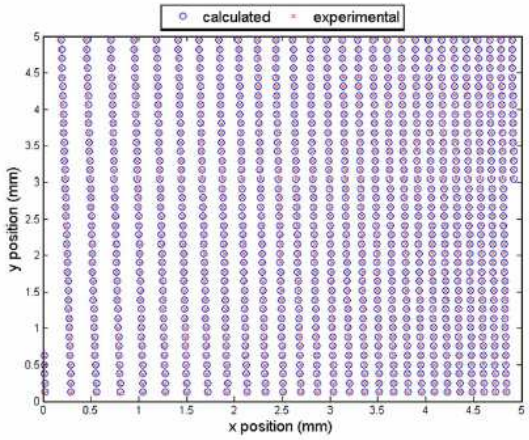

Fig. 8. Mapping of both theoretical and experimental spot locations in the output plane.

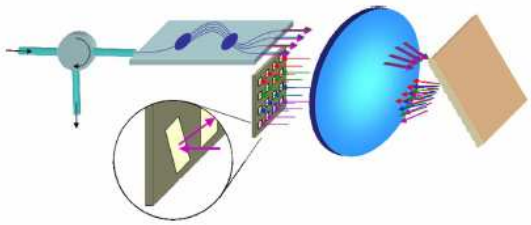

Fig. 9. Dynamic spectral equalizer employing the demultiplexer with an MEMS mirror array.

A standard SMF-28 single mode fiber mounted in a silicon v-groove and polished flat was used to characterize each of the 1092 individual channel outputs. The fiber was mounted on a PI model F206 hexapod stage (visible at left in Fig. 3) to provide < 0.1-μm absolute positioning accuracy. This fiber was scanned across the plane of best overall focus. The fiber coupled signal was connected to the external components for intensity measurements, spectral analysis, polarization dependence loss measurements, and bit-error-rate (BER) tests.

Fig. 7 diagrams the calculated output-spot distribution. The rows are separated by 0.127 mm, which is equal to the pitch of the 1×40 v-groove array. The separation between the columns is set by the dispersion from diffraction from the FSG, and so is proportional to the FSR (1) and increases monotonically with the wavelength. In the equations shown, m_n is the AWG diffraction order at wavelength λ_n, f is the lens focal length, and d is the grating period of the free-space demultiplexer.

The output-spot wavelengths are distributed in a raster fashion. The shortest wavelength signal is in the lower right, increasing in 50-GHz steps as you move up the column. There is a longer interval before you reach the next diffraction order, which starts at the next column to the left. The longest wavelength output is in the upper left corner. The design of the AWG (delay arm length distribution and output-waveguide arrangement) determines the space between diffraction orders.

Fig. 8 shows crosses at the measured position of maximum coupling efficiency for each channel into the fiber. These are plotted against their predicted positions represented by circles, calculated based on their diffraction order in the AWG and the grating equation, and measured focal length of the Fourier transform lens. The absolute position of the predicted and experimental data is aligned to minimize the RMS difference, which was 6.5 μm. In our measured data set, the column pitch decreases by more than half, from 0.268 mm near 1800 nm (at left) to 0.114 mm near 1160 nm (at right).

Irregularities in the output-spot position would be problematic if the output channels were to be coupled directly into a 2-D fiber array: A lateral offset of 5 μm would change the insertion loss by approximately 5 dB. In the intended application, however, the signals are incident on optoelectronic detectors (for signal monitoring) or on microelectromechanical system (MEMS) mirrors or reflective liquid crystal modulators (for wavelength switching and equalization). The large lateral pitch between active regions makes it straightforward to fabricate individual devices with oversized apertures. In such devices, reflected signals are automatically realigned to the output fibers when they are remultiplexed by a second pass through the optical system [8], [9]. A dynamic spectral equalizer shown in Fig. 9 serves as an example of a typical setup where tiltable MEMS mirrors control individual channel alignment for attenuation control in a double pass configuration.

IV. Output Channel Characterization

The collected signals were relayed to an optical spectrum analyzer to measure the channel passband profiles shown in Figs. 10 and 11. Fig. 10 shows the insertion loss of a single channel at 1533.7 nm as well as its intermediate passband spectrum immediately following the AWG. The AWG insertion

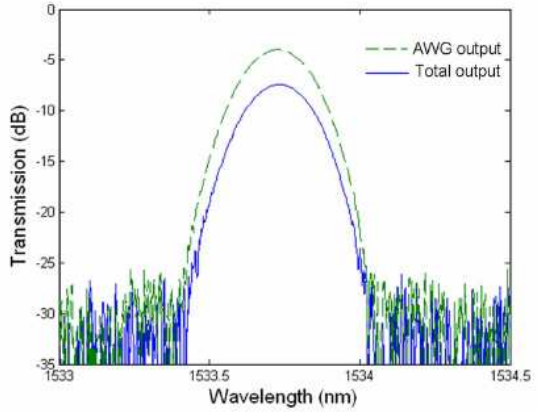

Fig. 10. Insertion loss and passband profile for a single output channel (solid line) closely following the Gaussian profile of the AWG output in the intermediate demultiplexing stage.

loss was 4 dB, and a combined additional loss of 3.4 dB came from the grating demultiplexer, the v-groove array, and the fiber connections. The Gaussian profile, the 0.24-nm 3-dB rolloff, and the 25-dB signal-to-background ratio of the AWG are maintained in the fully demultiplexed output.

In wavelength-division-multiplexing systems, crosstalk from neighboring channels is a concern. In our 2-D raster-positioned array of outputs, crosstalk may also come from adjacent channels in the array. This includes channels that are one FSR over in the neighboring diffraction orders. Fig. 12 shows the output spectrum of a single channel with the adjacent spots labeled where their passbands would appear. This reveals that there is no leakage of the signal into neighboring channels.

Fig. 11 shows the insertion loss of all 1092 channels, superimposed on a single 600-nm spectrum. The plot is sectioned to fit into a column format. The increase in the background noise near the minimum (1140 nm) and maximum (1750 nm) wavelengths is due to the lower input signal levels and OSA sensitivity at these wavelengths. Insertion losses over the entire spectral range vary smoothly between 7 and 18 dB with the greatest losses occurring in channels below 1300 nm. This is a result of the wavelength dependent losses of the two stages of demultiplexer at wavelengths far outside of their intended C-band function.

If we only accept channels with less than 10-dB insertion losses, our channel count is reduced to approximately 663 channels. With 80% bandwidth utilization, our demultiplexer would manage approximately 30% (26.5 THz) of the total spectral bandwidth. Much of the unaccounted data comes from high insertion losses far outside of the C-band wavelengths. Near the C-band, specifically at 1533.75 nm, we measured 4-dB loss from the AWG and 3.4-dB loss from the FSG. At approximately 1730 nm, both of the components exhibit almost no change in performance with 5-dB loss from the AWG and 3-dB loss from the grating. We see the components start to fail further away from the C-band below 1300 nm. At 1135 nm, we measured 7-dB loss from the AWG and an

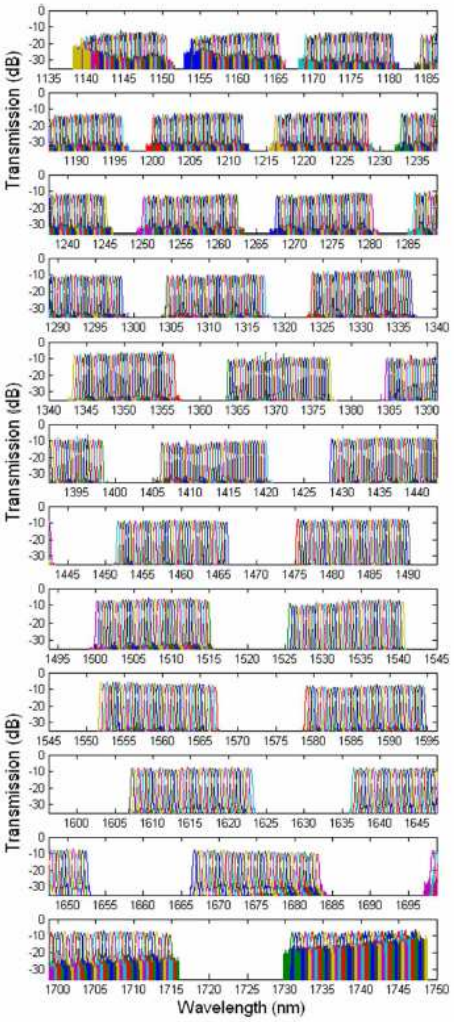

Fig. 11. All 1092 output channels superimposed over the full 600-nm spectrum showing a smooth variation in insertion loss.

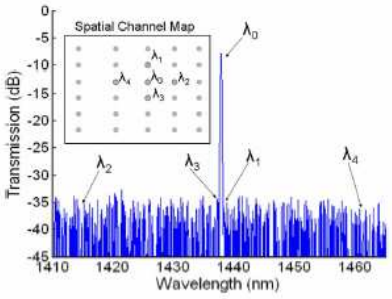

Fig. 12. Wide spectrum of a single channel showing no crosstalk between adjacent spots in the array.

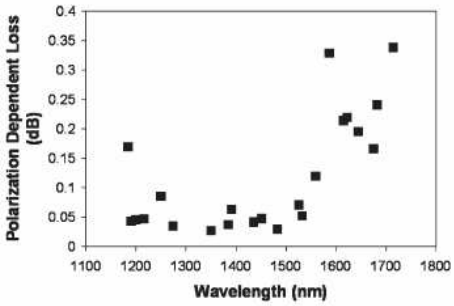

Fig. 13. Sampled PDL across the demultiplexer wavelength range.

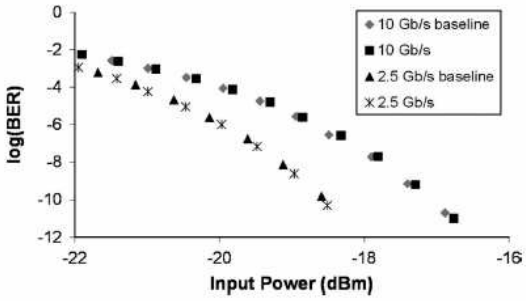

Fig. 14. BER testing of the 1543.9 channel of the demultiplexer showing a negligible penalty at both 2.5 and 10 Gb/s.

even greater 10.5-dB loss from the FSG demultiplexer. These results show that the usable bandwidth in our setup is largely limited by the reflectivity of the grating demultiplexer and not by the AWG. Fig. 11 also shows that much of the spectrum is unused between diffraction orders. This is inherent from our AWG and can be avoided with a suitable AWG design. Customized AWG fabrication also allows flexibility in the channel spacings to fit a different number of total channels in the usable wavelength range. For example, the two-stage AWG demultiplexer developed by Nippon Telegraph and Telephone (NTT) Corp. generates 4200 channels over a shorter range by using an AWG with 5-GHz channel pitch [3]. The capacity of this demultiplexing scheme is only limited by the wavelengths that are filtered out through the components.

Both waveguide and free-space multiplexers can introduce significant polarization dependent loss (PDL). Current fabrication techniques have been proven effective in minimizing PDL in commercial AWG and are effective over a broad wavelength spectrum. PDL in planar diffraction gratings depends on operating spectrum and dispersion, but for the relatively course pitch, we require (75 lp/mm, as opposed to the 600 lp/mm used in [7]) low PDL gratings available: Ours had a specification of less than 0.1 dB over the bandwidth of our supercontinuum source. When the AWG and the grating are combined in the 2-D demultiplexing system, the total PDL across the active spectrum is less than 0.4 dB. This is shown in Fig. 13 which reveals very little wavelength dependence on PDL.

Although the spectral passband profile of the AWG was maintained, it was possible that the second-stage demultiplexer introduced a nonuniform chromatic dispersion which could adversely impact data transmission. To verify that this was not the case, we performed BER tests to measure any loss in signal integrity. The output fiber was positioned to collect the 1543.9-nm wavelength channel. We then modulated a 1543.9-nm signal with a pseudorandom binary sequence and nonreturn-to-zero coding to perform BER tests on the demultiplexer. We used both 2.5- and 10-Gb/s modulation rates. Fig. 14 shows the results of these tests, and it is evident that the demultiplexer maintains signal quality. The penalty suffered by the 2.5-Gb/s signal was superimposed on the back-to-back signal, and the 10-Gb/s signal showed a still-negligible power penalty of 0.1 dB. Since all channels encounter the same optical components, we expect similar results for the remaining channels.

V. Conclusion

We have demonstrated a 2-D wavelength demultiplexer with 1092 channels spread over a 600-nm spectral band. If we assume an 80% utilization of the 50-GHz pitch channels, this device supports a record aggregate potential data capacity of up to 44 Tb/s. The channel passbands were Gaussian in profile and showed to support 10-Gb/s data modulation without significant power penalty. The outputs were characterized using a single scanned fiber, but this demultiplexer is primarily intended to be used in wavelength switching, equalization, and monitoring components using MEMS, inductance–capacitance (L–C), and optoelectronic devices. We believe that the total channel capacity of such array-parallel demultiplexers can be increased to 5000 or more channels by optimizing the AWG to reduce dead space between diffraction orders and by designing the FSG to operate over a 1200-nm spectral band.

References

[1] P. P. Mitra and J. B. Stark, "Nonlinear limits to the information capacity of optical fibre communications," *Nature*, vol. 411, no. 6841, pp. 1027–1030, Jun. 2001.

[2] K. Fukuchi, T. Kasamatsu, M. Morie, R. Ohhira, T. Ito, K. Sekiya, D. Ogasahar, and T. Ono, "10.92-Tb/s (273* 40-Gb/s) triple-band/ultra-dense WDM optical-repeatered transmission experiment," in *Proc. Opt. Fiber Commun. Conf. (IEEE Cat. 01CH37171)*, 2001, pp. PD24-1–PD24-3.

[3] K. Takada, M. Abe, T. Shibata, and K. Okamoto, "5 GHz-spaced 4200-channel two-stage tandem demultiplexer for ultra-multi-wavelength light source using supercontinuum generation," *Electron. Lett.*, vol. 38, no. 12, pp. 572–573, Jun. 2002.

[4] C. Dragone and J. E. Ford, "Free-space/arrayed waveguide router," U.S. Patent 6 263 127, Jul. 17, 2001.

[5] A. M. Weiner and S. Xiao, "2-D wavelength demultiplexer with potential for $\geq$ 1000 channels in the C-band," *Opt. Express*, vol. 12, no. 13, pp. 2895–2902, 2004.

[6] T. K. Chan, M. Abashin, and J. E. Ford, "2-D array wavelength demultiplexing by hybrid waveguide and free-space optics," presented at the OSA/IEEE Optical Fiber Commun. Conf., Anaheim CA, Mar. 2005, Paper OThV7.

[7] A. Dutta, N. Dutta, and M. Fujiwara, *WDM Technologies: Passive Optical Components*. San Diego, CA: Academic, 2003, p. 61.

[8] J. E. Ford, V. A. Aksyuk, D. J. Bishop, and J. A. Walker, "Wavelength add/drop switching using tilting micromirrors," *J. Lightw. Technol.*, vol. 17, no. 5, pp. 904–911, May 1999.

[9] D. M. Marom, D. T. Neilson, D. S. Greywall, C.-S. Pai, N. R. Basavanhally, V. A. Aksyuk, D. O. Lopez, F. Pardo, M. E. Simon, Y. Low, P. Kolodner, and C. A. Bolle, "Wavelength-selective $1 \times K$ switches using free-space optics and MEMS micromirrors: Theory, design, and implementation," *J. Lightw. Technol.*, vol. 23, no. 4, pp. 1620–1630, Apr. 2005.

Trevor K. Chan was born in Edmonton, AB, Canada, on March 6, 1980. He received the B.Sc. degree in engineering physics from the University of Alberta, Edmonton, in 2002 and the M.Sc. degree in electrical and computer engineering from University of California, San Diego (UCSD), La Jolla, and 2004 where he is currently working toward the Ph.D. degree in electrical and computer engineering.

He was with the Photonics Systems Integration Laboratory, UCSD, in 2003. His research interests include free-space optical communications, optical modulators, and wavelength division multiplexing technologies.

Jason Karp received the B.S. degree in electrical engineering from the University of Miami, Miami, FL, in 2004. He is currently working toward the M.A. and Ph.D. degrees at the University of California, San Diego (UCSD), La Jolla.

He joined the Photonics Systems Integration Laboratory, UCSD, in 2005. His current research interests include free-space communication systems, imaging, and wavefront sensing.

Rui Jiang was born in Hubei, China, in 1978. He received the B.S. degree in engineering physics from Tsinghua University, Beijing, China, in 2000 and the M.A. degree in laser plasma physics and imaging science from University of Rochester, Rochester, NY, in 2004. He is currently working toward the Ph.D. degree at the Department of Electrical and Computer Engineering, University of California, San Diego (UCSD), La Jolla.

He was with the China Institute of Atomic Energy, working on laser plasma physics for two years. His interest lies in the nonlinear fiber optics, especially in parametric process.

Nikola Alic is currently working toward the Ph.D. degree at the University of California, San Diego, La Jolla.

Stojan Radic graduated from The Institute of Optics, University of Rochester, Rochester, NY.

He has subsequently served as Senior Scientist with Corning Inc., Corning, NY, member of the Technical Staff at Bell Laboratories, and Nortel Networks Chair at Duke University, Durham, NC. He is currently an Associate Professor leading the Optical Networking Laboratory at the University of California, San Diego (UCSD), La Jolla/CalIT2. His research is focused on parametric processing and its use in all-optical networks.

Mr. Radic currently serves on the Conference on Lasers and Electro-Optics (CLEO), Optical Fiber Communications (OFC), and Optical Amplifiers and Their Applications (OAA) committees and is an Optical Communications Editor for *Optics Express*.

Christopher F. Marki was born in San Jose, CA, in August 1980. He received the B.S. degree in electrical engineering from Duke University, Durham, NC, in 2002. He subsequently matriculated to the University of California, San Diego (UCSD), La Jolla, where he received the M.S. degree in photonics in June 2004, where he is currently working toward the Ph.D. degree in optical communications.

He has held internships at Lucent Technologies and Anritsu Corporation and works closely with the Ziva Corporation, San Diego and Marki Microwave, Morgan Hill, CA.

Joseph E. Ford received the Ph.D. degree from University of California, San Diego (UCSD), La Jolla, in 1992 and the M.A. degrees in physics and optical engineering from the University of British Columbia, Vancouver, BC, Canada, and University of Rochester, Rochester, NY, respectively.

He is a coauthor of 35 refereed journal articles and 45 U.S. patents on optical components and systems. He was a member of Bell Labs' Advanced Photonics Research Department from 1994 to 2000, where he developed optoelectronics and micro-opto-mechanics for optical communications. From 2000 to 2002, he was with Optical Micromachines, San Diego, CA. In 2002, he became an Associate Professor with the Department of Electrical and Computer Engineering, USCD, where he leads the Photonic Systems Integration Laboratory.

Bibliography

[1] A. Acampora, "Last mile by laser," *Sci. Am.* **287**(1), 48-53 (2002).

[2] Leitgeb E., Bregenzer J., Fasser P., Gebhart M., Free Space Optics – Extension to Fiber-Networks for the "Last Mile", Proceedings of the 2002 IEEE LEOS Annual Meeting, Paper WL5, (IEEE, Glasgow, Scotland, 2002).

[3] M.-C. Jeong, J.-S. Lee, S.-Y. Kim, S.-W. Namgung, J.-H. Lee, M.-Y. Cho, S.-W. Huh, Y.-S. Ahn, J.-W. Cho and J-S. Lee, "8 x 10-Gb/s terrestrial optical free-space transmission over 3.4 km using an optical repeater,' IEEE Phot. Tech. Lett. **15**(1), 171-173 (2003).

[4] G. Nykola, G. Raybon, B. Mikkelsen, B. Brown, P. F. Szajowski, J. J. Auborn and H. M. Presby, "A 160 Gb/s free space transmission link" in *Proceedings of 2000 CLEO*, Paper PD15, (IEEE, Washington, D.C., 2000).

[5] Yoshikawa, M., Murakami, A., Sakurai, J., Nakayama, H., and Nakamura, T.: 'High power VCSEL devices for free space optical communications'. Electronic Components and Technology Conf, (IEEE, 2005), pp. 1353–1358.

[6] D. Kerr, K. Bouazza-Marouf, K. Girach, T. West, "Free space laser communication links for short range control of mobile robots using active pointing and tracking techniques," IEE Colloquium on Optical Free Space Communication Links, (IEE, London, UK, Feb. 1996), pp. 11/1-11/5.

[7] E. Leitgeb, K. Zettl, S. Muhammad, N. Schmitt, W. Rehm, "Investigation in Free Space Optical Communication Links Between Unmanned Aerial Vehicles (UAVs)," ICTON 2007, Paper TuD3.2, (IEEE, Rome, Italy, July 2007), pp. 152-155.

[8] V. I. Tatarski, *The Effects of the Turbulent Atmosphere on Wave Propagation* (Israel Program for Scientific Translations, 1971).

[9] D. L. Fried, G. E. Mevers, and M. P. Keister, "Measurements of Laser-Beam Scintillation in the Atmosphere," J. Opt. Soc. Am. **57**(6), 787-797 (1967).

[10] S. Arnon and N. S. Kopeika, "Laser satellite communication network-Vibration effect and possible solutions," Proc. IEEE **85**(10), 1646-1661 (1997).

[11] C. Motlagh, V. Ahmadi, Z. Ghassemlooy, and K. Abedi, "The effect of atmospheric turbulence on the performance of the free space optical

communications", CSNDSP 2008, (IEEE, Graz, Austria, July 2008), pp. 540-543.

[12] M. S. Awan, E. Leitgeb, Marzuki, M. S. Khan, F. Nadeem, C. Capsoni, "Evaluation of fog attenuation results for optical wireless links in free space," IWSSC 2008, (IEEE, Toulouse, France, Oct. 2008), pp. 112-116.

[13] D. Kedar and S. Arnon, "Optical Wireless Communication Through Fog in the Presence of Pointing Errors," Appl. Opt. **42**(24), 4946-4954 (2003).

[14] L. Zhou, J. M. Kahn, K. S. J. Pister, “Scanning micromirrors fabricated by an SOI/SOI wafer-bonding process,” J. Microelectromech. Syst. **15**(1), 24-32 (2006).

[15] C.L. Edwards, J.R. Bruzzi, B.G. Boone. “Free-space high data rate communications technologies for near terrestrial space,” in Vol. 7091 of Proceedings of SPIE (SPIE, USA, 2008), pp. 709109 (15).

[16] L. Zhou, M. Last, V. Milanovic, J.M. Kahn, and K. S. J. Pister, “Two-axis scanning mirror for free-space optical communication between UAVs,’ 2003 IEEE/LEOS International Conference on Optical MEMS, Paper WP14, (IEEE, Hawaii, 2003).

[17] V. Nikulin, R. Khandekar, J. Sofka, “Performance of a laser communication system with acousto-optic tracking: An experimental study,” in Vol. 6105 of Proceedings of SPIE, (SPIE, 2006), pp. 61050C.

[18] A. Yariv, P. Yeh, *Optical Waves in Crystals*, (Wiley, Hoboken, 2003).

[19] B. Winker, M. Mahajan, M. Hunwardsen, “Liquid crystal beam directors for airborne free-space optical communications,” in *2004 IEEE Aerospace Conference Proceedings*, (IEEE, Big Sky. Montana, March 2004), pp. 1709.

[20] R. G. Buser, R. S. Rohde, N. T. Nomiyama, “Laser retroreflector system for identification of friend or foe,” US Patent #4,361,991 issued November 1982.

[21] X. G. Sun, R. W. Babbitt, “Modulated retroreflection system for secure communication and identification,” US Patent #5,819,164 issued October 1998.

[22] M. A. Reed, "A personal level identification friend or foe system employing free space optical communications," 1992 IEEE International Conference on Selected Topics in Wireless Communications, (IEEE, June 1992), pp. 257-278.

[23] J. Liu, G. E. Faulkner, S. Collins, D. C. O'Brien, S. J. Elston, "An optically powered, free space optical communications receiver," ISCAS 2008, (IEEE, Seattle, WA, May 2008), pp. 197-200.

[24] J.M. Kahn, R.H. Katz, K.S.J. Pister, "Next century challenges: mobile networking for smart dust", in Proceedings of the ACM MobiCom'99, (IEEE, Washington, USA, 1999), pp. 271–278.

[25] T. Mikaelian, M. Weel, A. Kumarakrishnan, P.R. Battle, and R.C. Swanson, "A high-speed retro-reflector for free-space communication based on electro-optic phase modulation," Can. J. Phys. **81**, 639 (2003).

[26] G. Spirou, I. Yavin, M. Weel, T. Mikaelian, A. Vorozcovs, A. Kumarakrishnan, P.R. Battle, and R.C. Swanson. "A high-speed-modulated retro-reflector for lasers using an acousto-optic modulator," Can J. Phys. **81**, 625 (2003).

[27] D. A. B. Miller, D. S. Chemla, T. C. Damen, A. C. Gossard, W. Wiegmann, T. H. Wood, and C. A. Burrus, "Bandedge electro-absorption in quantum well structures: the quantum confined Stark effect," Phys. Rev. Lett. **53**(22), 2173–2177 (1984).

[28] E. Hällstig, J. Öhgren, L. Allard, L. Sjöqvist, D. Engström, S. Hård, D. Ågren, S. Junique, Q. Wang, and B. Noharet, "Retrocommunication utilizing electroabsorption modulators and nonmechanical beam steering," Opt. Eng. **44**(4), 045001 (2005).

[29] J Öhgren, F Kullander, L Sjöqvist, K Wang, Q Wang, "A high-speed modulated retro-reflector communication link with a transmissive modulator in a cat's eye optics arrangement," in Vol. 6736 of Proceedings of SPIE, (SPIE, Florence, Italy, 2007), pp. 673619.

[30] W. S. Rabinovich, R. Mahon, P. G. Goetz, E. Waluschka, D. S. Katzer, S. C. Binari, and G. C. Gilbreath, "A Cat's Eye Multiple Quantum-Well Modulating Retro-Reflector,' IEEE Phot. Tech. Lett. **15**(3), 461-463, (2003).

[31] Goossen, K.W.; Prather, D.W., "Fabrication and Yield of Large-Area Quantum-Well Modulators," Photonics Technology Letters, IEEE , **19**(24), 2054-2056 (2007).

[32] S. Junique, Q. Wang, S. Almqvist, B. Noharet, and J. Y. Andersson, "Large-area three-state, binary amplitude and binary phase vertical-cavity multiple quantum well electroabsorption modulator," Optics Express **15**(14), 8566-8575 (2007).

[33] Qin Wang; S. Junique; D. Agren; B. Noharet; J.Y. Andersson, "Fabry-Perot electroabsorption modulators for high-speed free-space optical communication," Photonics Technology Letters, IEEE **16**(6), 1471-1473 (2004).

[34] G. C. Gilbreath, W. S. Rabinovich, T. J. Meehan, M. J. Vilcheck, R. Mahon, R. Burris, M. Ferraro, I. Solkolsky, J. A. Vasquez, C. S. Bovais, K. Cochrell, K. C. Goins, R. Barbehenn, D. S. Katzer, K. Ikossi-Anastasiou, and M. J. Montes, "Large-aperture multiple quantum well modulating retroreflector for free-space optical data transfer on unmanned aerial vehicles," *Opt. Eng.* **40**(7), 1348-1356 (2001).

[35] Jenkins, C.; Johnstone, W.; Uttamchandani, D.; Handerek, V.; Radcliffe, S., "MEMS actuated spherical retroreflector for free-space optical communications," Electronics Letters 41(23), 1278-1279 (2005).

[36] L. Zhou, K.S.J. Pister, J.M. Kahn, "Assembled corner-cube retroreflector quadruplet", *MEMS 2002*, (IEEE, Las Vegas, Nevada, Jan. 2002), p.556-559.

[37] Hong Y.K., Syms R.R.A., Pister K.S.J., Zhou L.X. "Design, fabrication and test of self-assembled optical corner cube reflectors," J. Micromech. Microeng. **15**, 663-672 (2005).

[38] L. Zhou, J. M. Kahn and K. S. J. Pister, "Corner-cube retroreflectors based on structure-assisted assembly for free-space optical communication," Journal of Micromechanical Systems **12**(3), 233-242 (2003).

[39] D. Pedersen and O. Solgaard, "Free space communication link using a grating light modulator," Sensors and Actuators **83**(1-3), 6-10, (2000).

[40] J. A. Walker, K. W. Goossen and S. C. Arney, "Fabrication of a mechanical antireflection switch for fiber-to-the-home systems." IEEE J. of Microelectromechanical Systems **5**(1), 45-51 (1996).

[41] J. E. Ford, J. A. Walker, D. S. Greywall and K. W. Goossen, "Micromechanical fiber optic attenuator with 4 µs response," IEEE J. of Lightwave Technology **16**(9), 1663-1670 (1998).

[42] D. S. Greywall, P. A. Busch and J. A. Walker, "Phenomenological model for gas-damping of micromechanical structures," Sensors and Actuators **72**(1), 49-70 (1999).

[43] G. C. Gilbreath et al., "Progress in development of multiple-quantum-well retromodulators for free-space data links," Opt. Eng. **42**(6), 1611-1617 (2003).

[44] C. Luo and K. W. Goossen, “Optical microelectromechanical system array for free-space retrocommunication,” IEEE Photonics Technology Letters 16(9), 2045-2047, (2004).

[45] J. Ford and J. Walker, “Technique for modulating optical signals in optical communications,” US Patent #5,796,880, issued August, 1998.

[46] S. Sakarya, G. Vdovin and P. Sarro, “Micromachined SLM based on pixelated reflective membranes,” in Vol. 3760 of Proceedings of SPIE, (SPIE, Denver, CO, July 1999), pp. 23-31.

[47] H. A. MacLeod, *Thin-Film Optical Filters*, (Hilger, Bristol, 1986).

[48] H. Conzelmann, K. Graff and E. R. Weber, “Chromium and chromium-boron pairs in silicon,” Appl. Phys. A 30(3), 169-175, (1983).

[49] M. Cole and K. Kiasaleh, “Signal intensity estimators for free-space optical communications through turbulent atmosphere.” IEEE Photon. Technol. Lett. **16**(10), 2395-2397 (2004).

[50] I. Filinski and T. Skettrup, “Fast dispersive beam deflectors and modulators,” IEEE J. Quantum Electron. **18**(7), 1059-1062 (1982).

[51] C. Dragone and J. E. Ford, “Free-Space / Arrayed Waveguide Router,” United States Patent number 6,263,127, issued July 2001.

[52] A. M. Weiner and S. Xiao, “2-D wavelength demultiplexer with potential for ≥ 1000 channels in the C-band,” Optics Express **12**(13), 2895-2902 (2004).

[53] J. E. Simsarian, A. Bhardwaj, J. Gripp, K. Sherman, Y. Su, C. Webb, L. Zhang, M. Zirngibl,, “Fast switching characteristics of a widely tunable laser transmitter,” IEEE Photon. Technol. Lett. **15**(8), 1038-1040 (2003).

[54] M. Shirasaki, “Virtually imaged phased array,” Fujitsu Sci. Tech. J. **35**(1), 113-125 (1999).

[55] M. Shirasaki and S. Cao, “Optical apparatus which uses a virtually imaged phased array to produce chromatic dispersion,” US Patent #7,193,778, issued March 2007.